UNIVERSITY OF GENOVA

PHD PROGRAM IN BIOENGINEERING AND ROBOTICS

Model-based myoelectric control of robots for assistance and rehabilitation

by

Nicola Lotti

Thesis submitted for the degree of *Doctor of Philosophy* (32° cycle)

May 2020

Prof. Vittorio Sanguineti — Supervisor

Thesis Jury:

Prof. Andrea D'Avella, *University of Messina* — External examiner

Prof. Strahinja Dosen, *Aalborg University* — External examiner

Prof. Silvio Sabatini — Internal examiner

Dibris

Department of Informatics, Bioengineering, Robotics and Systems Engineering

Declaration

I hereby declare that except where specific reference is made to the work of others, the contents of this dissertation are original and have not been submitted in whole or in part for consideration for any other degree or qualification in this, or any other university. This dissertation is my own work and contains nothing which is the outcome of work done in collaboration with others, except as specified in the text and Acknowledgements.

Nicola Lotti
May 2020

Abstract

The first anthropomorphic robots and exoskeletons were developed with the idea of combining man and machine into an intimate symbiotic unit that can perform as one joint system. A human-robot interface consists of processes of two different nature: (1) the physical interaction (pHRI) between the device and its user and (2) the exchange of cognitive information (cHRI) between the human and the robot. To achieve the symbiosis between the two actors, both need to be optimized.

The evolution of mechanical design and the introduction of new materials pushed pHRI to new frontiers on ergonomics and assistance performance. However, cHRI still lacks on this direction because it is more complicated: it requires communication from the cognitive processes occuring in the human agent to the robot, e.g. intention detection; but also from the robot to the human agent, e.g. feedback modalities such as haptic cues.

A possible innovation is the inclusion of the electromyographic signal, the command signal from our brain to the musculoskeletal system for the movement, in the robot control loop.

The aim of this thesis was to develop a real-time control framework for an assistive device that can generate the same force produced by the muscles. To do this, I incorporated in the robot control loop a detailed musculoskeletal model that estimates the net torque at the joint level by taking as inputs the electromyography signals and kinematic data. This module is called *myoprocessor*.

Here I present two applications of this control approach: the first was implemented on a soft wearable arm exosuit in order to evaluate the adaptation of the controller on different motion and loads. The second one, was a generation of myoprocessor-driven force field on a planar robot manipulandum in order to study the modularity changes of the musculoskeletal system.

Both applications showed that the device controlled by myoprocessor works symbiotically with the user, by reducing the muscular activity and preserving the motor performance.

The ability of seamlessly combining musculoskeletal force estimators with assistive devices opens new avenues for assisting human movement both in healthy and impaired individuals.

Table of contents

[1] *Partial content of this Chapter has been published as* Lotti N. and Sanguineti V. Toward emg-controlled force field generation for training and rehabilitation: From movement data to muscle geometry. *International conference on Rehabilitation Robotics* (ICORR), 17-20 July 2017, London (UK).

[2] *Partial content of this Chapter has been published as* Lotti N. and Sanguineti V. Estimation of muscle torques from EMG and kinematics during planar arm movements. *IEEE International Conference on Biomedical Robotics and Biomechatronics*, 29-29 August 2018, Enschede (NL).

[3] *The whole content of this Chapter has been published as* Lotti, N., Xiloyannis, M., Durandau, G., Galofaro, E., Sanguineti, V., Masia, L., and Sartori,M. Adaptive model-based myoelectric control for a soft wearable arm exosuit: A new generation of wearable robot control. *IEEE Robotics & Automation Magazine, 2020.*

List of figures

List of tables

Introduction

I, Robot

"Imagine a wearable robot that gives you superhuman abilities, or another one that takes wheelchair users up standing and walking again..." In his beautiful TED talk in 2011, Eythor Bender addressed the potential of the human-robot interaction, by describing this new technology as *"something that you put in the morning and it will give you extra-strength and it will further enhance your speed by helping you on your daily routine"* (Bender, 2011).

Nowadays, wearable robotics has expanded in several areas, embracing the civil and industrial domains. In particular, the introduction of smart sensing and actuation that can interface the user and the robot through biological signals made the human-machine interaction close to the symbiosis goal (Masia and Vitiello, 2020).

However, to completely achieve the synergistic effort of these multiple actors, it is necessary to find the best way for the user's intention detection. How can we find it? Daniel Wolpert (Wolpert, 2011) invited to reflect that all living being that move voluntarily have a brain: the complexity of the movement somewhat is reflected in the complexity of our brain.

For this reason, the best way to control a robot that can cooperate with a user in a symbiosis way is to include in the machine control loop the same motor command that the brain sends to the motor system: this can be done through electromyographic signal.

The electromyographic signal (EMG) is the muscle fiber electrical activity which reflects the signal that our brain uses. The detection and the inclusion of these signals in a robotic control loop through a human-machine interface (HMI) have the potential to make user and robot a single being through a perfect symbiosis.

Assistance and rehabilitation: two sides of the same coin

Work-related musculoskeletal disorders (WRMDs) are the most common occupational illnesses in Europe: nearly of 50% of european worker suffer from back, neck or upper limb

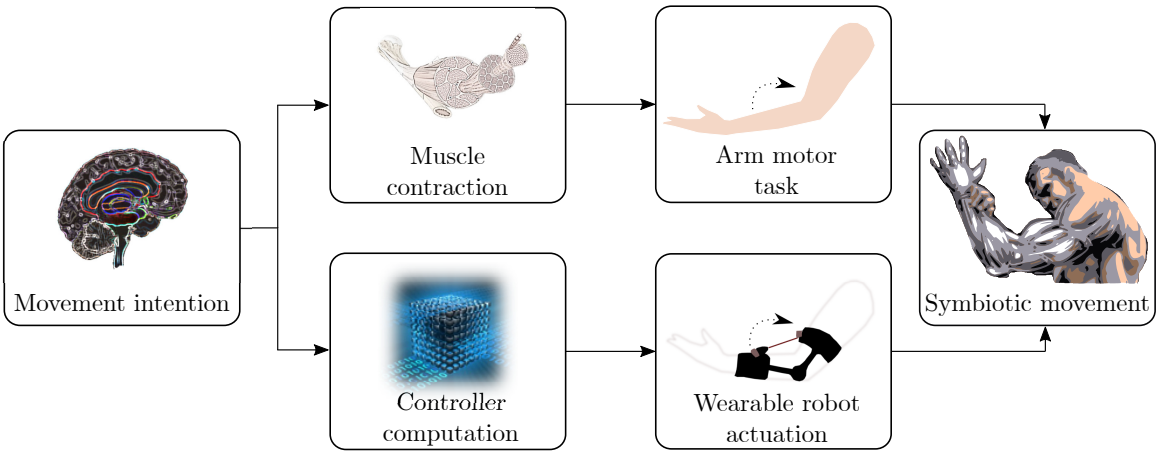

Figure 1 *Human-machine symbiosis*

disorders, causing significant health and cost issues (Iden, 2017). These health issues cause a huge financial burden for companies and healthcare system. In the worst cases, WRMDs could become chronic, with drastic consequence for the quality of life of the worker. Most disorders are related to repetitive movements, including also overhead tasks and awkward body postures (Grieve and Dickerson, 2008).

In the last few years, several companies started to develop and commercialize wearable upper limb exoskeletons to improve condition for workers in order to reduce musculoskeletal injuries: examples of commercially available upper-limb exoskeletons for workers are EksoVest (EksoBionics, Richmond, California, USA), Airframe (Levitate Technologies, San Diego, California, USA), ShoulderX (SuitX Emeryville, California, USA), PAEXO (Ottobock, Duderstadt, Germany), and Skel'Ex (Skel'Ex, Rotterdam, The Netherlands). All these devices have the aim to augment human performance and assist the movement, by reducing the effort of the user.

Robot devices are also increasingly being used in neurorehabilitation therapies, specially on disorders related to the central nervous system: disorders related to age, spinal cord injuries, multiple sclerosis, traumatic brain injuries, cerebral palsies and strokes induce a loss of arm dexterity in manipulating and communicating. Various strategies have been explored to improve motor recovery and they found that the best outcomes is in the acute phase of recovery (Bütefisch et al., 1995; Kwakkel et al., 2004; Van Peppen et al., 2004). For these treatments, robots assistance can increase the intensity of practice and relieve therapists from the demanding task of manually assisting the patient. Robot-assisted therapy has shown encouraging results, comparable to the ones achieved with traditional therapy (Klamroth-

Marganska et al., 2014), while allowing greater patient compliance and a quantitative, more accurate monitoring of the subject's performance.

Unfortunately, currently available robotic platforms are not logistically capable of following the patient after discharge from physical therapy. Patients go back home, training stops and their conditions plateau or even deteriorate.

Motivation and aim of the thesis

Robots are currently used to enable stroke survivors to perform intensive training under the influence of assistive forces. However, present-generation devices often use simple and fixed strategies, with little or no account for the patient's residual functions. One potential way to personalise treatment is to explicitly take the residual muscle activation into account.

Through EMG signals, it is possible to estimate the force generated by a particular muscle or use it as an input to control a robotic device in order to provide assistance in a symbiotic way. The development of a myoprocessor, a real-time module that estimates the force of a muscle or a group of muscles through a model-based approach, is an open challenge that could have a strongly impact both in daily activities, industry and rehabilitation.

This thesis work had the following scientific and technological objectives:

- to develop a biomechanical model of the musculoskeletal system, which allows to estimate the forces generated by each muscle in real-time

- to create a human machine interface (HMI) on a elbow exosuit that can adapt the assistance to different load and velocity conditons by keeping trasparent the exosuit's intrinsic dynamics and the external mechanical loads to the individuals' musculoskeletal systems

- to use the myocontrol module on a planar robot manipulandum to add a virtual muscle that can modify neuromuscular control in order to study its adaptivity.

The last aim required that the myoprocessor reliably estimated the muscle torque in each explored arm configuration. This implied a robust modelling of muscle contraction dynamics and muscle kinematics on a biomechanical point of view. The only way to achieve the proposed aims was to estimate the joints torques produced by the muscle by using an accurate and complex model-based approach.

Outline of the thesis

The first part of the work is an overture: the aim is to provide insight about the field of my PhD project. Chapter 1 is a brief introduction on myoelectric control and its applications. Chapter 2 presents an historical digression on the musculoskeletal modeling. This section describes the different approaches presented in literature by highlighting their limitations.

In part II I describe the approach taken in order to develop a real-time myoprocessor module for use in conjunction with a planar robot manipulandum. During my PhD project I developed myoprocessor modules with increasing level of biomechanical realism and computational complexity (Chapter 3, 4, 5). Real-time implementation is also addressed here (Chapter 6).

Part III discusses two applications for the myoprocessor framework: in Chapter 7 I describe how to control a soft wearable exoskeleton (exosuit) with a myoprocessor in order to partly compensate for user effort. In Chapter 8 I combine a myoprocessor module with the planar robot manipulandum in order to apply force field that mimics the contribution of an individual muscle. The aim is to study the modularity and the adaptivity of the musculoskeletal system.

The last Chapter draws general conclusions on the work, highlights our major contributions and elaborates on the open questions and paths for future work.

Part I

Model-based myoelectric control

Chapter 1

Introduction to myoelectric control and musculoskeletal modeling

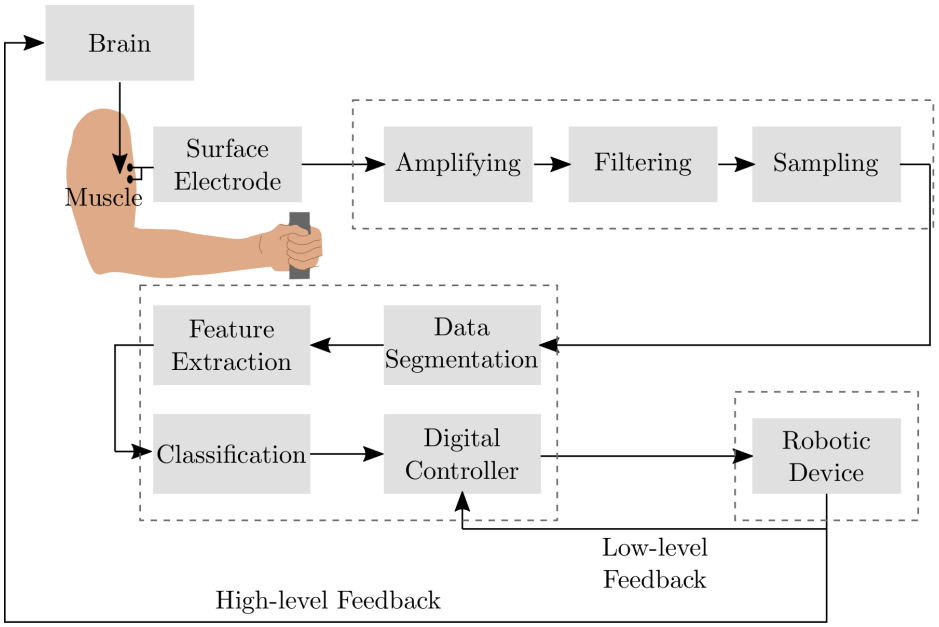

Figure 1.1 *Myoelectric control pattern recognition*. Image adapted from (Asghari Oskoei and Hu, 2007)

Myoelectric control approaches allow to detect movement intentions from the recorded movement and EMG signals. This intention detection can be used as an input to control a robot device (Cavallaro et al., 2006) or, more in general, as a human-machine interface (Ferreira et al., 2008). Myoelectric control can be divided in two main approaches: classification algorithm and model-based approach.

The efficiency of classification is important to validate the model (Hudgins et al., 1993), and the best compromise between efficiency and computational cost (Asghari Oskoei and Hu, 2007) must be identified. Englehart et al. (Englehart and Hudgins, 2003) developed a real-time myoelectric controller for the upper limb based on the wavelet classification: this approach is efficient, but it was tested using only two channels for movements and four channels for the EMG activity.

In the literature there are many works focused on the myoelectric control: Nielsen et al. (Nielsen et al., 2011) trained a neural network to estimate force in the bilateral mirror training. With this approach, they estimated the parameters of an amputated arm based on the activity of the other one (Jiang et al., 2012). One limitation of this approach is the different crosstalk between the amputated arm and the intact limb. The first has more crosstalk, so the signal is noisier but it was a good compromise with respect to the reinnervation technique (Kuiken et al., 2009). However, classification algorithm works only under training and are bounded to the training workspaces.

The second approach - i.e. model-based approach - has the aim at reconstructing the joint torque by using detailed musculoskeletal model. Musculoskeletal models can estimate the muscle force through mathematical relationships that model the dynamics of excitation and contractile behavior. In this way, it is possible to generalise the control through a muscle force estimation. Several studies demonstrated that a model-based real-time framework is robust enough to control prosthesis (Sartori et al., 2019) and rigid exoskeleton (Durandau et al., 2019), both in physiological and pathological cases. Since my work is focused on specific applications that are described in the following chapter, here I only focus on musculoskeletal modelling approach.

Chapter 2

Musculoskeletal modeling

2.1 Muscle contractile behavior

The muscle unit is composed by a group of muscle fibers. These fibers can be arranged along the direction of the tendon - i.e. parallel muscle fibers - or along a specify direction - i.e. pennated fibers. The angle between the pennated fibers and the tendon is called pennation angle ϕ. Pennates fibers are connected to the aponeurosis of the muscle, which is also called the inner portion of the tendon because its properties appear identical to the properties of the "external" portion of the tendon.

To understand muscletendon mechanics, the effect of pennation on musculotendon function can be ascertained from the arrangement shown in Fig. 2.1 by assuming the muscle is isovolumic and the distance between the aponeurosis of origin and insertion is constant. Specifically, the major effect is that ϕ, the orientation of muscle fibers to tendon, increases as fibers shorten.Thus, muscle fibers shorten in a direction that is not colinear with the direction in which tendon stretches (Fig. 2.1 red arrows). Though, this planar representation may also convey the notation that the longitudinal forces in tendon act to rotate muscle fibers, such effects on moving the body segments are believed to be either nonexistent or secondary to effects caused by the longitudinal forces. The muscle fiber of length L^M comprises a series of sarcomeres that have the same length. During muscle contraction, the sarcomeres are excited simultaneously to generate muscle strength. The sarcomere, in turn, encloses filaments of actin and myosin which, through mutual sliding, cause the shortening of the fiber. The motor unit comprised a series of muscle fibers that are innervated by the same motor neuron. The motor unit is the smallest functional unit associated to the muscle contraction. Motor units are recruited based their size (size principle, (Henneman et al., 1965)) and the force that can be produced: the type I motor unit, the first recruited, are slow, little and they are resistant

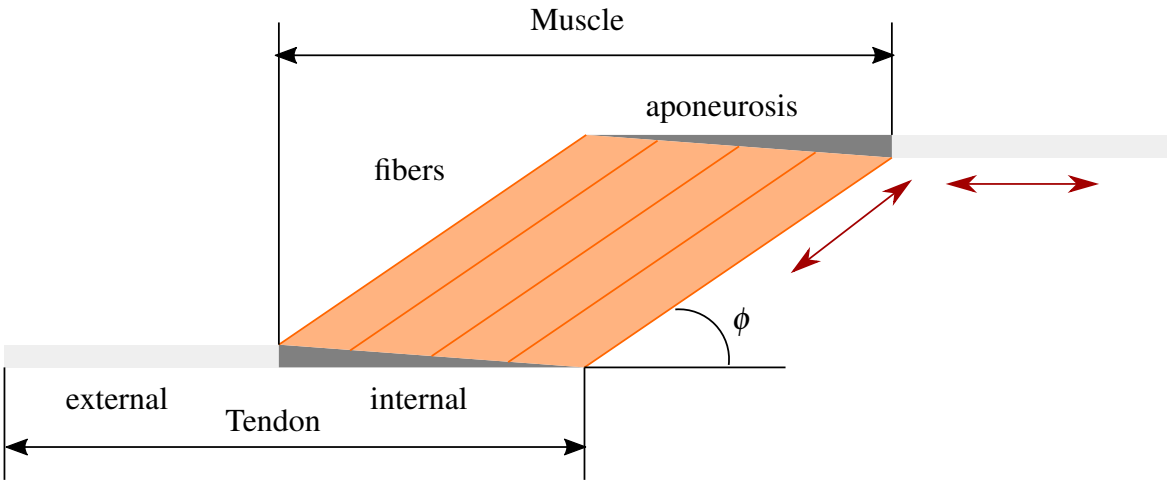

Figure 2.1 *Relation among muscle fibers and tendon in a pennated muscle*. Muscle fibers have the same length and are oriented at some ϕ to the tendon axis of pull. Functionally, tendon can be considered to consist of an internal portion (i.e. the aponeurosis of muscle origin and insertion) and external portion. As muscle fibers shorten, muscle is assumed to mantain isovolume, tendon to move onli along its axis, and fibers to become more pennated (i.e. ϕ increases (Zajac, 1989).

to fatigue. When it is necessary to increase the muscle force, the type IIa motor units are recruited. Finally, there are the type IIb motor units that are the strongest, fastest and more fatiguing motor units. The central nervous system can control the number of the motor units and the activation frequency in order to generate the desired force (Zajac, 1989). In a muscle there are several motor unit that control the contraction, but to simplify the problem, classical muscle modeling approximates the whole muscle with a single fiber controlled by a single motor neuron (i.e. a single-fiber motor unit).

Muscle dynamic behavior results from the combination of two distinct processes: activation and contraction. Activation dynamics converts neural activation, that can be detected by using EMG techniques, into muscle fiber recruitment. Contraction dynamics converts the muscle fiber recruitment into muscle force.

2.2 Dynamic contraction modeling

Several musculoskeletal models derive from the one introduced by A. V. Hill (Hill, 1938). He modeled the muscle fiber as the combination of a contractile (CE) and a series (SE) element, as shown in Fig. 2.2.

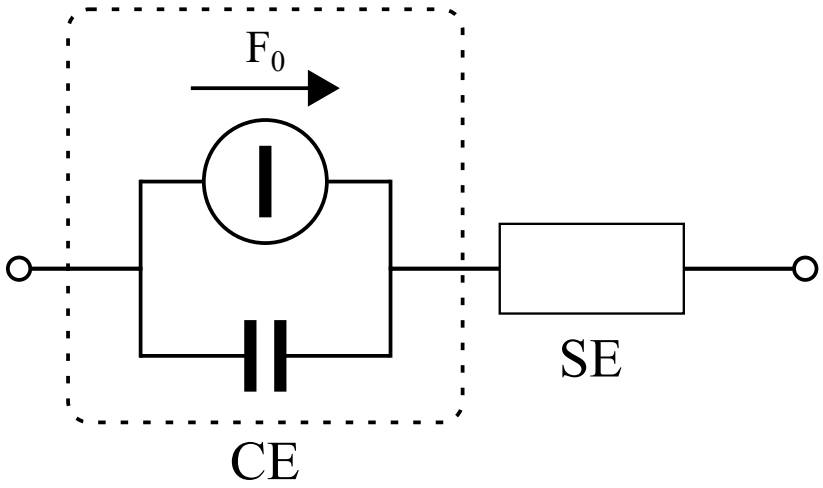

Figure 2.2 *Hill musculoskeletal model.*

The contractile element has a force generator and a damping element. The dynamic equation to obtain the muscle fiber force F is

$$F(t) = F_0^M - \frac{a + F_0^M}{b + \dot{L}} \dot{L} \tag{2.1}$$

where F_0^M is the maximum isometric force, $\dot{L}$ is the contraction fiber velocity and a, b are model parameters (a: heat of shortening; b: rate of energy liberation). Eq. 2.1 includes the muscle thermodynamics. The series element models the instant contraction dues to the muscle stiffness through the relationship

$$F(t) = -k(F)\Delta L \tag{2.2}$$

This model presents some limitations. It studies only the concentric dynamics, by ignoring the eccentric ones. With this model is possible to analyze only the maximum isometric contraction situation -i.e. tetanic contraction-. This condition is limited to a very limited range. Finally, the model does not include the tendon contribution and the calcium kinetics.

The "Hill-based" models evolve the paradigms introduced by the Hill model by generalizing Eq. 2.1 and 2.2 in order to extended them to other conditions, such as eccentric contraction and non-maximum activation.

2.2.1 Zajac Model

The work of Felix Zajac model (Zajac, 1989) is a milestone of musculoskeletal modeling. It extends the Hill model by considering the entire muscle (not only the single muscle fiber), taking into account also the tendon contribution. The purpose of this model is to estimate muscle-tendon force starting from muscle activation. Muscle and tendon are a single actuator that provides movements in conjunction with the dynamics of the body (see Fig. 2.3. The dynamics directly influences the muscle-tendon length and its velocity contraction: these values depending by the body movement and position. Body kinematics, instead, depending by the muscle-tendon force. Given an excitation signal $u(t)$ we can obtain the corresponding activation signal through the activation dynamics that models the calcium channels opening. Through the muscle activation $a(t)$, combining with the muscle length $L^M(t)$ and the fiber velocity contraction $v^m(t)$, is possible to obtain the muscle force $F^M(t)$, that corresponds also to the tendon force $F^T(t)$. The tendon length $L^T(t)$ and its time derivative v^T are computed by using the muscle force. These two values close the loop of the scheme, as shown in Fig. 2.3;

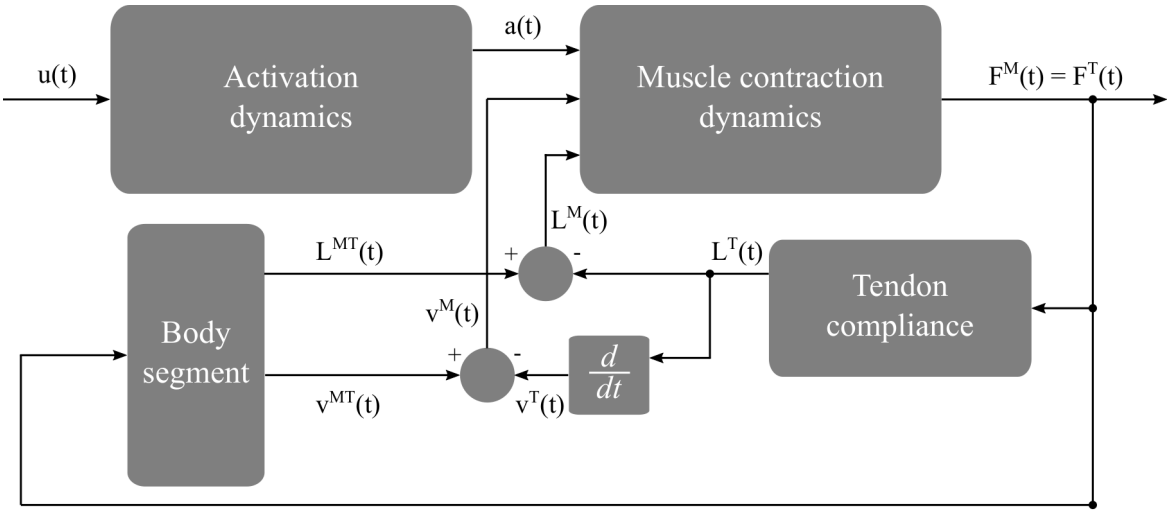

Figure 2.3 *Zajac musculoskeletal model*. Image adapted from (Zajac, 1989)

2.2.2 Rosen-Fuchs-Arcan model

The Rosen-Fuchs-Arcan model (Rosen et al., 1999) was developed to estimate elbow joint torque during an elbow flexion-extension. The movement was performed along the sagittal plane by using an upper limb exoskeleton to record elbow position. The authors extended Hill model by adding EMG signals to obtaine a reliable torque reconstruction. The model

comprised three blocks: the contractile element (CE), the series element (SE) and the parallel element (PE). SE and PE represent, respectivetely, the passive component of the tendon and the passive fiber tissue. Blocks are connected as shown in figure 2.4

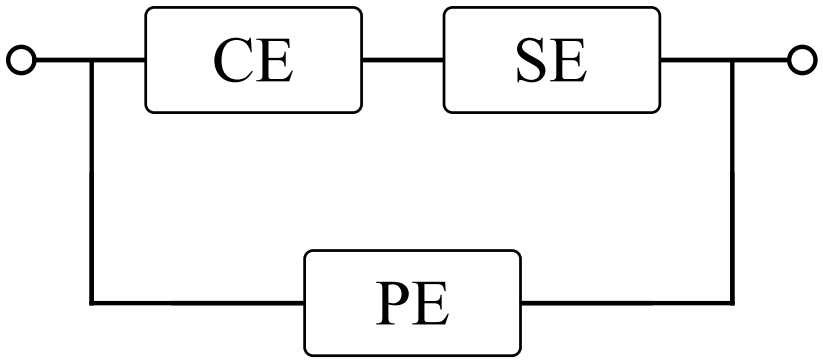

Figure 2.4 *Rosen-Fuchs-Arcan musculoskeletal model*. Image adapted from (Rosen et al., 2001)

The force-extension relationship of these tissues is defined by the following equations:

$$F^{SE}(t) = \frac{F^{SE}_{max}}{e^{SE_{sh}}}(e^{SE_{sh}\Delta L^{SE}(t)/\Delta L^{SE}_{max}} - 1) \tag{2.3}$$

$$F^{PE}(t) = \frac{F^{PE}_{max}}{e^{PE_{sh}}}(e^{PE_{sh}\Delta L^{PE}(t)/\Delta L^{PE}_{max}} - 1) \tag{2.4}$$

$F^{SE}(t)$, $F^{PE}(t)$ are the SE and PE forces, $\Delta L^{PE}(t)$, $\Delta L^{SE}(t)$ are the extensions of the corresponding element and SE^{sh}, PE^{sh} are shape factors. Finally, the CE component represents the muscle fiber activity, that is characterized by two relationship: the force-length f_l and the force-velocity f_v relationship.

$$F^{CE}(t) = f_v(V^{CE}(t)) \cdot f_l(L^{CE}(t)) \cdot F^{CE}_{max} \cdot u(t) \tag{2.5}$$

where $V^{CE}(t)$ and $L^{CE}(t)$ are the fiber velocity contraction and the fiber length and $u(t)$ is the normalized activation level.

The force-length relationship f_l is a decreasing exponential function that depends by the CE element length normalized respect to the resting length.

$$f_l(t) = e^{-0.5((L^{CE}(t)/L^M_0 - 1.05)/0.19)^2} \tag{2.6}$$

The f_v relationship is bounded to the fiber velocity contraction normalized respect to its maximum value.

$$f_v(t) = \frac{0.1433}{0.1074 + e^{-1.409\sinh(3.2V^{CE}(t)/V^M_{max}+1.6)}} \tag{2.7}$$

The inputs of the model are the activation level of the motor unit and the elbow joint position and the output is the joint torque. The force generated by the contractile element is the same of the series element ($F^{CE-SE}(t) = F^{CE}(t) = F^{SE}(t)$) and the muscle force is the sum between F^{CE-SE} and F^{PE} ($F^M(t) = F^{CE-SE}(t) + F^{PE}(t)$).

2.2.3 Lloyd-Besier model

The Lloyd-Besier model (Lloyd and Besier, 2003) evolves the Zajac model and was originally developed to estimate the net torque at the knee level through an inverse dynamics approach. Respect to Rosen (Rosen et al., 2001) that limits the study to the biceps, the triceps and the brachioradialis, this model takes into account 13 muscle-tendon units, by using simpler equations but exploring a huger case. The force generated by each unit is estimated through the force-length $f_l(t)$, the force-velocity $f_v(t)$ and the parallel passive elastic force–length $f_p(t)$ relationships. The curves are normalized respect to the maximum isometric force F_0^M, optimal fibre length L_0^M, and maximum muscle contraction velocity v_{max}^M. The force-length relationship $f_l(t)$ is obtained by a cubic spline interpolation of normative data points, $f_v(t)$ is taken from (Schutte et al., 1993) and $f_p(t)$ is obtained from an exponential relationship. The general equation to estimate the muscle-tendon force ($F^{MT}(t)$) is

$$\begin{aligned} F^{MT}(t) &= F^T(t) \\ &= F_0^M[f_l(t) \cdot f_v(t) \cdot a(t) + f_p(t)] \cdot \cos(\phi(t)) \end{aligned} \tag{2.8}$$

where $\phi(t)$, the pennation angle, depended by the muscle length $L^M(t)$, the muscle optimal fiber length L_0^M and by its value at the muscle optimal fiber length (ϕ_0):

$$\phi(t) = \arcsin\left(\frac{L_0^M \sin(\phi_0)}{L^M(t)}\right) \tag{2.9}$$

The muscle activation level a_j for the muscle-tendon unit j derives from the excitation level u_j through a non-linear shape factor $A(-3 < A < 0)$

$$a_j(t) = \frac{e^{Au_j(t)} - 1}{e^A - 1} \tag{2.10}$$

The muscle fibre lengths is calculated by forward integration of the fibre velocities obtained from the force–velocity and force–length relationships using a Runge-Kutta–Fehlberg

algorithm (Fehlberg, 1968). To obtain the net torque at the knee level, the muscle-tendon force of each unit is multiplied by the corresponding moment arm and the vectorial sum provides the model output.

2.2.4 Thelen model

The Thelen model (Thelen, 2003) is an evolution of Zajac model. It was developed to study the lower limb dynamics, by focusing on the ankle joint torque estimation. The activation dynamics and contraction dynamics follow two non-linear first order differential equations. There are two time constants for the activation dynamics: one faster for the activation ($\tau_{act} = 10$ ms) and one slower for the deactivation ($\tau_{deact} = 40$ ms). The contraction dynamics models the relationship between the force-length relationship of the contractile element and the elastic properties of the tendon element. The forces are normalized respect to the maximum isometric force F_0^M and the lengths respect to the optimal fiber length L_0^M. I report the normalized element with a ' ~ ' respect to the non-normalized ones (e.g.: $a(t)$, $\tilde{a}(t)$).

The model output is the muscle-tendon force $F^{MT}(t)$ (see Fig. 2.5). It use as inputs the EMG signals and the muscle fiber length $L^M(t)$. From the EMG signals $u(t)$ is possible to obtain the activation level $a(t)$) as

$$\dot{a}(t+\Delta t) = \begin{cases} (u(t)-a(t))/\tau_{act}, & u(t) \geq a(t) \\ (u(t)-a(t))/\tau_{deact}, & u(t) < a(t) \end{cases} \tag{2.11}$$

The muscle fiber has two elements: the contractile element and the passive element. The tendon force is the same generated by the muscle element, so we have $F^{MT}(t) = F^M(t) = F^T(t)$. The normalized passive force $\tilde{F}^{PE}(t)$ is described by the equation

$$\tilde{F}^{PE}(t) = \frac{e^{k^{PE}(\tilde{L}^M(t)-1)^2/\varepsilon_0^M} - 1}{e^{k^{PE}} - 1} \tag{2.12}$$

where $k^{PE}$is a shape factor and ε_0^M is the passive strain due to the maximum isometric force ($\varepsilon_0^M = 0.6F_0^M$).

The tendon force $\tilde{F}^T(t)$ is computed as

$$\tilde{F}^T(t) = \begin{cases} \frac{\tilde{F}_{toe}^T}{e^{k_{toe}}-1}(e^{k_{toe}\varepsilon^T(t)/\varepsilon_{toe}^T} - 1), & \varepsilon^T \leq \varepsilon_{toe}^T \\ k_{lin}(\varepsilon^T(t) - \varepsilon_{toe}^T) + \tilde{F}_{toe}^T, & \varepsilon^T > \varepsilon_{toe}^T \end{cases} \tag{2.13}$$

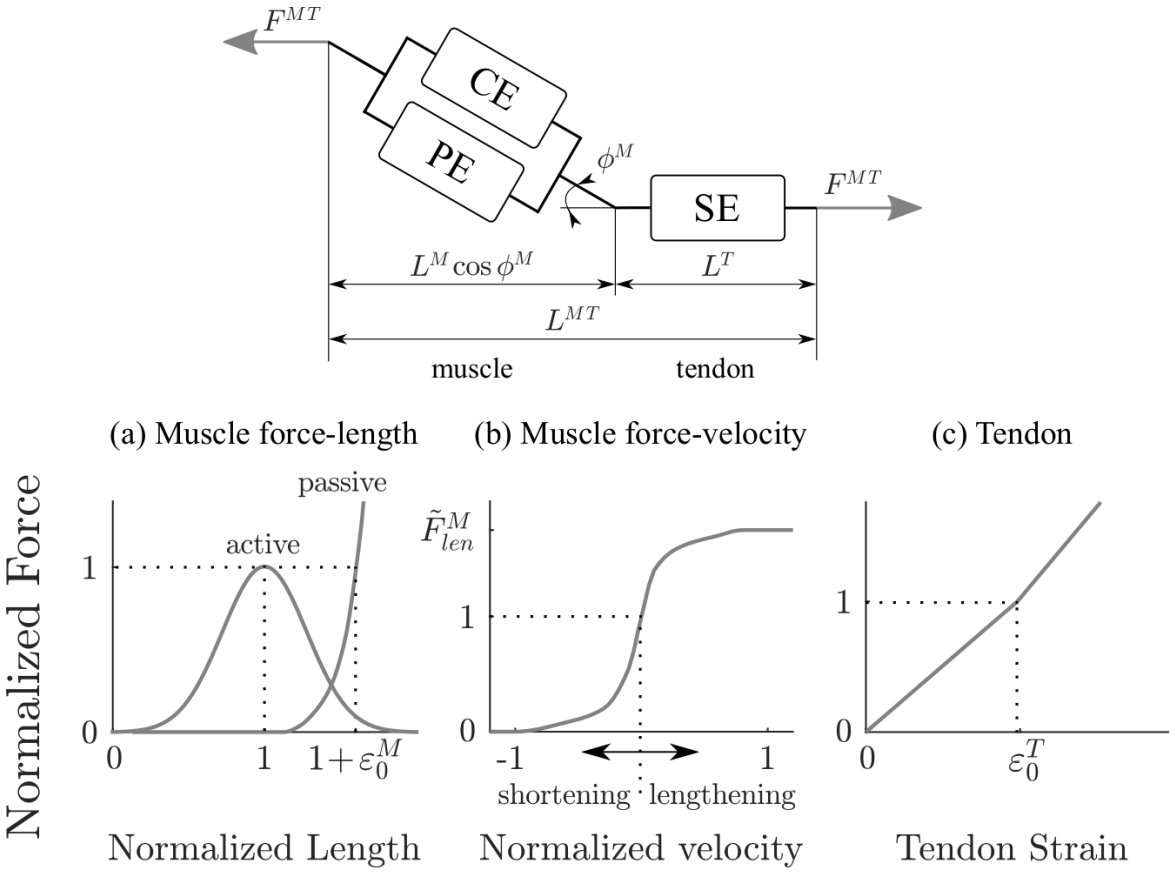

Figure 2.5 *Thelen model muscle-tendon scheme*. Panel (a) shows the force-length relationship and the passive element curve. Panel (b) represents the force-velocity relationship and panel (c) the tendon curve (Thelen, 2003). Image adapted from (Thelen, 2003)

where $\varepsilon^T(t)$ is the tendon strain, ε_{toe}^T is the strain when the tendon is in the linear range, k_{lin} is a scale factor and F_{toe} is the maximum tendon force in its linear range. The contractile element force is obtained as

$$F^{CE}(t) = \frac{F^T(t)}{\cos\alpha(t)} - F^{PE}(T) \tag{2.14}$$

The force-length relationship is modeled as a Gaussian function

$$f_l(t) = e^{-(\tilde{L}^M(t)-1)^2/\gamma} \tag{2.15}$$

the fiber contraction velocity is computed as

$$V^M(t) = (0.25 + 0.75a(t))V_{max}^M \frac{\tilde{F}^{CE}(t) - a(t)f_l(t)}{b(t)} \tag{2.16}$$

$$b(t) = \begin{cases} a(t)f_l(t) + \tilde{F}^{CE}(t)/A_f, & \tilde{F}^{CE}(t) \leq a(t)f_l(t) \text{ shortening} \\ \frac{(2+2/A_f)(a(t)f_l(t)\tilde{F}^M_{len} - \tilde{F}^{CE})(t)}{\tilde{F}^M_{len}-1}, & \tilde{F}^{CE}(t) > a(t)f_l(t) \text{ lengthening} \end{cases} \tag{2.17}$$

$\tilde{F}^M_{len}$ is the maximum normalized force produced by the fiber during lengthening and A_f is a shape factor. Finally, the tendon length is obtained as $L^T(t) = L^{MT}(t) - L^M(t)\cos\alpha(t)$.

2.3 Muscletendon kinematics modeling

Musculoskeletal modeling and simulations require accurate estimates of musculotendon kinematics including musculotendon length (L^{MT}) and moment arms (J^M) to accurately predict musculotendon forces (F^{MT}) and joint moments. It is necessary to not have discontinuities in the predicted musculotendon kinematics (Gao et al., 2002; Garner and Pandy, 2000) by using equation function that are continuosly differentiable.

2.3.1 Estimation of musculotendon kinematics as function of joint angles

Pigeon *et al.* modeled musculotendon lengths and moment arms of human upper limb muscles through polynomial functions of n coefficients that took joint angles as input (Pigeon et al., 1996). They obtained the musculotendon length equations using anatomical and model data and they derived them to estimate the moment arms. L^{MT} and J^M for the $j-$muscle were described by the equations

$$L^{MT}_j = k_{j0} + \sum_{i=1}^{nDoF} (k^j_{i1}q_i + k^j_{i2}q_i^2 + \cdots + k^j_{in}q_i^n) \tag{2.18}$$

$$J^M_j = \sum_{i=1}^{nDoF} (k^j_{i1} + k^j_{i2}q_i + \cdots + k^j_{in}q_i n - 1) \tag{2.19}$$

where q_i is the angle value for the $i-$joint, $nDoF$ the degrees of freedom of the considered joints and $k^{i1}, \ldots, k^j_{in}$ is the sequence of the polynomial k coefficients. Table 2.1 shows the coefficient k for the upper limb muscles and Fig. 2.6the muscle length trend for the elbow joint muscles.

Muscle	k_{S0} [m]	k_{E0} [m]	k_{E1} [m/rad]	k_{E2} [m/rad^2]	k_{E3} [m/rad^3]	k_{E4} [m/rad^4]	k_{E5} [m/rad^5]
pectoralis major	-0.051	0	0	0	0	0	0
anterior deltoid	-0.033	0	0	0	0	0	0
posterior deltoid	0.079	0	0	0	0	0	0
long head of biceps	0	-0.015	-0.026	-0.006	0.006	0	0
sort head of biceps	-0.029	-0.015	-0.026	-0.006	0.006	0	0
long head of ticeps	0.025	0.023	0.017	-0.042	0.037	-0.014	0.002
medial head of triceps	0	0.023	0.017	-0.042	0.037	-0.014	0.002
brachioradialis	0	-0.020	-0.010	-0.033	0.012	0	0

Table 2.1 *Normative muscle geometry parameters* (Pigeon et al., 1996)

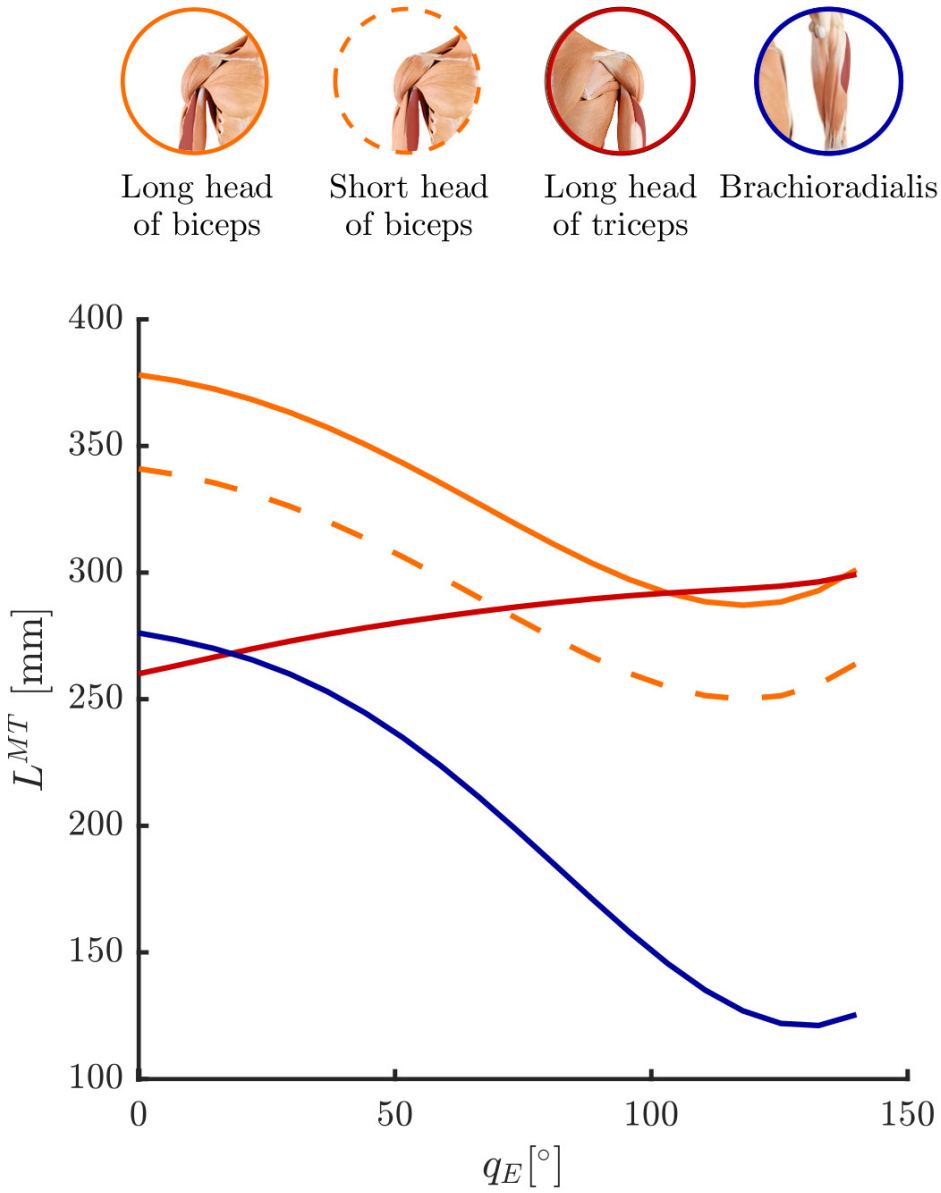

Figure 2.6 *Muscle-tendon length trend by following Pigeon model* (Pigeon et al., 1996).

2.3.2 Estimation of musculotendon kinematics using multidimensional B-spline

Sartori *et al.* used instead of a single function per muscle, a set of differentiable polynomial equations to estimate musculotendon kinematics. In particular, they opted for continuously differentiable multidimensional cubic splines (Sartori et al., 2012) based on estimates of musculotendon lengths L^{MT} obtained for different body configurations. These lengths were

extracted from musculoskeletal geometry models using Opensim (Delp et al., 2007). They developed, tested, and validated the method on lower limb muscle models (Delp et al., 1990; Winby et al., 2009). A cubic spline consists of a series of third-order polynomials spliced together to preserve continuity of the first and second-order derivatives. The points at which polynomials are spliced together are called nodes and they respect the relationship

$$a = x_0 < x_1 < \cdots < x_n = b \tag{2.20}$$

where a and b are the lower bound and the upper bound of the interval $\Gamma_n \in \mathbb{R}$. A spline $s(x)$ with $n+1$ nodes can be interpolated from the nominal data y as a linear combination of $n+3$ cubic polynomials $u_1, u_2, \ldots, u_{n+3}$

$$s(x) = \sum_{i=l}^{m} c_i u_i(x) \tag{2.21}$$

where c_i are the coefficients, $m = \min(l+3, n+3)$, $l = \left[\frac{x-a}{h}\right]$ and h is the distance between nodes. If $s_j(x)$ represents the musculotendon length of the $j-$muscle, the corresponding moment arm J_j^M will be

$$J_j^M = \frac{ds(x)}{dx} \tag{2.22}$$

It is possible to extend the spline formulation described above to a multidimensional case of dimension d (Habermann and Kindermann, 2007) by taking d different grids $\Delta_1, \Delta_2, \ldots, \Delta_d$ and the corresponding interpolation data $y_1, \ldots, y_d$. If n_i is the number of nodes in Δ_i and $c_{i_1 i_2 \ldots i_d}$ the spline coefficients, the spline function $s_d(x)$ can be written as

$$s_d(x) = \sum_{i_1=1}^{n_1+3} \cdots \sum_{i_d=1}^{n_d+3} c_{i_1 i_2 \ldots i_d} \cdot \prod_{j=1}^{d} u_{i_j}^j \left(x^j\right) \tag{2.23}$$

The moment arm for a multi joint muscle corresponds to the partial derivative of the musculotendon length L^{MT} respect to the q_k joint

$$J_j^M = \frac{\partial L^{MT}}{\partial q_k} = \frac{\partial s_d(x)}{\partial q_k} \tag{2.24}$$

Fig. 2.7, 2.8 and 2.9 show respectively the musculotendon length, the shoulder moment arm and the elbow moment arm of the long head of the biceps computed by using multidimensional cubic b-spline technique.

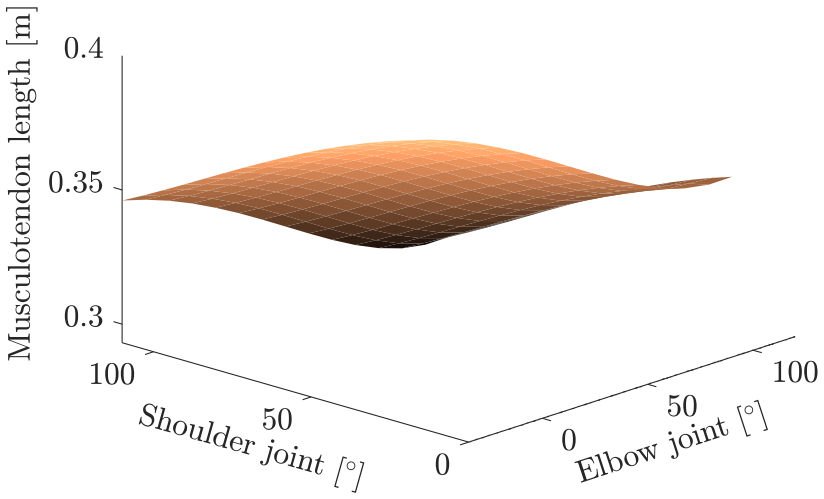

Figure 2.7 *Musculotendon length of the long head of the biceps computed through multidimensional cubic bi-spline*

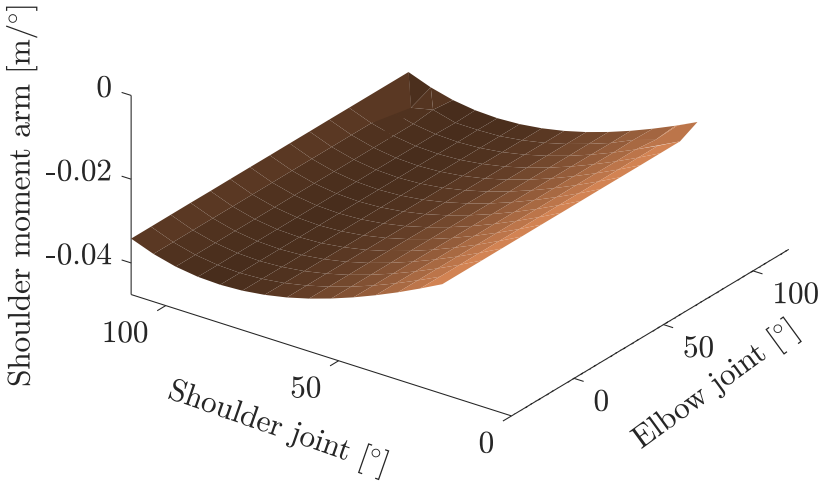

Figure 2.8 *Musculotendon shoulder moment arm of the long head of the biceps computed through multidimensional cubic bi-spline*

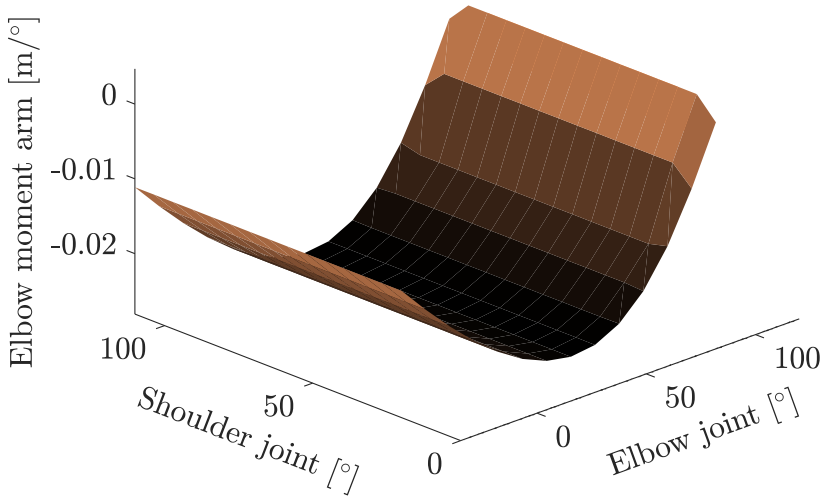

Figure 2.9 *Musculotendon elbow moment arm of the long head of the biceps computed through multidimensional cubic bi-spline*

2.3.3 Net torque computation

The projection of the muscle force $F^M(t)$ at the joint level can be obtained by combining it with the moment arm J^M in order to compute the muscle torque τ^M

$$\tau^M(t) = J(q(t))^T \cdot F^M(t) \tag{2.25}$$

Finally, the net torque $\tau^{net}(t)$ is the sum between all muscle torques.

$$\tau^{net}(t) = \sum_{j=1}^{nMuscles} \tau_j^M(t) \tag{2.26}$$

Part II

Myoprocessor module

The myoprocessor is a Real-time EMG-driven model that estimates the human joints torque starting from the EMG signals and the joints kinematics. The torque estimation is obtained from detailed biomechanical models and it can be used to control a device. Myoprocessor is a Human Machine Interface that directly connects the human musculo-nervous system with a target to control. The myoprocessor needs to be calibrated on each subject in order to obtain the most reliability on a biomechanical point of view.

During my PhD, I developed several versions of the myoprocessor module, that can be summarized in three main versions:

1. Proportional myoprocessor module
2. Hill-based myoprocessor module: preliminary version
3. Hill-based myoprocessor module: final version

The first module was a proportional myoprocessor (Chapter 3) that estimated the muscle torque in isometric conditions. Here the calibration involved the muscle geometry, modelled through polynomial function with free coefficients.

The second version included an Hill-based myoprocessor module (Chapter 4) that can describes the contraction aspect related to the arm movement that the proportional model was not able to capture. However, the polynomial estimation of muscle geometry did not reliable estimate the muscle length and the moment arm of each muscle and, for this reason, I changed my approach to the last version of the myoprocessor module.

This last version (Chapter 5) keeps the same Hill-based model structure of the version 2, but estimates the muscle geometry by scaling normative musculoskeletal models in order to match subjects anthropometric sizes.

Chapter 3

Proportional myoprocessor module[1]

As first step in the myoprocessor development, I decided to focus on musculoskeletal geometry identification. For this study I took into account 8 muscle-tendon units: anterior and posterior deltoid, the long and the short head of the biceps, the long and the medial head of the triceps, brachioradialis and the pectoralis major. To simplify the problem, I assumed that in isometric conditions the muscle force was proportional to the muscle activation, $u(t)$, defined as the envelope of the EMG signal:

$$F^M = A \cdot u \tag{3.1}$$

where A is a diagonal matrix with $a_{ii} = F^i_{max}/U^i_{max}$. Parameter vectors F^i_{max} and U^i_{max} are, respectively, the maximum isometric force and maximum activation for the i muscle.

3.1 Muscle geometry and force capability

The joint torque τ_m is calculated as

$$\tau_m = J_m(q)^T \cdot f_m \tag{3.2}$$

where $J_m(q)$ is the moment arms matrix of the muscle-tendon complex and q is the upper limb configuration (vector of shoulder and elbow angles). The moment arms matrix $J_m(q)$ is composed by the Jacobian vector of the muscle lengths. Each $i-$row j_i contains the partial

[1] *Partial content of this Chapter has been published as* Lotti N. and Sanguineti V. Toward emg-controlled force field generation for training and rehabilitation: From movement data to muscle geometry. *International conference on Rehabilitation Robotics* (ICORR), 17-20 July 2017, London (UK).

derivatives of the muscle-tendon length L^{MT_i} of the muscle i respect to the shoulder angle q_S and the elbow angle q_E.

$$j_i = \begin{bmatrix} \frac{\partial L^{MT_i}}{\partial q_S} & \frac{\partial L^{MT_i}}{\partial q_E} \end{bmatrix} \tag{3.3}$$

I tested three different models to estimate muscle geometry. On the first one, I assumed the moment arms constants with respect to arm configuration. The rows j_i of J_m were

$$j_i = \text{constant} \tag{3.4}$$

This corresponds to assuming that muscle lengths change linearly with joint rotations. Maximum muscle force and moment arms always appear multiplied together, thus the model parameters are in fact the moment arms times the peak muscle force. In conclusion, the model has two parameters for bi-articular muscles (the short head of the biceps and the long head of the triceps) and one parameter for mono-articular muscles, with a total of $2 \times 2 + 6 = 10$ parameters.

The second tested model of muscle geometry was based on cadaver and normative anatomical data: Pigeon et al (Pigeon et al., 1996) suggested that muscle lengths have a linear dependence on shoulder angle q_S and a polynomial dependence on elbow angle, q_E (up to 5-th order depending on muscle). Following Pigeon (Pigeon et al., 1996), the i-th row of $J_m(q)$, corresponding to the i-th muscle, can be calculated as

$$j_i = \begin{bmatrix} k_{S_i} & k_{E_{0_i}} + k_{E_{1_i}} q_E + k_{E_{2_i}} q_E^2 + k_{E_{3_i}} q_E^3 + k_{E_{4_i}} q_E^4 + k_{E_{5_i}} q_E^5 \end{bmatrix} \tag{3.5}$$

In a bi-articular muscles, the moment arm function is described by up to 7 parameters per muscle. In mono-articular muscles, there either one parameter for the shoulder muscle or six parameters for the elbow. This makes a total of $2 \times 7 + 3 \times 6 + 3 = 35$ parameters. I tested two variants of this model. In one case I used the normative estimates provided in (Pigeon et al., 1996) for each subject; see Table 2.1.

In this normative polynomial model, the only parameter is the vector of maximum force lengths, F_{max} – a total of 8 parameters. In a variant of the same model, I estimated the polynomial parameters for each subjects acquired. As in constant moment arms model, polynomial coefficients and peak muscle force always come multiplied together and cannot be estimated independently. This variant of the model has 35 parameters as calculated above. It is possible to obtain the muscle-tendon length for each muscle tendon unit by integrating the corresponding j_i respect to the joint angles. For the polynomial models the muscle tendon length L^{MT_i} for the $i-$muscle is

$$L^{MT_i} = \iint_{q_{S0},q_{E0}}^{q_{S1},q_{E1}} j_i \, dq_S dq_E \tag{3.6}$$

$$= k_{S_i} q_S + k_{E_{0_i}} q_E + k_{E_{1_i}} q_E^2 + k_{E_{2_i}} q_E^3 + k_{E_{3_i}} q_E^4 + k_{E_{4_i}} q_E^5 + k_{E_{5_i}} q_E^6 + L_{rest}^{MT_i} \tag{3.7}$$

where $L_{rest}^{MT_i}$ is the muscle-tendon length during the resting state. Fig.2.6 shows the muscle-tendon length trend of the short head of biceps, long head of biceps, long head of triceps and brachioradialis respect the elbow joint angle q_E by using the normative polynomial model.

As discussed above, I developed this myoprocessor to work in conjunction with a planar robot manipulandum: for this reason, another relevant quantity that I wanted to estimate were endpoint forces F_H^{MT} in order to compare them to the force generated by the robot F_H. Assuming that the torso and the wrist were blocked and that the arm only moves in the horizontal plane, were possible to uniquely determine the endpoint force F_H^{MT} from the joints torque τ_m as

$$F_H^{MT} = J(q)^{-T} \tau_m \tag{3.8}$$

where $J(q)$ is the Jacobian of the forward kinematics transformation $x = x(q)$, where x is hand position. Given the above assumptions we have:

$$J(q) = \begin{bmatrix} -L_U \sin q_S - L_F \sin(q_S + q_E) & -L_F \sin(q_S + q_E) \\ L_U \cos q_S + L_F \cos(q_S + q_E) & L_F \cos(q_S + q_E) \end{bmatrix} \tag{3.9}$$

where L_U and L_F are the upperarm and the forearm lengths.

3.2 Model calibration

I designed a motor task specifically aimed at parameters identification and test myoprocessor module. In this work I studied how limb and muscle geometry – the way endpoint position and muscle torque change with arm configuration – can be estimated from movement data and be used to extend the linear controllers used in (Berger et al., 2013; de Rugy et al., 2012) to reliably estimate isometric endpoint forces in various arm configurations.

3.2.1 Experimental Apparatus

The subjects sat in front of a $19''$ computer monitor placed vertically about 1 m away, at eye level. They grasped with their right hand the handle of a planar manipulandum with two degrees of freedom - see Casadio et al. (2006) for details. Torso and wrist were restrained. The robot handle included a support for the forearm, which partly compensated for the effect of gravity. A Force/Torque sensor (Gamma 130-10, ATI Industrial Automation, USA) was mounted on the robot handle to measure the interaction force between subject and robot. Seat position was adjusted so that, with the cursor pointing at the center of the workspace, the elbow and the shoulder joints were flexed about 90° and 45°. A multi-channel wireless EMG system (EMG Wave plus, Cometa srl, Italy) was used to record the muscle activity from selected muscles in the subject's right arm. The activity of seven muscles was recorded: anterior and posterior deltoid, the long and the short head of the biceps, the triceps, brachioradialis and the pectoralis major. As it is difficult to obtain separate EMG recordings for different parts of the triceps, I separately modelled long head and medial head of the triceps, but assumed that they are driven by the same activation. I used an additional electrode, placed on the sternum, to record the electrocardiography (ECG) signal. One infrared camera (Slim 13, Optitrack, NaturalPoint Inc, USA) placed above the robot workspace recorded the movements of three IR LED markers, placed on the subject's shoulder acromion and elbow joint and on the robot handle. The experimental set-up was controlled by two network-connected PCs, communicating through the UDP protocol. PC1 was responsible for the management of a software application, written in Simulink and based on the Real-Time Windows Target toolset, which was responsible for managing the experimental protocol, force recordings and robot control. PC2 was responsible for EMG and camera recordings and marker detection. Fig. 3.1 shows the setup of this experimental apparatus.

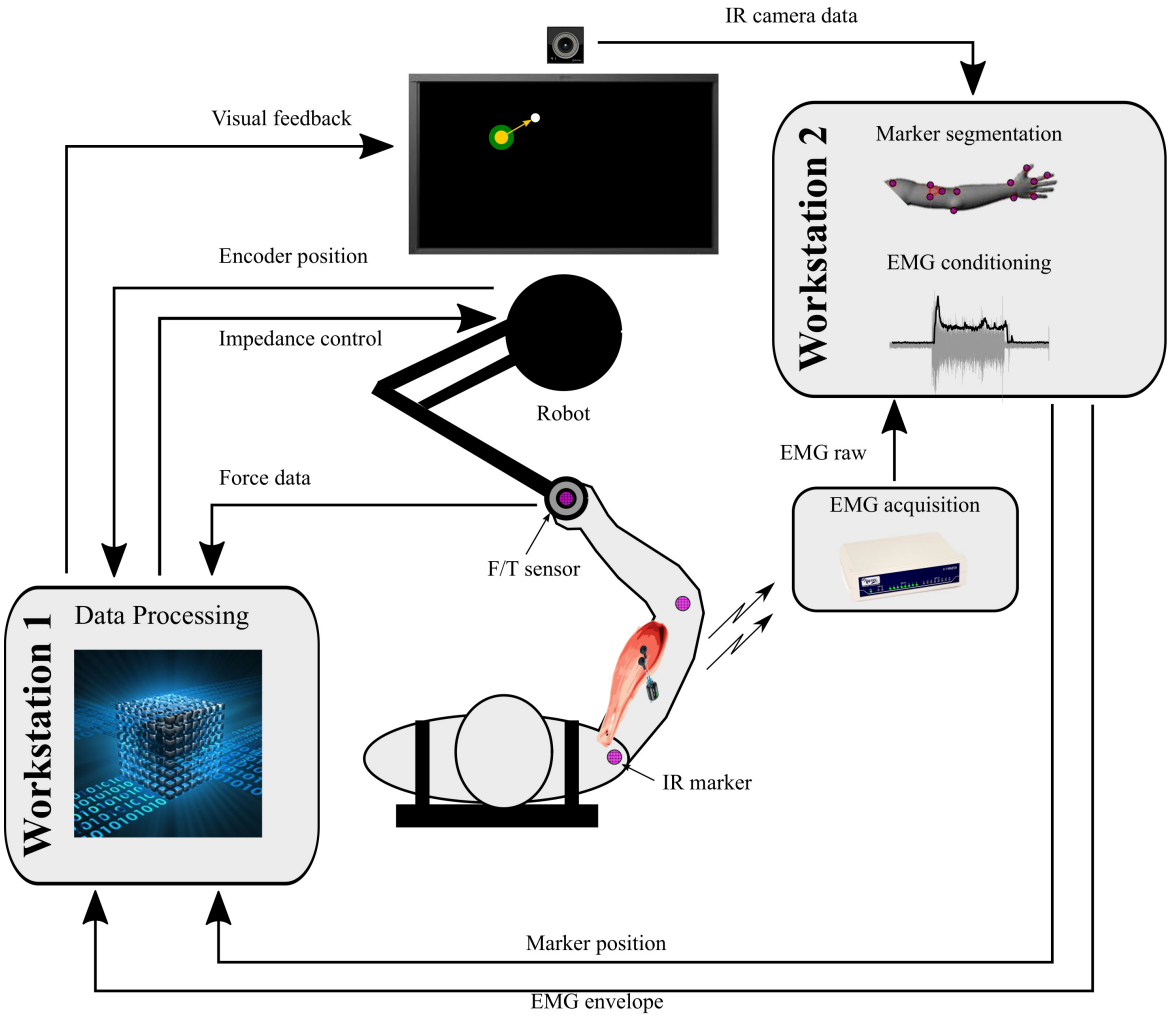

Figure 3.1 *Experimental apparatus of the proportional myoprocessor calibration.*

3.2.2 Task and experimental procedure

The task alternates reaching movements between seven targets, $P_1, \ldots, P_7$ (Flanagan and Rao, 1995) evenly distributed within the robot workspace – see Fig. 3.2, (a) – and isometric force steps in twelve directions, while the hand is centered in each of the P_i targets. Once the spatial target is reached, the robot generates a position-dependent force (stiffness: 8 kN/m) directed toward the target. Subjects are instructed to push against the force field to generate quasi-isometric force steps (amplitude: 25 N) in twelve directions. The target force is displayed as a white circle. The current force generated by the subject is depicted as an arrow; see Fig. 3.2 (b). Once the target force is reached, the target changes its color from white to red, and the subjects must hold the force until the target circle disappears (after 3 s). At this point, the subjects return back to the start position and must relax for 3 s, until a new

force target appears. The whole sequence (movement and force generation) was repeated a total of 5 times. A total of four subjects (2 M + 2 F, age 24 ± 1) participated in this pilot study, all right-handed and with no previous history of neurological disorders; see Table 3.1 for the demographic data.

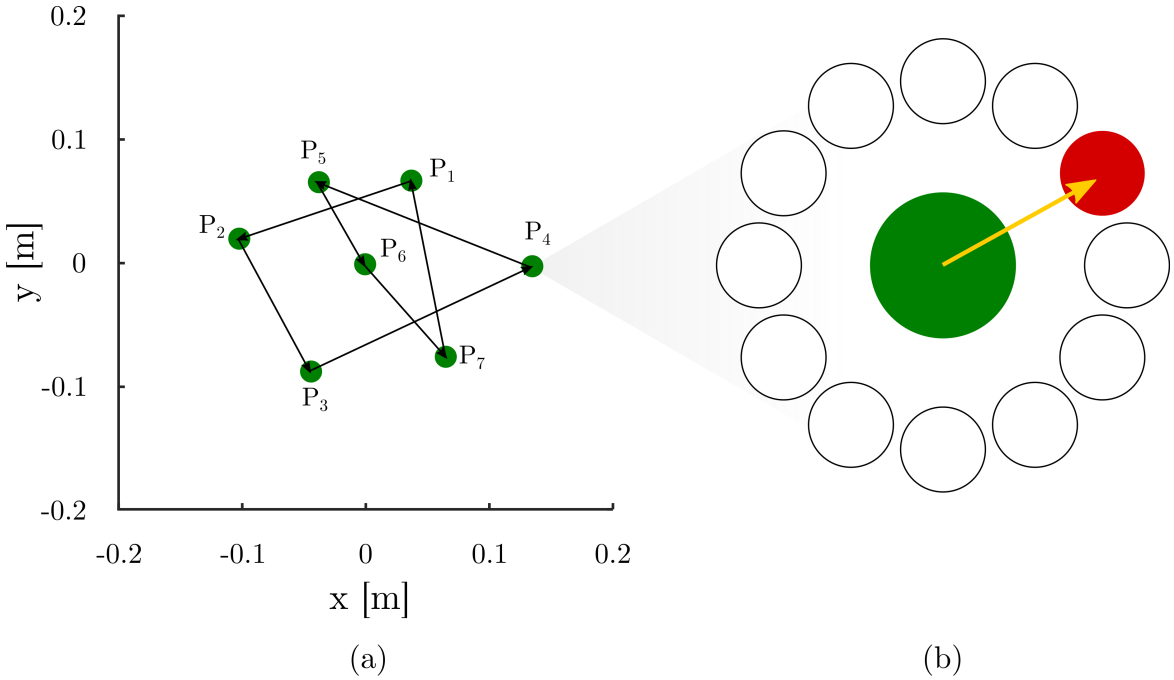

Figure 3.2 *Task scheme of the proportional myoprocessor calibration*. Panel (a) shows the target position in the workspace and the movements toward the targets (black arrows). Panel (b) shows the isometric force step on a single target.

Table 3.1 Subjects demographic data

Subject	Gender	Age	Height [m]	Weight [kg]
S1	F	23	1.70	60
S2	M	25	1.80	75
S3	M	24	1.85	85
S4	F	24	1.60	50

3.3 Data analysis and model identification

Computer PC2 recorded the raw EMG signals from the seven muscles (sampling rate: 1000 Hz). The recorded muscle activity of the major pectoralis was contaminated by the cardiac activity. Using the recorded ECG signal, I removed this artifact by using a cross-correlation

method (Hof, 2009). These signals were online rectified and low-pass filtered with a 100-th order FIR filter (cut-off frequency: 6 Hz). The resulting EMG envelopes were sent to PC1 via a UDP connection – see Fig. 3.1. The same computer also acquired the IR camera frames (sampling rate: 100 Hz) and detected the position of the three markers in camera coordinates. The camera was previously calibrated by comparing the trajectories of the 'robot' marker with the end effector trajectories estimated through the robot encoders. I used the Direct Linear Transform to translate these measures into Cartesian coordinates in the robot coordinate frame. The following signals: (i) envelope of EMG activity, $u(t)$; (ii) endpoint trajectory, $x(t)$; (iii) forces $F(t)$ against the robot handle were sampled at 100 Hz and saved for further analysis. Although the set-up allows for real-time estimation of the joint angles $q_S(t)$ and $q_E(t)$, from the estimated marker positions, in these initial experiments all processing was performed off-line. The camera measurements were used to estimate the skeletal geometry (L_U and L_F). Using these parameters, through inverse kinematics we then derived off-line the joint angles for each time step from the endpoint trajectory. This is less accurate than estimating the joint angles directly from the camera measurements, but does not require to process the latter in real-time. To estimate the muscle parameters, we focused on the isometric portion of the experiment, which allows to identify the spatial patterns of activation of the individual muscles (de Rugy et al., 2012). The maximum activation, U_{max} was estimated, for each muscle, as the maximum activation over all force directions and arm configurations. The remaining parameters include muscle geometry parameters and peak muscle force. In the first variant of the polynomial model, the normative ones, peak muscle forces are the only parameters. In the constant moment arms and the second variant of the polynomial, the fitted ones, peak muscle force always appear multiplied by the muscle geometry coefficients so I can only estimate their product. By defying $B(q) = J_M(q)^T \cdot A$, in all three models B is a function of the parameters set p, i.e. $B = B(q, p)$. The estimation procedure is a quadratic optimisation problem:

$$\begin{cases} \min_p \sum_{t=1}^{T} \left[F_H(t) - J(q(t))^{-T} B(q(t), p) \cdot u(t)\right]^2 + \mu \; p^T \cdot p \\ B_{ij}(q, p) \cdot b_{ij} > 0 \;\; i = 1 \ldots 2, j = 1 \ldots M \end{cases} \tag{3.10}$$

where F_H is the endpoint force exerted on the robot handle (equal and opposite to the force generated by the robot handle). In other words, optimal model parameters that minimise the mean square error between actual and predicted endpoint force. The additional constraints reflect muscle geometry, in the sense that irrespective of the parameters the moment arm of a given muscle with respect to a joint cannot change its sign. We set $b_{ij} = 1$ if muscle j is an extensor for joint i, $b_{ij} = -1$ otherwise. In the normative polynomial model, the constraint reduces to $x_j = F_{max}^{MTj} > 0$ (muscle forces can only be positive). The second part of the cost function penalize solutions in which antagonist muscles exert greater forces.

3.3.1 Model Evaluation

To quantify fitting performance, I used an extended version of the coefficient of determination, r^2, which measures similarity between vector quantities (Crosby et al., 1993). The coefficient r^2 is defined in terms of the cross-correlation matrices between the actual (F_H) and predicted (F_H^{MT}) endpoint force vectors. If I define $\Sigma_{xy} = \mathrm{cov}(x,y)$, where x and y are either F or F_H^{MT}, I have:

$$r^2 = \frac{1}{2}\mathrm{Tr}(\Sigma^{-1}_{F_H F_H}\Sigma_{F_H F_H^{MT}}\Sigma^{-1}_{F_H^{MT} F_H^{MT}}\Sigma_{F_H F_H^{MT}}) \tag{3.11}$$

As in its scalar counterpart, $r^2 = 1$ corresponds to exact fitting, whereas $r^2 = 0$ denotes no correlation between measure and prediction. For each subject, I calculated r^2 separately for each trial, by considering all force trajectories and arm configurations. I then averaged these values over trials. Reconstruction performance alone is not enough to assess the model differences in predicting muscle forces. When applied to scalar data, r^2 measures similarity irrespective of scale. Similarly, when applied to vector quantities, r^2 measures similarity irrespective of vector magnitude and rotation. To account for these, I calculated the matrix regression coefficient A so that $F_H \approx A \cdot F_H^{MT}$, calculated as $A = \Sigma_{F_H F_H^{MT}} \cdot \Sigma^{-1}_{F_H^{MT} F_H^{MT}}$. I then factorized $A = \Lambda R$ where Λ is a diagonal (scale) matrix and R is an orthogonal (rotation) matrix. I finally took rotation $= \tan^{-1}(A_{21}/A_{22})$ and scale $= \mathrm{sign}(A_{11})\sqrt{A_{11}^2 + A_{12}^2}$ as measures of rotation and scale of F_H^{MT} with respect to F_H. Exact fitting not only has $r^2 = 1$ but also rotation$= 0$ and scale $= 1$.

3.4 Results

In the following pages I reported the results obtained by the calibration of the proportional myoprocessor module. This results were also published in the ICORR 2017 proceedings (Lotti and Sanguineti, 2017).

3.4.1 Muscle parameters estimation

The results of the analysis are reported in Fig. 3.3, in a typical subject, for all seven joint configurations. For each muscle, the polar plots depict the spatial selectivity of muscle activation. The columns of the matrix $P(q) = J(q)^{-T}B(q)$ denote, for each muscle, its direction of action or 'pulling vector' (de Rugy et al., 2012) – displayed as an arrow in the figure. The contribution of each muscle to the endpoint force in a given direction is calculated by multiplying the pulling vector by the normalised muscle activation.

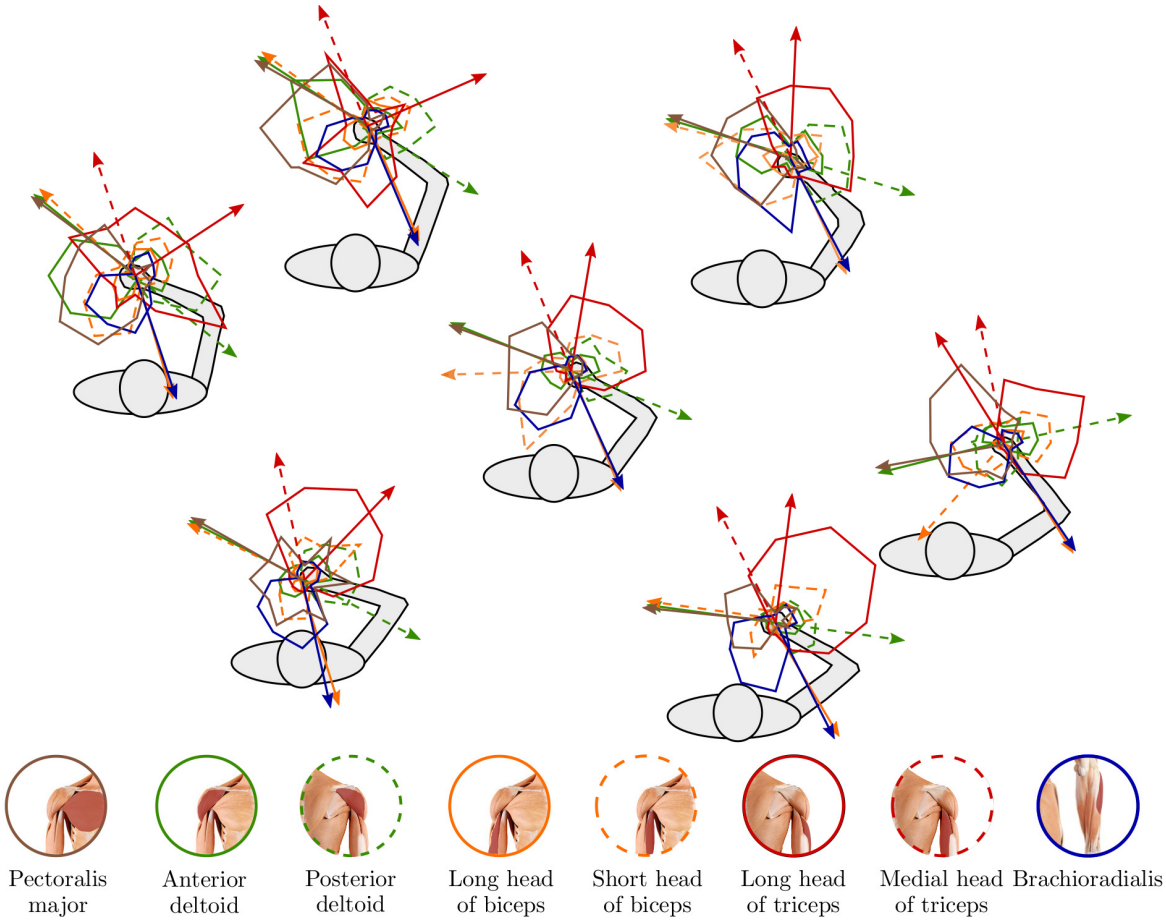

Figure 3.3 *Spatial selectivity of activation and directions of action of the arm muscles*, for a typical subject (S3). For each muscle, the polar plots depict the direction dependence of muscle activation. The arrows denote the muscles' directions of action or 'pulling vectors' (de Rugy et al., 2012).

3.4.2 Isometric force prediction

Table 3.2 summarizes, for each subject, the reconstruction performance (r^2, rotation and scale) obtained by the different muscle geometry models. The first model is the constant moment arms model, the second one is the normative polynomial model and the last one the polynomial model with the coefficients calibrated for each subject (k^*), the fitted polynomial.

Not surprisingly, the more complex model (the fitted polynomial) generally exhibits the best performance. The gain of this model with respect to the constant moment arms model is subject-dependent: accurately modelling muscle geometry provides a gain of $0-6\%$. With respect the normative model of muscle geometry, a personalised model produces a $1-14\%$ increase. Similar differences are observed for scale and rotation. A less obvious finding is

Table 3.2 *Reconstruction performance*, per subject and per muscle geometry model

	j_i = constant			$j_i = \left[k_{S_i} \sum_{j=0}^{5} k_{E_{ji}} q_E^j\right]$			$j_i = \left[k^*_{S_i} \sum_{j=0}^{5} k^*_{E_{ji}} q_E^j\right]$		
Subject	r^2	scale	|rotation| (deg)	r^2	scale	|rotation| (deg)	r^2	scale	|rotation| (deg)
S1	0.73	0.98	8	0.65	0.98	12	0.79	0.98	5
S2	0.73	0.88	24	0.73	0.89	23	0.74	0.89	22
S3	0.72	0.97	14	0.64	0.97	19	0.72	0.97	13
S4	0.63	0.82	31	0.58	0.82	32	0.65	0.85	30
mean±SD	0.70±0.05	0.91±0.08	19±10	0.65±0.07	0.91±0.07	22±8	0.72±0.06	0.92±0.06	17±11

that the constant moment arms model often outperforms the normative polynomial model. Fig. 3.4 compares the actual endpoint force trajectories F_H and their reconstructions F_H^{MT}.

The results suggested that the three muscle geometry models are indeed very different in reconstruction performance. In particular, the fitted polynomial model clearly outperforms the other models, specially in specific force directions.

3.5 Discussion

Adaptability to different subjects was an essential requirement of this modelling effort. The results suggest that accounting for muscle geometry may be important to accurately predict muscle forces from EMG and movement data. As shown in Table 3.2, I found that a more accurate model of muscle geometry significantly improves force reconstruction. The fitted polynomial model was the most adaptable to different anatomical structures because of its parametric model of muscle geometry k^*. This might explain the performance improvement with respect to the normative polynomial model, particularly in the two female subjects (S1 and S4). A less obvious finding is that in spite of its simplicity, the constant moment arms model outperformed the normative polynomial model (r^2, scale and rotation). This may be due to the fact that the muscle geometry parameters in the normative polynomial were fixed: they were estimated by Pigeon (Pigeon et al., 1996) through cadaver anatomical data. This suggests that normative polynomial was good for subjects which reflect this 'average'. In contrast, the parameters of the constant moment arms model were estimated separately for each subject. However, the constant moment arms model did not consider nonlinear changes of muscle length as the arm configuration changes, which might explain why it was outperformed by the fitted polynomial model. I also found that the muscle geometry parameters can be reliably estimated from combined movement, force and EMG data. The reconstruction problem defined by Eq. 3.10 used muscle activations to weight the contributions of the different muscles. If muscles acting on the same joint have similar spatial patterns on muscle activity, the reconstruction problem may become ill-posed, thus allowing

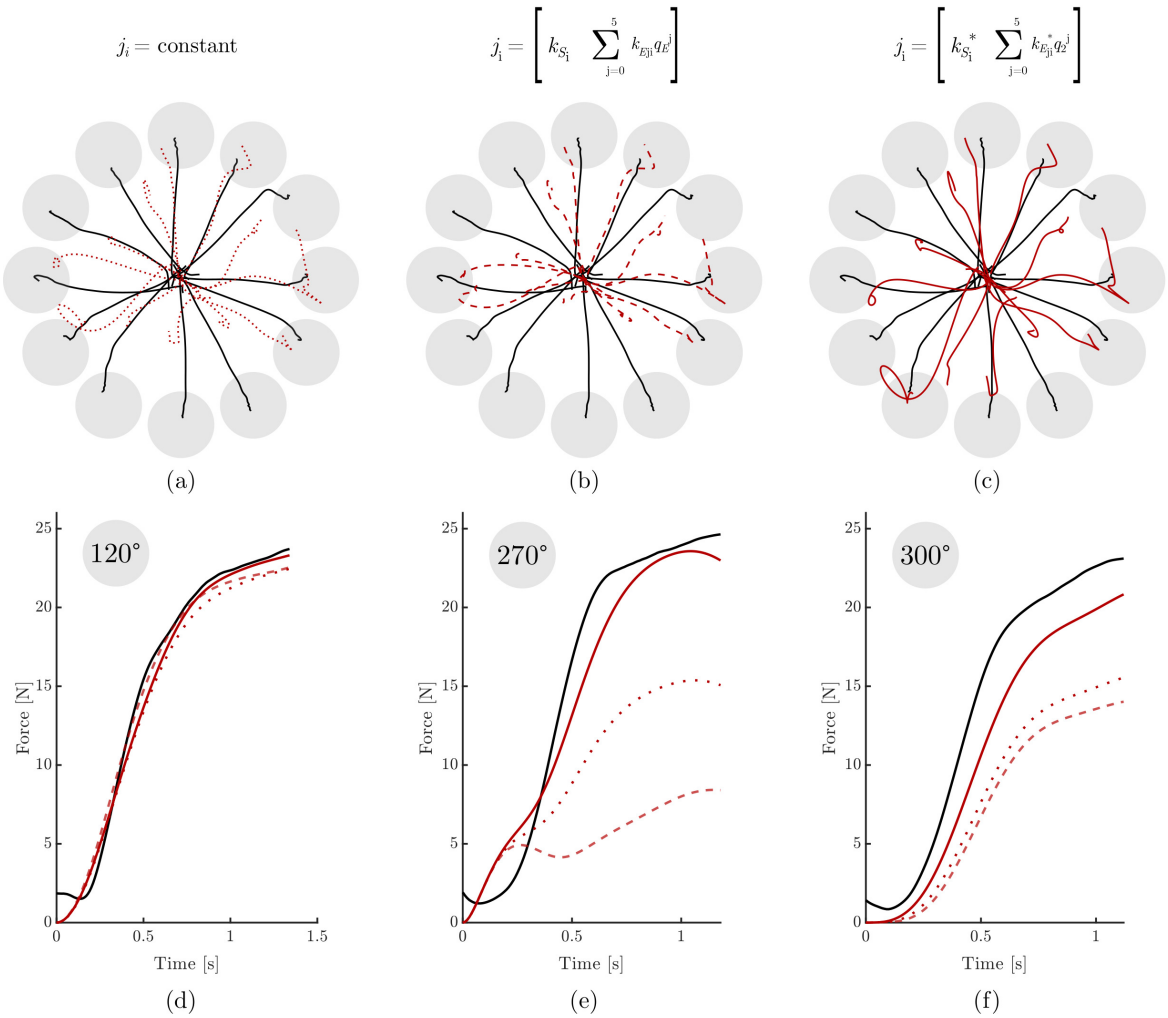

Figure 3.4 *Actual and reconstructed forces using different models of muscle geometry*. Data came from subject S1 and configuration P_6. Panel (a) represents the constant moment arms, panel (b) the normative polynomial model and panel (c) the fitted polynomial model. Red line is the reconstructed force F_H^{MT} and the black ones the measured force F_H. All repetitions for each force direction averaged together. Panels (d), (e) and (f) show the time course of the endpoint forces module in three different target force reaching: for 120°, 270° and 300°. The black line is the measured force and the red lines the force reconstructed by using the three models. The label convention is the same used in panels (a), (b) and (c).

for multiple solutions. This is the case, for instance, when muscles co-contract. Cross-talk is another possible source of inaccurate reconstruction. Because of cross-talk, nearby muscles may turn out to have similar activations, which prevents the correct reconstruction of their respective geometry parameters. This problem may seriously affect the correct assessment of the activity of short head of biceps and the triceps. These problems may be mitigated by allowing during the experiment time intervals to relax muscle activation and by more accurate electrode placement. A penalty term was added to the cost function of Eq. 3.10 to penalise for larger force magnitudes (de Rugy et al., 2012).

Chapter 4

Hill-based myoprocessor module: preliminary version [1]

A proportional myoloectric control approach (Lotti and Sanguineti, 2017) can reliably estimate the net joint torque in isometric condition. However, it cannot model enough the whole muscle-tendon dynamics during movements. A simple linear mapping between the EMG activity and the muscle-tendon force cannot capture all the aspects related to the dynamics contraction. The introduction of a Hill-based model in the myoprocessor module was necessary to improve the controller performance.

4.1 Myoprocessor module

4.1.1 Muscle model structure

The EMG activity, $U(t)$, was normalized with respect to minimum and maximum activation, calculated over the whole trial:

$$u(t) = \frac{U(t) - U_{min}}{U_{max} - U_{min}} \tag{4.1}$$

I then calculated neural activation, $n(t)$ as the output of a second-order low-pass filter:

$$\tau^2 \ddot{n} + 2\tau\dot{n} + n = u \tag{4.2}$$

[1] *Partial content of this Chapter has been published as* Lotti N. and Sanguineti V. Estimation of muscle torques from EMG and kinematics during planar arm movements. *IEEE International Conference on Biomedical Robotics and Biomechatronics*, 29-29 August 2018, Enschede (NL).

with $\tau = 40$ ms.

The muscle model has the Thelen structure (Thelen et al., 2003), with a contractile element (CE), a parallel element (PE) and a tendon element (TE). As simplifying assumption, I considered the tendon as non-deformable, i.e. with a constant length $L^{TE} = L_0^{TE}$. Under this assumption the model is simply defined as:

$$F^M(n, L^M, \dot{L}^M) = F_{max} \cdot \left[\tilde{F}^{CE}(n, \tilde{L}^{CE}, \dot{\tilde{L}}^{CE}) + \tilde{F}^{PE}(\tilde{L}^{CE}) \right] \tag{4.3}$$

with $\tilde{L}^M = \tilde{L}_0^{TE} + \tilde{L}^{CE}$. I modelled the CE as:

$$\tilde{F}^{CE}(n, \tilde{L}^{CE}, \dot{\tilde{L}}^{CE}) = B^H \frac{n \cdot e^{-\left(\frac{\tilde{L}^{CE}}{\tilde{L}_0^{CE}} - 1\right)^2 / \gamma} + A^H \dot{\tilde{L}}^M}{B^H - \dot{\tilde{L}}^{CE}} \tag{4.4}$$

The PE was set to:

$$\tilde{F}^{PE}(\tilde{L}^M) = \frac{e^{K_{PE}\left(\frac{\tilde{L}^{CE}}{\tilde{L}_0^{CE}} - 1\right)} - 1}{e^{K_{PE}\left(\frac{\tilde{L}_{max}^{CE}}{\tilde{L}_0^{CE}} - 1\right)} - 1} \tag{4.5}$$

I set $\tilde{L}_{max}^{CE} = 1.5 \cdot \tilde{L}_0^{CE}$ (Garner and Pandy, 2003). The behaviour of a given muscle is completely specified by the following parameters: F_{max}, $\tilde{L}_0^{CE}$, γ, A^H, B^H and K_{PE}.

4.1.2 Muscle geometry and force capability

The joint torque τ_m is calculated as

$$\tau_m = J_m(q)^T \cdot F_m \tag{4.6}$$

where $J_m(q)$ (matrix of muscle moment arms) is the Jacobian of the vector of lengths of the muscle-tendon complex, $l_{MT}(q)$, and q is limb configuration (vector of shoulder and elbow angles). I adopted a model of muscle geometry based on cadaver and normative anatomical data (Pigeon et al., 1996), which assumes that muscle lengths have a linear dependence on shoulder angle q_S and a polynomial dependence on elbow angle, q_E (up to 5-th order depending on muscle). Following this approach, the j-th row of $J_m(q)$, corresponding to the j-th muscle, can be expressed as

$$J_m^{(j)^T} = \begin{bmatrix} k_{jS} \\ k_{jE0} + k_{jE1} q_E + k_{jE2} q_E^2 + k_{jE3} q_E^3 + k_{jE4} q_E^4 + k_{jE5} q_E^5 \end{bmatrix} \tag{4.7}$$

In bi-articular muscles (short head of biceps, long head of triceps), the moment arm is described by up to 7 parameters per muscle. In mono-articular muscles, there are either one (shoulder: pectoralis major, anterior deltoid, posterior deltoid) or six parameters (elbow: long head of biceps, medial head of triceps, brachioradialis). This makes a total of $2 \times 7 + 3 \times 6 + 3 = 35$ parameters. An additional geometric parameter, l_{m0}, specifies length of the whole muscle-tendon unit for $q_S = 0$ and $q_E = 0$.

4.2 Model calibration

The experimental apparatus, the experimental protocol and the data analysis followed the same procedure described in Chapter 3.

A total of three subjects (2 M + 1 F, age 25 ± 1) participated in this pilot study, all right-handed and with no previous history of neurological disorders. The research conforms to the ethical standards laid down in the 1964 Declaration of Helsinki that protects research subjects. Each subject signed a consent form that conforms to these guidelines.

4.2.1 Parameters identification

Although the set-up allows for real-time estimation of the joint angles $q_S(t)$ and $q_E(t)$, from the estimated marker positions, in these initial experiments I only focused on the model identification procedure which was performed off-line. The camera measurements were used to estimate the skeletal geometry (L_1 and L_2). Using these parameters, through inverse kinematics I then derived off-line the joint angles for each time step from the endpoint trajectory. This is less accurate than estimating the joint angles directly from the camera measurements, but does not require to process the latter in real-time and is an acceptable approximation for planar arm movement with fixed shoulder.

To estimate the muscle parameters from the movement data I used a two-step procedure.

Muscle geometric and 'static' parameters

I initially focused on the isometric portion of the experiment. For each muscle I estimated the maximum activation, U_{max} as the maximum activation over all force directions and arm configurations. In isometric conditions, the endpoint force, F_h – i.e. the force exerted on the robot handle – reflects the joint moments:

$$\tau_m = J(q)^T F_h \tag{4.8}$$

where $J(q)$ is the Jacobian of the forward kinematics transformation $x = x(q)$, where x is hand position. Given the above assumptions we have:

$$J(q) = \begin{bmatrix} -L_1 \sin q_S - L_2 \sin(q_S + q_E) & -L_2 \sin(q_S + q_E) \\ L_1 \cos q_S + L_2 \cos(q_S + q_E & L_2 \cos(q_S + q_E) \end{bmatrix} \tag{4.9}$$

The estimation procedure is formulated as a quadratic optimization problem:

$$\begin{cases} \min_p \sum_{i=1}^{7} \sum_{d=1}^{12} \sum_{t=1}^{T} \left[\tau_m(t) - J_m(q(t))^T \cdot F_m \right]^2 + \mu \left\| F_{max} \right\|^2 \\ J_m^{ij}(q) \cdot b_{ij} > 0 \;\; i = 1 \ldots 2, j = 1 \ldots M \end{cases} \tag{4.10}$$

where $\tau_m = J(q)^T F_h$ is the isometric joint torque (corresponding to the endpoint force F_h) and F_m is the vector of the predicted muscle forces. Therefore, the cost function minimizes the mean square error between actual and predicted joint torque. The additional constraints reflect the requirement that irrespective of the parameters values, the moment arm of a given muscle with respect to a joint cannot change its sign. We set $b_{ij} = 1$ if muscle j is an extensor for joint i, and $b_{ij} = -1$ otherwise. The second part of the cost function penalizes solutions involving muscle co-contraction.

The vector p includes moment arm geometry, peak muscle force and all the static parameters of the muscle model. Therefore, $p = \left\{ l_{m0}^j, k_{jS}, k_{jE0}, \ldots, k_{jE5}, K^j, F_{max}^j, l_{CE_0}^j, \gamma^j, K_{PE}^j \right\}$, for each muscle $j = 1 \ldots M$. I initialized all the parameters with values found in the literature for both muscle geometry (Pigeon et al., 1996) and contractile properties (Garner and Pandy, 2003). I additionally required that each parameter remained within its physiological range. In the optimization, I used an iterative procedure in which the cost function was minimized with respect to the geometric parameters – by keeping the muscle parameters fixed – and by optimizing the muscle parameters alone, in alternation until convergence.

Muscle dynamic parameters

To estimate the muscle dynamic parameters of the Hill-based model, I only focused on the movement data. During movements the hand force measured by the force sensor, $F_h(t)$ reflects not only joint moments τ_m, but also arm dynamics:

$$I(q)\ddot{q} + C(q, \dot{q}) = \tau_{dyn}(q, \dot{q}, \ddot{q}) = \tau_m - J(q)^T \cdot F_h \tag{4.11}$$

so that $\tau_m = J(q)^T \cdot F_h + \tau_{dyn}$. I used a normative model of arm dynamics, whose parameters were determined from individual subjects' mass and arm geometry (Winter, 2009), in conjunction with measured joint rotations, angular velocities and accelerations to calculate

the inverse dynamics, τ_{dyn} at each time instant. I then minimized the following cost function:

$$\min_{p} \sum_{r=1}^{4} \sum_{i=1}^{7} \sum_{t=1}^{T_{ir}} \left[J(q(t))^T \cdot F_h(t) + \tau_{dyn} - J_m(q(t))^T \cdot F_m \right]^2 \tag{4.12}$$

where $r = 1,\ldots,4$ are the repetitions and $i = 1,\ldots,7$ are the movements. The model parameters here describe, for each muscle, the dependence of CE force on shortening or lengthening speed, i.e. $p = \left\{A^H, B^H_{conc}, B^H_{ecc}\right\}$.

4.3 Results

4.3.1 Joint moments estimation in isometric conditions

An example of the reconstruction of the endpoint isometric force trajectories is displayed in Figure 4.1. For one specific force direction, the Figure also shows the recorded muscle activities and the corresponding joint moments estimates.

The overall reconstruction performance, for all directions and arm configurations, is summarized in Table 4.1. In two subjects (S1 and S3) the reconstruction performance is close or around 80% throughout the whole workspace. A somewhat poorer performance is observed in subject S2.

Table 4.1 Coefficient of determination (r^2), expressed in %, of isometric torque reconstruction performance, per subject and per configuration

	P1		P2		P3		P4		P5		P6		P7		mean±std	
Subject	sh	el	sh	el	sh	el	sh	el	sh	el	sh	el	sh	el	sh	el
S1	81	84	83	83	91	90	90	88	89	76	86	90	81	83	86±4	85±5
S2	71	73	70	78	44	50	69	58	64	55	76	74	83	81	68±11	67±11
S3	89	79	91	75	80	89	53	40	87	85	86	86	61	77	78±14	76±15
mean	80	79	81	79	72	76	71	62	80	72	83	83	75	77	77±4	75±6
std	6	4	8	3	20	19	15	20	11	12	5	7	9	2		

4.3.2 Joint moments estimation during movements

Figure 4.2 shows the recorded EMG activity and the hand speed profiles for three such movements.

For the same movements, Figure 4.3 displays the measured and reconstructed joint moments.

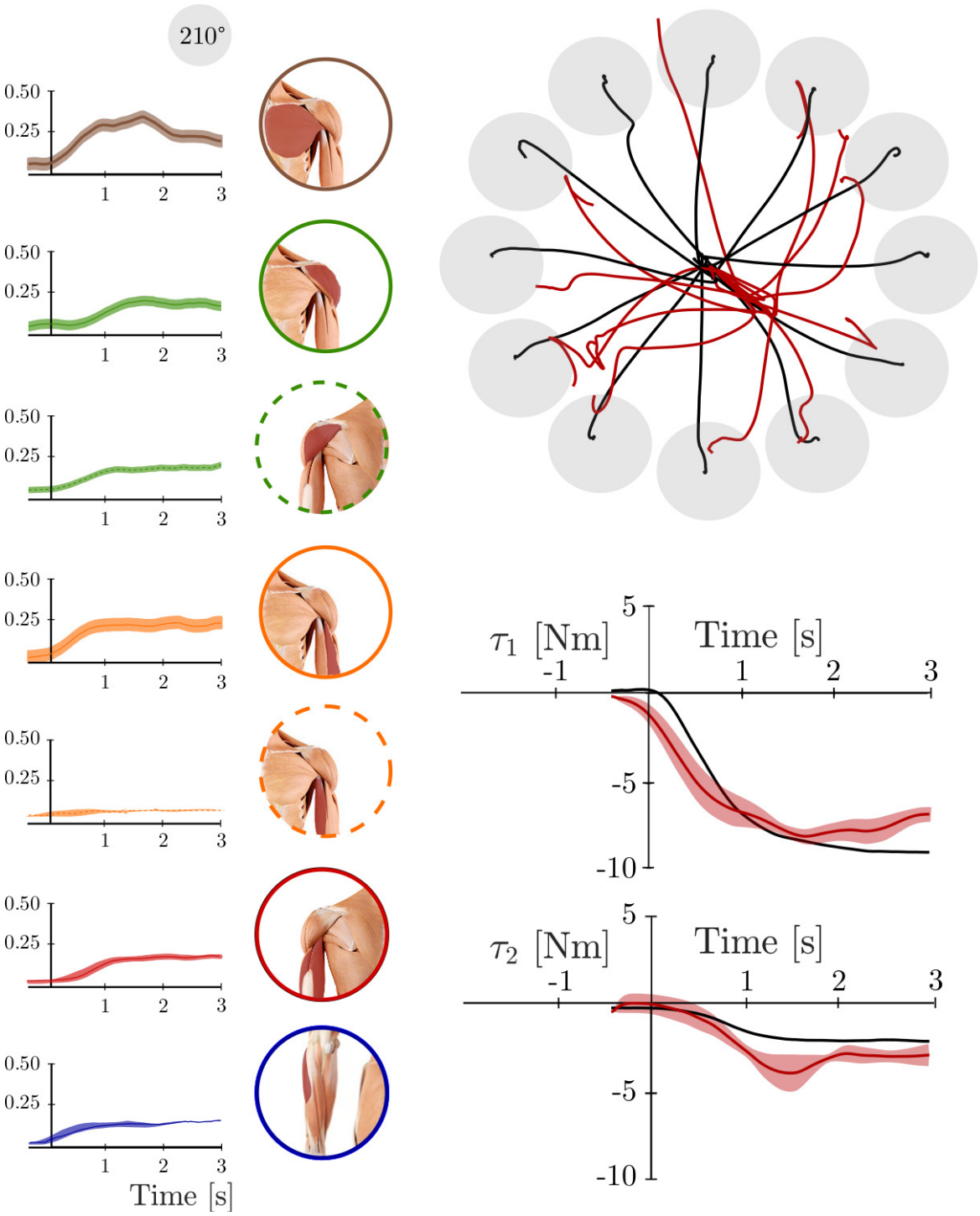

Figure 4.1 *Isometric endpoint force reconstruction.* Top, right: Measured (black) and estimated force trajectories (red) in a typical subject and in a specific configuration (P6). Bottom, right: joint moments (measured and estimated) for the force direction $-150°$. Left: normalized EMG activity $u(t)$ for the same force direction.

Table 4.2 *Coefficient of determination* (r^2), expressed in %, of isometric torque reconstruction, per subject and per configuration

	P1		P2		P3		P4		P5		P6		P7		mean±std	
Subject	sh	el	sh	el	sh	el	sh	el	sh	el	sh	el	sh	el	sh	el
S1	16	11	25	76	80	45	40	23	24	34	39	20	61	33	41±21	35±20
S2	21	25	17	20	15	20	15	14	15	13	10	11	12	18	15±3	17±5
S3	16	10	32	43	56	47	39	36	19	10	15	10	26	37	29±14	28±16
mean	18	15	25	46	50	37	31	24	19	19	21	14	33	29	28±10	26±11
std	2	7	6	23	26	12	12	9	4	11	13	4	21	8		

Table 4.2 summarizes the reconstruction performance for all trajectories and subjects. The reconstruction performance is lower than in isometric conditions. However, some subjects still exhibit a high reconstruction performance at least for some trajectories.

4.4 Discussion and Conclusions

The reconstruction performance exhibited in isometric movements suggests that muscle geometry and muscle activation parameters can be reliably estimated from EMG data.

The reconstruction performance during movements is only acceptable for some subjects and movements. Estimation accuracy is generally better in elbow torques with respect to the shoulder.

This degradation may have multiple causes. The reconstruction problem defined by Eq. 4.10 uses muscle activations to weight the contributions of the different muscles. If muscles acting on the same joint have similar spatial patterns of muscle activity, the reconstruction problem may become ill-posed, thus allowing for multiple solutions. This is the case, for instance, when muscles co-contract. Cross-talk is another possible source of inaccurate reconstruction. Because of cross-talk, nearby muscles may turn out to have similar activations, which prevents the correct reconstruction of their respective geometry parameters. These problems affect both movements and isometric conditions, but may additionally affect the estimation of dynamic parameters, thus affecting to a greater extent the torque predictions during movements.

Poor estimation of shoulder torques during movement may additionally depend on inaccurate modeling of muscle geometry at the shoulder (for which a constant moment arm is assumed), and/or residual movements of the shoulder. Although preliminar, this work is one step forward the implementation of a general myo-processor which is capable of estimating muscle torques in a variety of conditions.

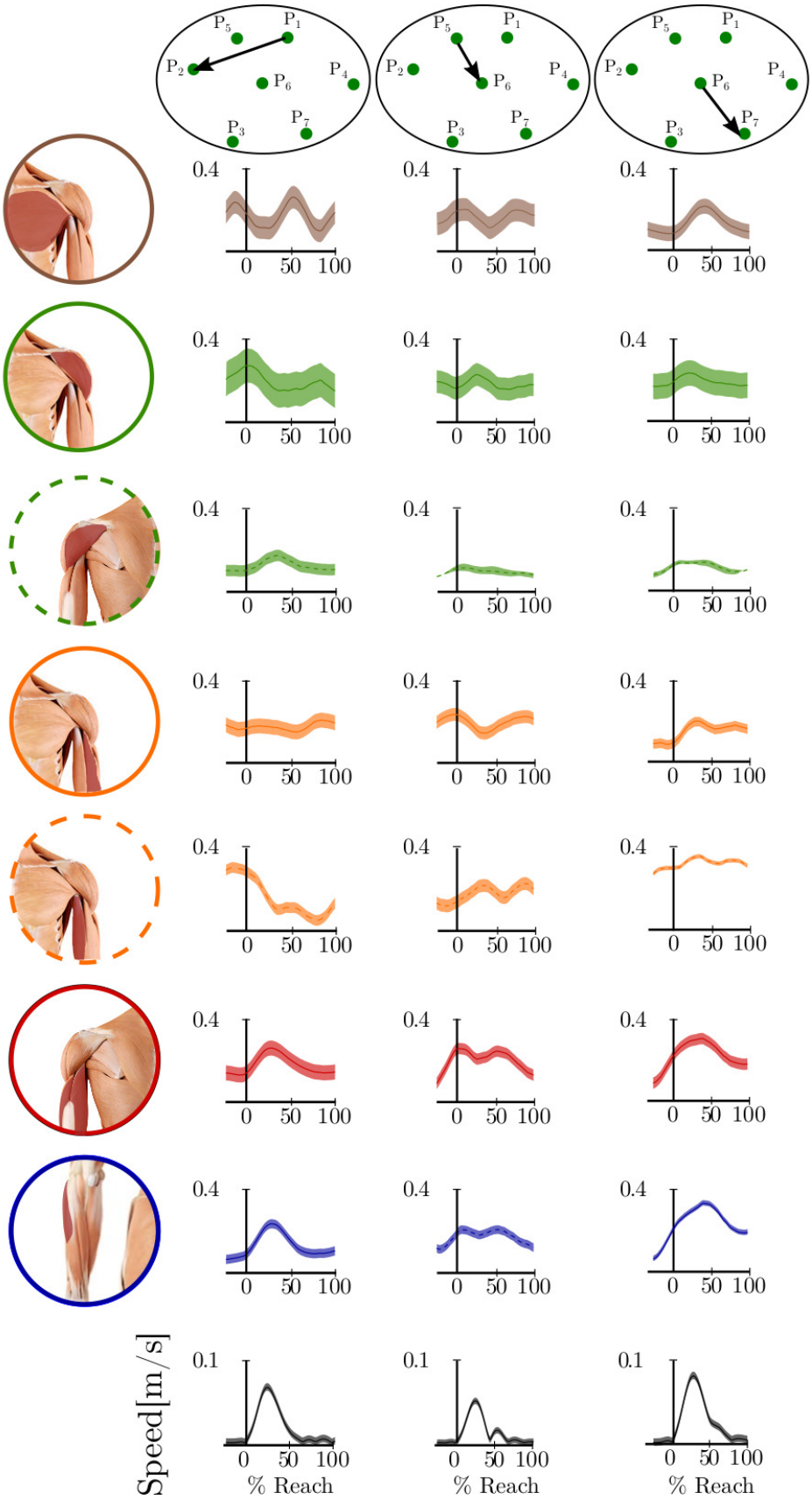

Figure 4.2 *Normalized EMG activity and speed profiles for three specific movements.*

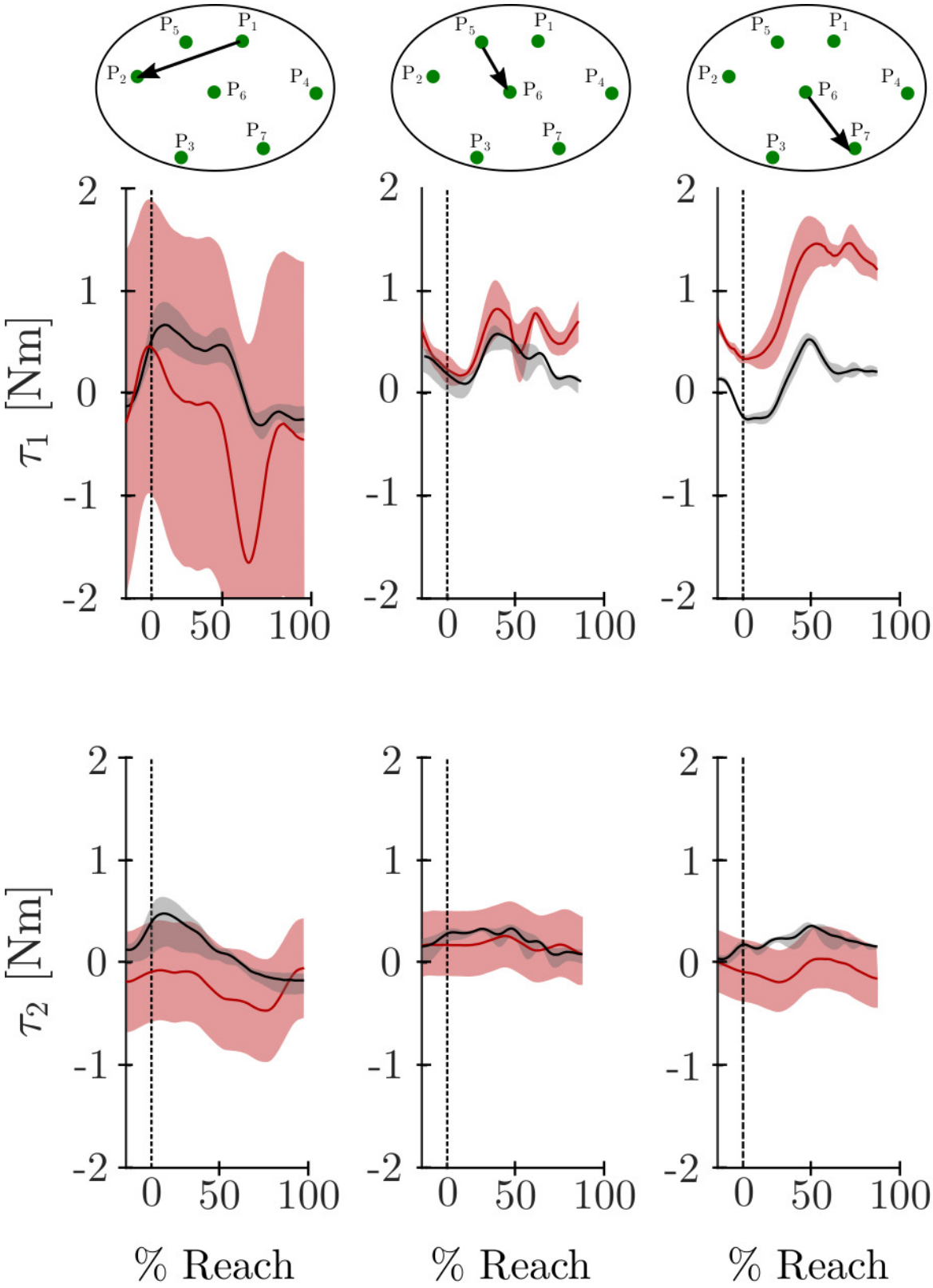

Figure 4.3 *Joint moments reconstruction during movement*. Estimated (black) vs reconstructed (red) - mean ± SE - for a three specific movements, for a typical subject

Chapter 5

Hill-based myoprocessor module: final version

The previous version of the myoprocessor module estimated muscle geometry (i.e. muscle-tendon length and moment arm) by using a polynomial model. This approach was not enough robust to describe the geometry on the overall workspace. During my visiting period at University of Twente, I learned several approaches to improve the myoprocessor module. The most important was related to the muscle geometry estimation

5.1 Muscle geometry estimation toward cubic b-spline

This technique is based on the work of Sartori (Sartori et al., 2012). A cubic spline consisted of a series of third-order polynomials spliced together to preserve continuity of the first and second order derivatives. The points at the which polynomials are spliced together are called nodes. I spliced the range of motion of each joint in n nodes. I sampled the muscle-tendon length L^{MT} of a musculoskeletal model (Holzbaur et al., 2005), previously scaled in order to match subjects' anatomical size. The lengths L^{MT} were interpolated by using the cubic splines. To compute the moment arms $j^M_{q_i}$, I derived L^{MT} respect to the joint.

$$j^M_{q_i} = \frac{\partial L^{MT}}{\partial q_i} \tag{5.1}$$

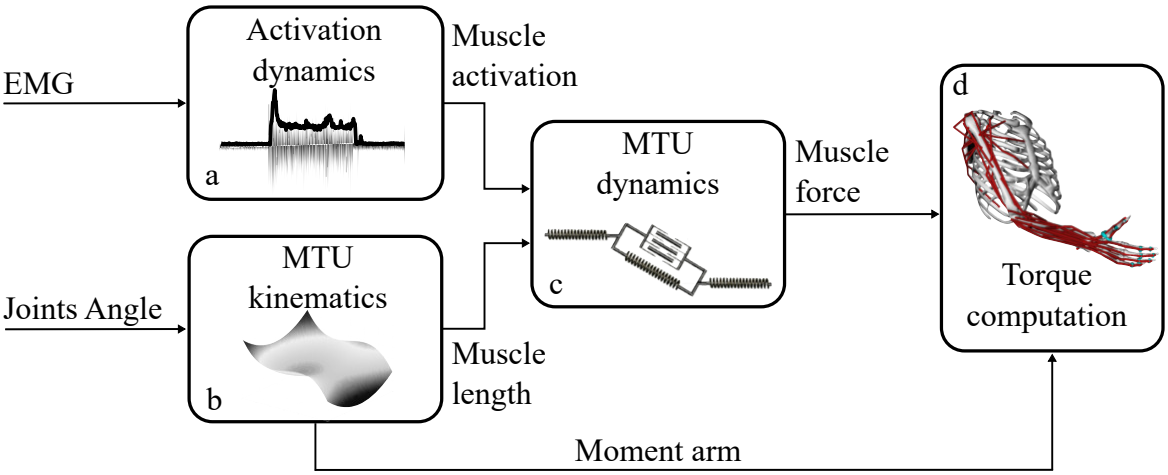

Figure 5.1 *The myoprocessor module scheme.*

5.2 Muscle model structure

The myoprocessor model is composed by four elements, as shown in Fig. 5.1: the *Activation dynamics* block describes the muscle fiber recruitment, the *MTU kinematics* estimates the muscle geometry (e.g. muscle-tendo unit length and moment arm), the *MTU dynamics* block describes how to obtain the muscle forces and the *torque computation* computes the torque at the joints level.

Activation dynamics

In the *Activation dynamics* block the EMG signals are converted into the muscles activation. As the first step, the normalized EMG signal $\text{emg}_j(t)$ for the muscle j is converted into the neural excitation $u_j(t)$ by using a second-order discrete linear model Lloyd and Besier (2003)

$$u_j(t) = \alpha \cdot \text{emg}_j(t-d) + \beta_1 \cdot u(t-1) + \beta_2 \cdot u(t-2) \tag{5.2}$$

where α is the gain coefficient, β_1 and β_2 the recursive coefficients and d the electromechanical delay. To obtain the muscle activation $a_j(t)$ we used the non-linear relationship described in Lloyd and Besier (2003)

$$a_j(t) = \frac{e^{A_j u_j(t)} - 1}{e^{A_j} - 1} \tag{5.3}$$

Muscle-tendon unit kinematics

The *Muscle-tendon unit kinematics* synthesizes the three-dimensional musculoskeletal geometry of the human arm (Holzbaur et al., 2005) into a set of multidimensional cubic B-splines (Sartori et al., 2012).

Muscle-tendon unit dynamics

This unit estimates the muscle force starting from the *Activation dynamics* and *MTU kinematics* outputs. The force $F_j^{MT}(t)$ produced by the j-muscle is obtained by the equation

$$F_j^{MT}(t) = F_j^{max}[a_j(t)f_l(t)f_v(t) + f_p(t)] \cdot \cos\phi_j(t) \tag{5.4}$$

where F_j^{max} is the maximum isometric force, $a_j(t)$ the muscle activation, f_l, f_v and f_p are respectively the force-length relationship, the force-velocity relationship and the parallel passive elastic muscle force. Finally, ϕ_j is the pennation angle. The force-length, force-velocity relationship and the passive elastic muscle force have the Thelen structure (Thelen, 2003): f_l describes the force produced by the muscle in isometric condition as

$$f_l(t) = e^{-\frac{(l^M(t)-1)^2}{\gamma}} \tag{5.5}$$

This relationship depends by the normalized muscle length $l^M(t)$. The shape factor γ is the same for each muscle. The force velocity relationship models the muscle force during eccentric and concentric movements

$$f_v(t) = \begin{cases} \frac{v(t)+1}{1+1/A_f}, & v(t) < -1 \\ \frac{v(t)+1}{1-v(t)/A_f}, & -1 \le v(t) < 0 \\ \frac{(2+2/A_f)vf_{len}^M+f_{len}^M-1}{(2+2/A_f)v+f_{len}^M-1}, & 0 \le v(t) < \frac{10(f_{len}^M-1)(0.95f_{len}^M-1)}{(1+1/A_f)f_{len}^M} \\ \frac{f_{len}^M}{20(f_{len}^M-1)}\left(\frac{(1+1/A_f)vf_{len}^M}{10(f_{len}^M-1)} + 18.05f_{len}^M - 18\right), & v(t) \ge \frac{10(f_{len}^M-1)(0.95f_{len}^M-1)}{(1+1/A_f)f_{len}^M} \end{cases} \tag{5.6}$$

where A_f is a shape factor and f_{len}^M the maximum normalized muscle force achievable when the fiber is lengthening. The last relationship f_p computes the passive force in the muscle dues to the elasticity of the tissue that is in parallel with the contractile element. Passive forces are very small when the muscle fibers are shorter than their optimal fiber lengths, L_0^M, and rise greatly thereafter

$$f_p(t) = \begin{cases} 0, & l^M \leq 1 \\ \frac{e^{\frac{k_p}{\varepsilon} l^M(t)} - 1}{e_p^k - 1}, & l^M > 1 \end{cases} \tag{5.7}$$

The pennation angle $\phi_j(t)$ for the j-muscle depends by the muscle length $L^M(t)$, by the optimal fiber length L_0^M and by the pennation angle of the muscle fibers at the optimal fiber length ϕ_0

$$\phi_j(t) = \frac{L_0^M \cdot \sin(\phi_0)}{L^M(t)} \tag{5.8}$$

5.3 Myoprocessor calibration

The myoprocessor module is subject-specific. The calibration consists of three procedures: (i) EMG normalization, (ii) muscle geometry estimation, (iii) parameters optimization. The EMG are normalized trough a maximum voluntary contraction trial (MVC) in which subjects performed a series of task in order to achieve the maximum contraction for each muscle included in the model. The muscle geometry estimation linearly scales a generic musculoskeletal model (Holzbaur et al., 2005) to match each individual's arm anthropometry by using the open-source software OpenSim. From the scaled model I extract the musculotendon lengths and moment arms through the multidimensional spline techniques (see Chapter 2). The parameters optimization calibrates several parameters of the myoprocessor module by using the kinematic data, EMG, and Force signals recorded during a calibration task related to the application (see Chapter 7, 8). By using the simulated annealing algorithm (Das and Chakrabarti, 2005), the minimized function is

$$\sum_{i=1}^{nDoFs} \sum_{t=1}^{N} (\tau_i^{ref}(t) - \tau_i^M(t))^2 \tag{5.9}$$

where $nDoFs$ are the degrees of fredoom of the model, τ^{ref} is the reference torque and τ^M the torque estimated by the myoprocessor model. The parameters involved in the optimization function are the optimal fiber length, the tendon slack length and the maximum isometric force in the MTU dynamics block (Fig. 5.1c) and the filtering coefficients and the non-linear coefficient in the activation dynamics block (Fig. 5.1a).

Chapter 6

Real-time control

The ultimate challenge in the development of a myoprocessor is to convert the musculoskeletal model into a real-time controller. The control algorithm could be different depending on the hardware target. The control techniques can be grouped in two main different fields: compliant and stiff control (Calanca et al., 2015). Traditional robotic devices used the stiff control in order to be as stiff as possible, by increasing position/velocity control accuracy and bandwidth. However, the high stiffness produced high force modification for small displacement errors by causing instability and unsafe interaction. Compliance controller try to fix these issues by shaping the mechanical impedance of the robotic system, i.e. the dynamical relation between robot position or velocity and external forces (Hogan, 1985). These changes allow to safely interact with the unknown environment because, instead of controlling either a position or a force, It possible to control the power transferred to the environment. A common term that highlights the aim to change in real-time the rigidity of the robot is *virtual stiffness control*.

The virtual stiffness can be controlled by using impedance or admittance control over stiff or soft joints. For example, let

$$f_e = g(x, \dot{x}, \ddot{x}) \tag{6.1}$$

be the ordinary differential equation modeling of a single degree of freedom mechanical system, where f_e is the sum of external or environmental forces and x is a Lagrangian coordinate. At given position x_0 the stiffness can be defined as

$$k = \frac{\partial g(x, \dot{x}, \ddot{x})}{\partial x}\Big|_{x=x_0} \tag{6.2}$$

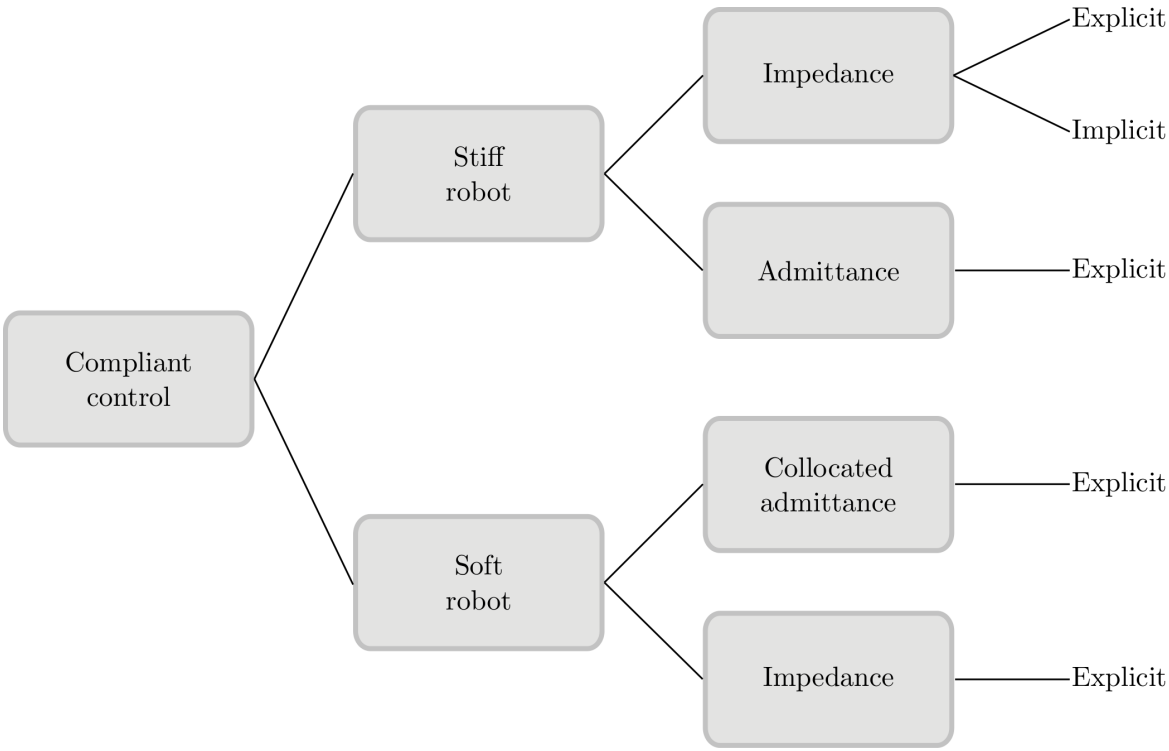

Figure 6.1 *Compliant control*. Compliant control for soft and stiff robots scheme (Calanca et al., 2015). Explicit and implicit refer, respectively, to the need or not of a sensor to measure the interaction force between the robot and the environment. Image adapted from (Calanca et al., 2015).

Mechanical compliance is the reciprocal of stiffness, $c = k^{-1}$. It refers to the ability to exhibit displacement if a force is applied. While stiffness and compliance refer to the static displacement/force relation, impedance, and admittance describe the dynamic relations between force and velocity. In the literature, alternative definitions of impedance and admittance are used by considering the relation between force and velocity instead of position, to account for power quantities. Using Laplace notation, impedance and admittance can be computed as

$$I(s) = \frac{F_e(s)}{JX(s)} \qquad A(s) = \frac{JX(s)}{F_e(s)} = I(s)^{-1} \tag{6.3}$$

where J is the rotor inertia, $Fe(s)$ and $X(s)$ are the Laplace transform of $f_e(t)$ and $x(t)$, respectively.

The control of a task in an environment having kinematic and/or dynamic constraints is generically termed interaction control. The main distinction is between active interaction control and passive interaction control. In active interaction, the compliance is entirely due to

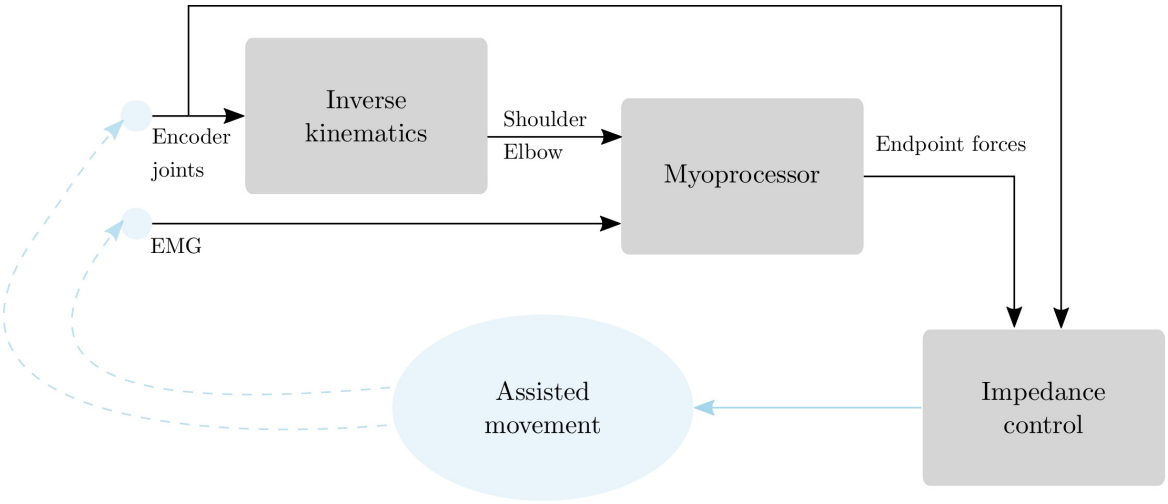

Figure 6.2 *Impedance scheme planar robot manipulandum.*

control, while in passive interaction, it is entirely due to mechanics. Active control is divided in direct and indirect subcategories. The direct force control category includes algorithms that control separately the force and the position subspaces, called hybrid position–force control (Mason, 1981), (Raibert et al., 1981). Fig. 6.1 summarises all the control technique in robotics. Both soft and stiff control require a fast inner loop and an outer loop to shape the impedance or admittance. Admittance control on stiff joint cannot display a low impedance whereas impedance control cannot display a high impedance.

Figure 6.2 shows an example of a myoprocessor module combined with an impedance stiff control: the controller, implemented on a planar robot manipulandum, takes as inputs the value of the motor encoder and the endpoint forces computed by the myoprocessor.

The relation between the current $i(t)$ that controls the motors and the endpoint forces $F^H(t)$ is

$$i(t) = k \cdot J(q)^T \cdot F^H(t) \tag{6.4}$$

where k is the vector that contains the relationship between the current and the motors torque and $J(q)$ the Jacobian matrix that depends by the encoders value.

An opposite example is to apply the myoprocessor module to a soft wearable exosuit, that presents soft joint. The admittance controller (Fig. 6.3) compares the difference between the muscle torque τ_m and the interaction torque τ_i.

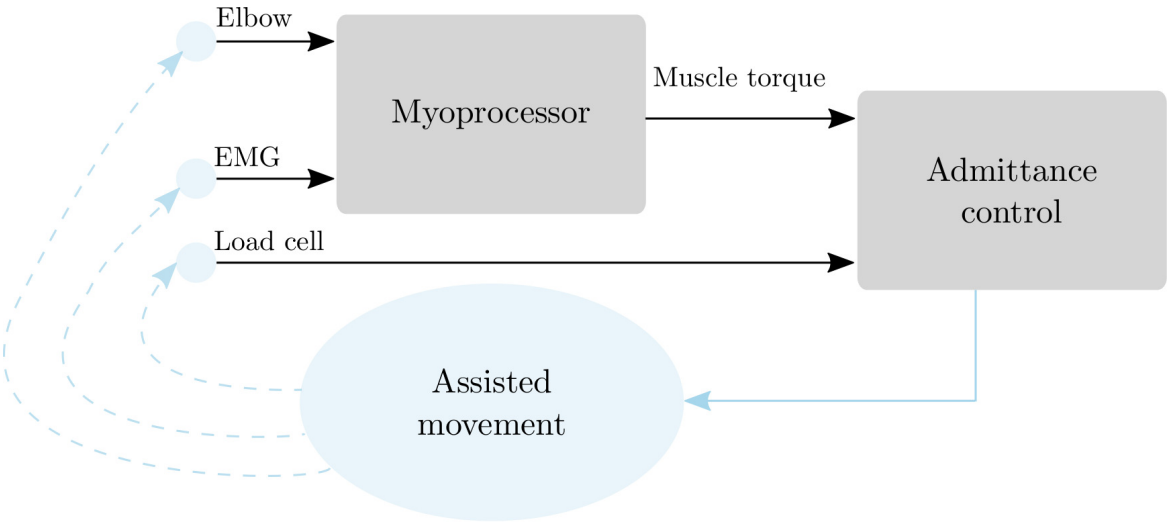

Figure 6.3 *Admittance scheme exosuit.*

From the resultant torque τ_r is possible to obtain the velocity that controlled the motor through a PID-like admittance

$$Y(s) = \frac{\omega_r}{\tau_r} = P + \frac{I}{s} + Ds \tag{6.5}$$

where the P, I and D gains shapes the dynamic response of the exosuit in order to follow the target τ_m from the myoprocessor. The velocity can be converted into the current $i(t)$ through a gain value k.

Part III

Myoprocessor applications

Chapter 7

Adaptive model-based myoelectric control for a soft wearable arm exosuit[1]

7.1 Introduction

The quest for co-existence between humans and machines has pushed scientific boundaries beyond industrial automation, towards the area of wearable robotics. With regards to motor rehabilitation and augmentation, a wealth of wearable robots have been designed for providing movement assistance. In this context, the aim is that of compensating for reduced or missing voluntary activity via controlled forces that support task-based motor activities. Yet, technological limitations hamper the adoption of wearable robots and their widespread acceptance by final users: limitations in ergonomics, motor intention prediction and in control robustness represent major open challenges.

Existing wearable robots (i.e. active orthoses or exoskeletons) interact with their users with little knowledge of the effects induced to the musculoskeletal system. It is currently unknown how the human body responds to different HMI types and how wearable robots should operate to best enhance movements (Sartori et al., 2016). In this context, HMIs for active orthoses and exoskeletons have been developed that superpose pre-defined trajectories to the user's joint motions in order to provide the level of assistance necessary to complete selected functional movements (Lo and Xie, 2012). HMIs using model-free machine learning approaches have also been proposed. These include pattern recognition or regression to map electromyograms (EMGs) into joint kinematics. However, one joint rotation can be generated

[1] *The whole content of this Chapter has been published as* Lotti, N., Xiloyannis, M., Durandau, G., Galofaro, E., Sanguineti, V., Masia, L., and Sartori,M. Adaptive model-based myoelectric control for a soft wearable arm exosuit: A new generation of wearable robot control. *IEEE Robotics & Automation Magazine, 2020.*

via different EMG patterns. Therefore, mappings learned in one condition (i.e. low loads) may not generalize to novel conditions (i.e. high loads), leading to lack of control robustness (Sartori et al., 2018). An alternative approach is that of neuromusculoskeletal modeling, which explicitly characterizes each intermediate transformation between EMG-onset and joint torque production by simulating the interplay between the nervous, the muscular, and the skeletal systems. We will refer to this as a myoprocessor. Unlike a model-free machine learning approach, a myoprocessor maps EMGs into forces that belong to the solution space of the human musculoskeletal system (Cavallaro et al., 2006). Therefore, decoded forces are always within physiological bounds, potentially enabling robust robot control across a broad range of conditions (Durandau et al., 2018).

Design of powered orthoses has been long based on rigid exoskeletal technologies. This has the drawback of restricting body mobility, inducing misalignment with the user's joint (Schiele et al., 2006) as well as leading to sub-optimal ergonomics due to the device excessive weight and size (Frisoli et al., 2005). The introduction of soft robotic exosuits, employing flexible materials for transmitting forces to the human body, has provided the possibility of addressing limitations of rigid hardware (Asbeck et al., 2014). Soft exosuits have the potential to effectively operate as an external layer superposed to biological muscles to support human joint mechanics.

However, despite potential benefits, exosuits still present limited control reliability (Ding et al., 2017) due to their highly non linear behaviour, lower tracking accuracy, reduced magnitude of assistance and control robustness when compared to rigid exoskeletons (Park and Cho, 2017). As a result, there is currently no effective framework for controlling soft wearable robots as a function of human motor intention (Anam and Al-Jumaily, 2012).

We have developed a new framework that combines, for the first time, a model-based human machine interface (HMI) with a soft wearable arm exosuit, ultimately for addressing key limits in current HMIs and wearable robotics. This work assessed whether a myoprocessor based on an EMG-driven musculoskeletal model could be established and personalized to different individuals. We assessed the myoprocessor accuracy in decoding elbow joint torques from EMGs and translating decoded torques into exosuit control commands across a repertoire of dynamic joint rotations and load lifting tasks. To the best of our knowledge, this is the first time that a subject-specific EMG-driven musculoskeletal model is synthetized into an HMI for the online control of an upper limb exosuit. Interfacing real-time myoprocessors with soft wearable robotics may lead to a new paradigm for achieving exosuit control robustness as well as symbiotic human-exosuit interaction.

Figure 7.1 *Exosuit device.* The exosuit for assistance of the elbow joint is comprised of three fabric straps: one around the forearm (distal anchor point), one around the arm (proximal anchor point) and a shoulder harness, connected to the arm strap via adjustable webbing bands. Buckles, velcro straps and a Boa lacing system allow to tighten the suit. A pair of Bowden cables is attached to the front and the back of the arm strap and transmits power from an actuation unit to the anchor points. The assistance is provided by recovering the front cable during elbow flexion. During elbow extension the motor releases the cable.

7.2 Methods

7.2.1 Exosuit design and control hardware

A cable-driven elbow exosuit (Xiloyannis et al., 2019) (Fig. 7.1) powered by a brushless electric motor (EC-i 40-70W, Maxon, Sachseln, Switzerland) was used to test the newly proposed controller. Sensing elements consisted in a load cell (LCM300, Futek, Irvine CA, USA) secured on the distal anchor point of the exosuit, and feeding back cable tension, while elbow angular position was recorded by means of an absolute encoder (AS5047P, AMS, Premstaetten, Austria) aligned with the anatomical joint. In order to detect muscular bio-electric activity, a multi-channel EMG system (Bagnoli Desktop, Delsys, Natick MA, USA) was used to record three muscles that contribute flexing and extending the elbow joint:

namely the long head of biceps (BIC), long head of triceps (TRI) and brachioradialis (BRD): electrodes placement followed the SENIAM guidelines (Hermens et al., 2000). All signals from the exosuits and the EMG workstation were acquired using DAQ board NI 6025E (National Instruments, Austin TX, USA), at a sampling frequency of 1 kHz, while an inner control loop for the exosuit actuation (Fig. 7.2) ran at 10 kHz on a dedicated motor controller (EPOS2 50/5, Maxon, Sachseln, Switzerland). The control architecture was arranged as two separate modules, which ran concurrently. Real-time low-level control of the exosuit and data logging was implemented as a MATLAB/Simulink application. Exosuit high-level control was based on an EMG-driven musculoskeletal model implemented in C++ (Durandau et al., 2018).

7.2.2 Real-time control framework

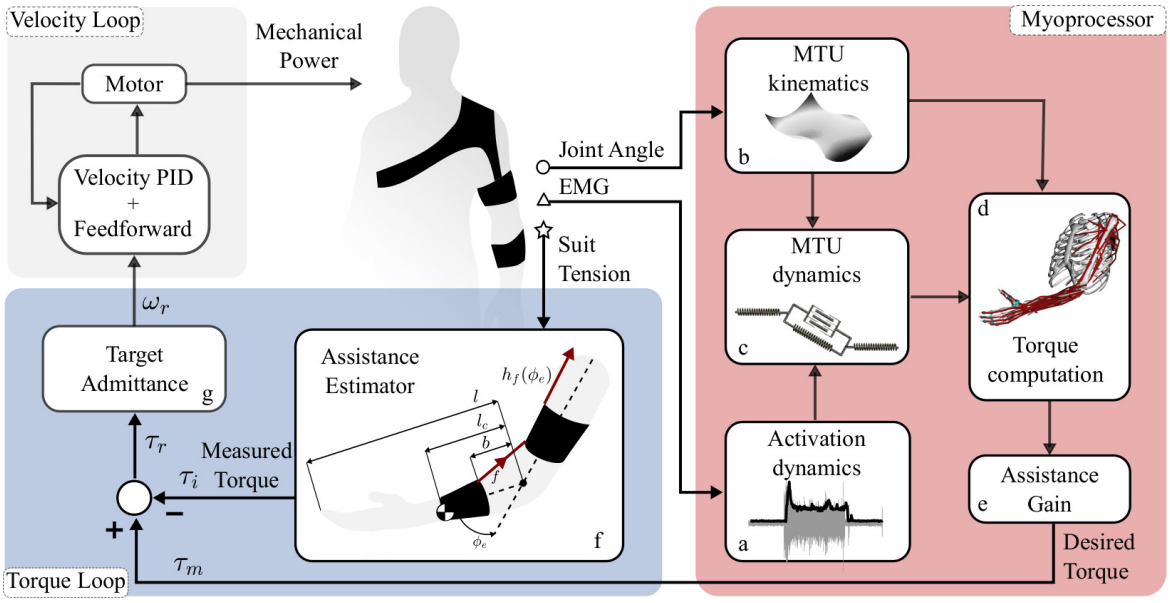

Figure 7.2 *Exosuit control scheme.* The myoprocessor (light red) estimates physiologically accurate torque profiles (τ_m) equal to the torque generated by the muscles spanning the elbow joint. This is tracked by an admittance controller comprised of an outer torque loop (light blue) and an inner velocity loop (light grey). The myoprocessor combines geometric and dynamic properties of muscle-tendon units (MTUs) to estimate the net elbow flexion-extension torque as a function of muscle activation derived from surface EMG electrodes. Myoprocessor estimated torque is compared to the torque (τ_i) delivered by the robot to the human joint. The error torque ($\tau_r = \tau_m - \tau_i$) is then converted to a motor velocity ω_r, delivering assistive power to the suit's wearer.

We developed a real-time framework composed of a high-level controller (myoprocessor) that estimated joint torque from EMG signals and a low-level controller (Section 7.2.2) that provided the assistance needed.

Myoprocessor (high-level controller)

Our proposed real-time EMG-driven modelling framework (Durandau et al., 2018; Sartori et al., 2018) computed elbow flexion-extension torque as a function of (i) three EMG channels and (ii) elbow flexion-extension joint angle from the exosuit encoder (see Suit design and control hardware Section 7.2.1). The model included four components (Fig. 7.2):

– The *Activation dynamics* component (Fig. 7.2a) converted the three input EMGs into muscle activations via a second order muscle twitch model and a non-linear transfer function. The resulting muscle activations were mapped to seven musculotendon units (MTU). The activation derived from the BIC-EMG channel controlled both long head and short head MTUs of the biceps. Activation from the TRI-EMG channel controlled long, lateral and medial head MTUs of the triceps. Activation from BRD-EMG controlled brachioradialis and brachialis MTUs (Sartori et al., 2018).

– The *MTU kinematics* component (Fig. 7.2b) synthesized the three-dimensional musculoskeletal geometry of the human arm (Holzbaur et al., 2005) into a set of multidimensional cubic B-splines.

– The *MTU dynamics* component (Fig. 7.2c) solved for muscle and tendon force using a Hill-type muscle model, as previously described in (Durandau et al., 2018; Sartori et al., 2018).

– The *Torque computation* component projected MTU forces from Fig. 7.2c onto the elbow joint using moments arm from Fig. 7.2b. The EMG-driven modelling framework was then connected to the exosuit low-level controller via UDP protocol to compute the assistance provided by the tendon-driven transmission.

Velocity and torque loops (low-level controller)

The elbow torque estimated via the myoprocessor (Section 7.2.2) was used as reference signal for the exosuit's low-level admittance controller. The admittance controller was comprised of an outer torque and of an inner velocity loop. The torque loop (light blue in Fig. 7.2) compared the reference torque, τ_m, with the interaction torque, τ_i. The interaction torque was

estimated from a load cell recording the cable tension (f), and transformed into elbow torque via the Force/Torque mapping (Fig. 7.2f) (Chiaradia et al., 2018).

Assuming the anchor point was fixed with respect to the user's arm and neglecting the deformations of the fabric and the soft tissues, the interaction torque τ_i was given by:

$$\tau_i = J(\phi_e)^T f \tag{7.1}$$

where $J(\phi_e)$ was the cable's moment arm with respect to the elbow joint. This quantity was a function of the elbow angle, ϕ_e and was defined as

$$J(\phi_e) = \frac{\partial h_f}{\partial \phi_e} \tag{7.2}$$

where $h_f(\phi_e)$ was the cable displacement function, which was described by the following model - see Figure 7.2f for details:

$$h_f(\phi_e) = 2\sqrt{a^2+b^2}\cos\left(\tan^{-1}\left(\frac{a}{b}\right)+\frac{\phi_e}{2}\right)-2b \tag{7.3}$$

where a and b were respectively the forearm's half width and the distance between the elbow's centre of rotation and the anchor point.

The resulting torque error $\tau_r = \tau_m - \tau_i$ was transformed into a desired angular velocity, ω_r, through a PID-like admittance (Target Admittance in Figure 7.2), of the form:

$$Y(s) = \frac{\omega_r}{\tau_r} = P + \frac{I}{s} + Ds \tag{7.4}$$

where the P, I and D gains shaped the dynamic response of the exosuit in order to follow the target τ_m from the myoprocessor. The control gains were tuned to preserve stability, assured a promptness of response comparable with the requirements of the proposed tasks and to minimize the tracking error, τ_r (Yu et al., 2011). They were tuned prior to perform the experiments, on a single subject, and then left unchanged. Finally, the velocity loop (light grey in Fig. 7.2) is responsible for compensation of the intrinsic, unwanted dynamics of the exosuit device (backlash, static and dynamic friction).

7.2.3 Experimental protocol

The study involved six subjects: two female and four male with age 26.0 $\pm$ 2.4 years (mean $\pm$ sd), body weight 78.3 $\pm$ 12.0 kg and height 1.78 $\pm$ 0.08 m. All participants presented

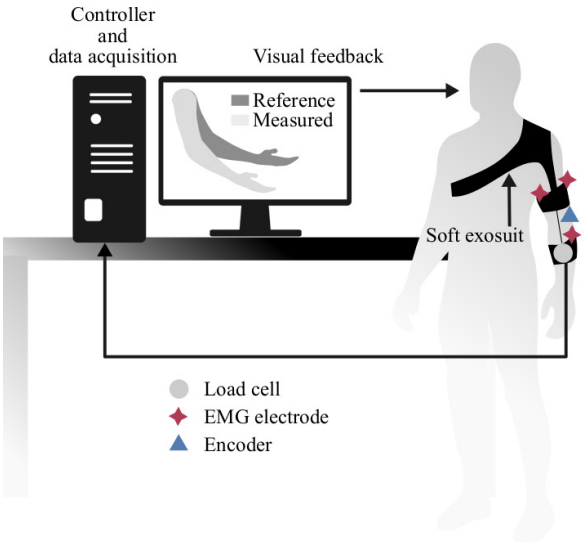

Figure 7.3 *Tracking task to test controller's performance.* We instructed subjects to follow a reference trajectory displayed on a screen in the form of a moving elbow, the position of their own arm was superimposed to provide visual feedback. Setup was the same for both powered and unpowered conditions.

no evidence or known history of skeletal or neurological diseases, and exhibited normal joint range of motion and muscle strength. All experimental procedures were carried out in accordance with the Declaration of Helsinki on research involving human subjects and were approved by the ethical committee of the University of Twente. All subjects provided explicit written consent to participate in the study. To test the performance of the controller, we designed an experiment in which subjects, wearing the exosuit, were requested to track a reference elbow trajectory, which was visually presented via a screen (see Fig. 7.3). The tracking task was performed in two different conditions where the exosuit was powered and unpowered respectively. In the unpowered condition the exosuit cable was slack and the motor turned off. This enabled replicating an unassisted scenario comparable to not wearing the device. The tracking task consisted of a single sequence of minimum-jerk trajectories, replicating features of physiological movements (Flash and Hogan, 1985) in both speed and amplitude.

– Speed: we selected 35 deg/s and 70 deg/s, which respectively correspond to 27% and 55% of the average speed observed in activities of daily living (ADLs) (Buckley et al., 1996).

– Amplitude: three movement amplitudes were tested, 30 deg, 60 deg and 80 deg (Fig. 7.5), where each of them was repeated four times in a random order, for a total of 12 movements per trial.

Similar to (Xiloyannis et al., 2019), the sequence was repeated for different load conditions. The load was placed on subjects' forearm through a specific support to avoid wrist flexion/extension in order not to incur in muscular activation at the level of brachioradialis nerve. Load conditions were three: 0 kg (unloaded), 1 kg and 2 kg. We performed the experiment starting with the unpowered condition for all subjects and randomized load and velocity conditions. During the unpowered condition another workstation ran the algorithm to calibrate the myoprocessor module by using the data collected during dynamic calibration. To avoid fatigue, participants rested for 10 min between conditions.

7.2.4 Myoprocessor calibration

Before running the experiment using the controller shown in Fig. 7.2, each subject performed a calibration task. This allowed the musculoskeletal model of the myoprocessor to be tuned for individual anthropometric features. A 3D motion capture system (Visualeyez II, Phoenix Technologies Inc., Vancouver BC, Canada) was used to record at 100 Hz the trajectories of six markers, placed on anatomical landmarks: third metacarpus, lateral wrist, medial wrist, lateral elbow, medial elbow and acromion. The calibration procedure consisted of three different phases: (i) static pose acquisition, (ii) a maximum voluntary contractions (MVC) trials and (iii) a dynamic calibration. During the static pose, we recorded the three-dimensional location of reflective markers by means of motion capture. For each subject, the open-source software OpenSim was used to linearly scale a generic musculoskeletal model (Holzbaur et al., 2005) to match each individual's arm anthropometry. During the MVC trials, a series of isometric contractions for each muscle group were performed to extract EMG peaks, used successively for EMG signal normalization. During the dynamic calibration, subjects were requested to follow reference trajectories, visually feedback on a screen, by flexing and extending the elbow at different speeds. Recorded EMG signals, joint angles and reference torques were used to calibrate the myoprocessor: joint moments were extracted using the OpenSim inverse dynamics tool by following the procedures described in (Durandau et al., 2018). The calibration process estimated the values of the internal model parameters that minimised the normalized error between the myoprocessor torque estimates and the reference torque profiles. Tuned parameters included optimal fiber length, tendon

slack length, maximal isometric force and EMG-to-activation filtering coefficients (Durandau et al., 2018).

7.2.5 Data analysis

Raw EMG signals were processed online using a 50 Hz notch filter, high-pass filtering (35 Hz), full-wave rectification and low-pass filtering (4 Hz, second-order Butterworth filter), and then normalized with respect to individual MVC level recorded during the calibration procedure. In order to test subjects' performance across the different experimental conditions a set of indicators was evaluated:

- Tracking accuracy: we computed the coefficient of determination r^2 and the root means square error RMSE between reference and measured elbow trajectories performed by the subjects over the different conditions. The two metrics were also used to quantify the ability of the myoprocessor to estimate the elbow joint torque by comparison with the OpenSim inverse dynamics tool.

- Time delay: to assess the time lag occurring between the EMG signal onset and the exosuit motor drive engagement, we calculated the time window between the acquisition of EMG signals and the torque loop output, ω_r. We used two different approaches: offline and online. In the offline method, we simulated 140 EMG pulses and collected the output from the target admittance (Fig. 7.2g), which drove the exosuit actuation. The online method estimated the onset time during subjects' performance. We computed the norm of the derivative of both EMG linear envelopes and reference elbow angular velocity. In both signals we estimated the onset as the time instant at which the signal was greater than 10 % of its peak magnitude. We then extracted the time lag as the difference between the onset time of the velocity and the muscle, which activated first – typically, the biceps.

- Muscular activity: we evaluated the Root Mean Square (RMS) of both EMG signals and muscle forces, estimated from the myoprocessor, under all experimental conditions.

7.2.6 Statistical analysis

Whenever appropriate, we assessed normality of the statistical distribution using the Kolmogorov-Smirnov Test and the sphericity condition for repeated-measures ANOVA with the Mauchly Test. All metrics resulted normally distributed. When the sphericity condition was violated,

we applied the Greenhouse-Geisser correction. Significance of differences in muscular activation was inferred for different conditions using performance indicators (%MVC and muscle forces) across the two main setups (powered vs unpowered exosuit) and load conditions (unloaded vs 1kg vs 2 kg). For the kinematic analysis we considered the average value of the movement amplitude and velocity. A repeated-measures ANOVA (rANOVA) within-subject factors was performed: 'powered vs unpowered', 3 'loading conditions' (unloaded, 1 kg and 2 kg) and their mutual interaction. The significance level was set at $p<0.05$. We also reported for ANOVA the notation F(n,d), where n are the DOFs of the numerator - i.e. powered/unpowered condition - and d of the denominator - i.e. subjects.

7.3 Results

7.3.1 Myoprocessor reliably estimated elbow joint torque

Fig. 7.4a displays the myoprocessor estimated torque in the unpowered condition and zero load as well as the reference torque obtained by inverse dynamics (extracted from the trajectories showed in Fig. 7.5). The coefficient of determination depicted in Fig. 7.4b was calculated for each subject by averaging on all movement amplitudes (30 deg, 60 deg and 80 deg), and velocities (35 deg/s and 70 deg/s).

For all subjects and across all trials the coefficient of determination r^2 was always higher than 0.82, with a mean value of $r^2 = 0.87 \pm 0.04$ (mean $\pm$ sd). The RMSE was lower than 0.02 Nm/kg and the mean value was 0.0146 ± 0.0051 Nm/kg (mean $\pm$ sd).

7.3.2 Exosuit responsiveness was comparable to the electromechanical delay

The shorter the latency between EMG onset and electromechanical actuation, the more transparent the exosuit was perceived by the wearer. This may be due to optimal synchronization between muscle contraction and exosuit actuation. Fig. 7.4c shows the distribution of the estimated latencies, including the mean latency and the standard deviation across all simulation frames (140 spike frames). Using Chebyshev's Theorem we also estimated the maximal expected latency within a 95% confidence. We found that in 95% of cases the onset of the controller response occured within 53.8 ms, which is comparable with the physiological upper limb electromechanical delay – 55.5 ms according to (Norman and Komi,

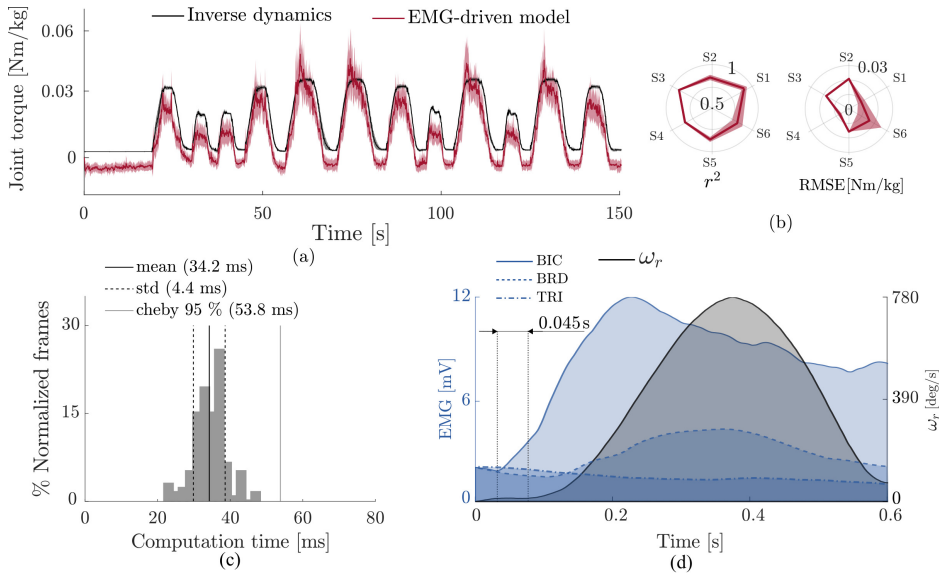

Figure 7.4 *Accuracy and latency of the model-based myoprocessor.* Panel (a) shows the EMG-driven model estimated torque, averaged over all subjects (red line, mean ± sd), compared to the inverse dynamic torque (reference value, black line, mean ± sd) during the tracking task. Torques were normalized using the mass of each subject. Panel (b) displays the coefficient of determination, r^2, and the root mean square error between the two torques for each subject, averaged over repetitions, velocities and loads. Panels (c) and (d) show the time delay of the latency in exosuit reaction. Panel (c) shows the distribution of latencies between the EMG input and the motor speed, including the average latency (mean ± sd) and the maximal expected error within the 95% percentile of data. In panel (d) we report a typical delay between the activation of biceps (BIC) and the target admittance output ω_r (see Fig. 7.2g) during a trial. The controller latency is within the time range of the electromechanical delay of upper limbs natural muscle fibers (55.5 ms).

1979). Fig. 7.4d exemplifies a typical delay of 45 ms between the onset of BIC and the target admittance output ω_r during a tracking movement.

7.3.3 Assisted elbow motion accurately tracks reference trajectories

Fig. 7.5a shows that reference trajectory tracking accuracy was not affected by the exosuit assistance with respect to the unpowered condition and in the presence of loads. Average tracking accuracy measured using the coefficient of determination r^2 during unloaded trial (0 kg) for unpowered condition was 0.94 ± 0.03, while for powered condition was 0.90 ± 0.03 (mean ± sd). We found similar values for the maximally loaded setup (2 kg) with average r^2 being 0.94 ± 0.03 for unpowered and 0.90 ± 0.02 for powered conditions respectively. Regarding the RMSE, we found 10.3° ± 2.3° for unpowered condition and 10.7° ± 2.5° for

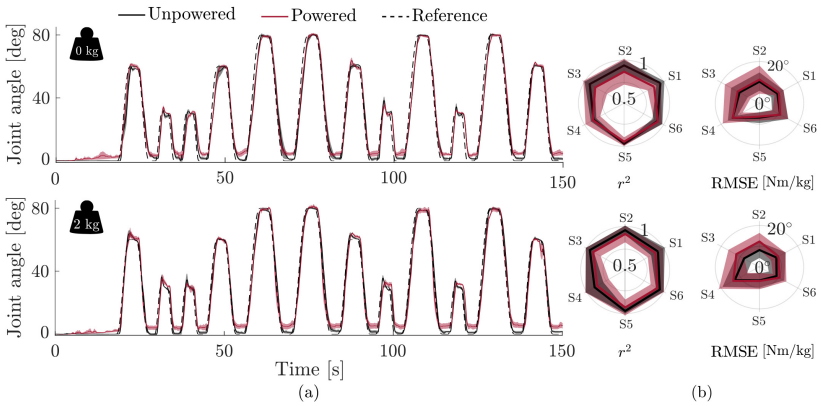

Figure 7.5 *Human tracking accuracy.* Panel (a) shows the tracking accuracy averaged over all subjects (mean ± sd) for the unloaded condition (top) and the 2 kg condition (bottom). Black continuous lines represent the unpowered condition, red lines represent the powered condition and the dashed line the tracking reference. Panel (b) reports the coefficient of determination r^2 and the root mean square of the error RMSE for each subject, computed on the unloaded trial (top) and 2 kg trial (bottom).

powered condition during unloaded trial. In the maximally loaded setup (2kg) we found 9.0° ± 2.2° during the unpowered condition and 11.0° ± 2.4° during the powered condition. A Wilcoxon signed-rank test between the two aforementioned analysis confirmed that wearing the exosuit did not significantly reduce the ability to track a reference trajectory (p = 0.16) in terms of delay by looking the r^2, but we found a significative difference in the RMSE value (p = 0.0034).

7.3.4 Exosuit assistance reduced muscular activity

A significant difference was observed in muscular activation across conditions: in particular Fig. 7.6 shows EMG traces for a representative subject performing tracking movement in unloaded (Fig. 7.6a) and 1-2 kg loads (Fig. 7.6b-c) conditions, respectively with and without exosuit assistance. For the unloaded condition (a) the difference between the EMGs waveforms was negligible, indicating that the controller was able to not feel the presence of the exosuit assuring an almost complete mechanical transparency of the device. When movements were performed in the presence of a load (Fig. 7.6b-c), the EMG amplitude, with the exosuit assistance, was substantially lower, proving that the myoprocessor accurately estimated the elbow torque from muscular activity and consequently the controller delivered assistance to the subjects against gravity. Analysis of muscular envelopes revealed that in all muscles and in all powered conditions the EMG activity decreased significantly with respect to the unpowered conditions. In particular, the BIC muscle displayed a significant decrease

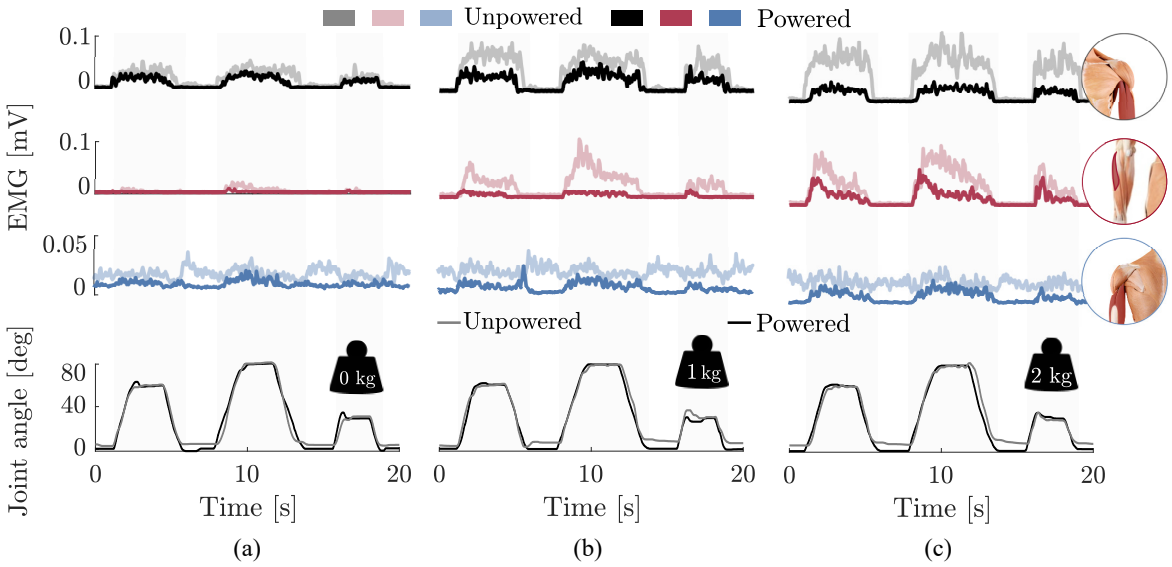

Figure 7.6 *Muscle activation and tracking.* EMG linear envelopes of a representative subject who performed three consecutive tasks at the highest velocity, with 0 kg load (a), 1 kg (b) and 2 kg (c) in both the powered and unpowered conditions. During the powered condition, the exosuit reduced the biceps activity (black line) by 35.6 %, 55.1 % and 73.0 %, brachioradialis activity (red line) by 49.5 %, 77.0 % and 58.4 % and the triceps activity (blue line) by 35.6 %, 59.7 % and 51.9 % for 0 kg, 1 kg and 2 kg loads, respectively.

(F(1, 5) = 35.9, p = 0.0018) as well as the BRD muscle (F(1, 5) = 12.6, p = 0.016) and the TRI (F(1, 5) = 9.8, p = 0.026).

Fig. 7.7a shows the trend of EMGs RMS, expressed in % of MVC, for two elbow velocities (min and max), with increasing loads and powered vs unpowered conditions. During powered conditions the activity of the biceps only increased less than 2% between 1 kg and 2 kg loads. With regard to the muscle forces estimated by the myoprocessor (Fig. 7.7b), we observed similar results, where BIC (F(1, 5) = 12.1, p = 0.018), BRD (F(1, 5) = 20.0, p = 0.0066) and TRI (F(1, 5) = 14.6, p = 0.012) reported a significant reduction in all powered conditions. Also in this analysis, the BIC, which was the muscle predominantly working against gravity, was found to increase by less than 5 N between 1 kg and 2 kg loads.

7.4 Discussion

We developed a human-machine interface, which combined, for the first time, a realistic, subject-specific real-time EMG-driven myoprocessor with an upper limb active soft exosuit.

The proposed myoprocessor used EMGs and kinematic data to estimate the net muscle-generated elbow flexion-extension torque, which was used to determine the assistance

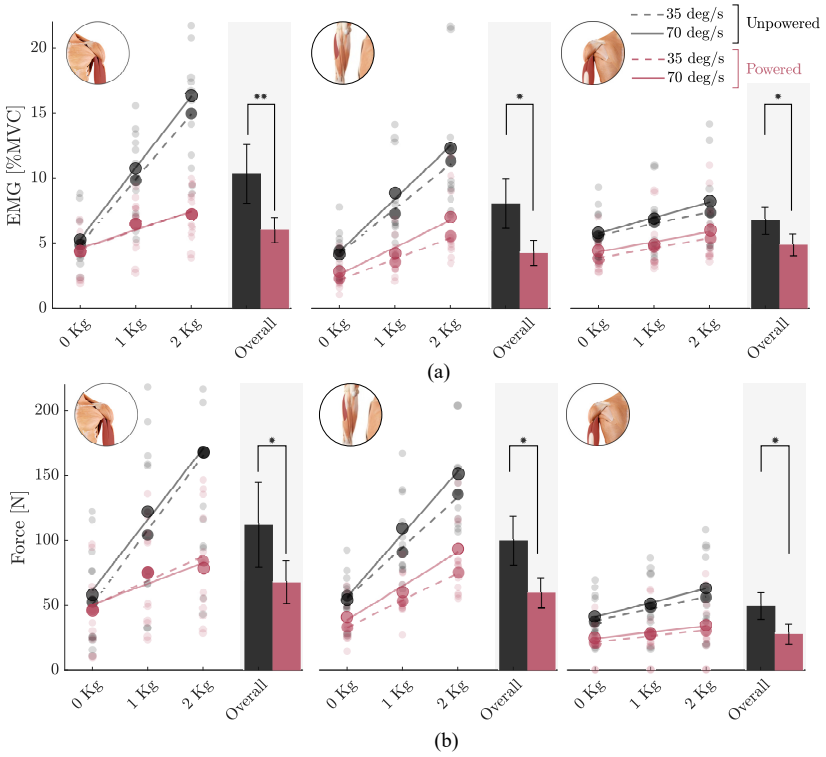

Figure 7.7 *EMG activity and estimated muscle force.* Panels (a) and (b) show EMG amplitude and estimated muscle force, respectively. Translucent dots are the values for each participant, opaque ones the average over subjects; lines indicate the trend across loads (dash line for 35 deg/s and continuous line for 70 deg/s). From left to right we report the biceps, the brachioradialis and the triceps. The marks ** and * above the bar plots denote, respectively, high significant ($p<0.01$) and significant ($p<0.05$). EMG amplitude and force of all muscles were significantly lower in all powered conditions.

provided by the exosuit. That is, the exosuit added a fraction of the estimated elbow torque to support a range of movements. A distinctive aspect of this control scheme is that the myoprocessor directly incorporated changes in arm+exosuit dynamics and task requirements (e.g. presence of additional loads or different speeds), with no need for additional re-calibration and low-level controller re-tuning. In this way, the exosuit effectively operated as an extension of the human musculoskeletal system, dynamically adapting to different external mechanical loads.

We assessed the performance of the controller during tracking tasks – a sequence of arm flexion and extensions in the sagittal plane – carried out at different speeds as well as including lifting of different loads.

Results showed that model-based estimates of elbow torques well matched reference torque values across all tested kinematic and load conditions (Fig. 7.4a), thereby validating

model estimation accuracy. Results also showed that the exosuit tracked EMG-decoded elbow torques with high accuracy, thereby mimicking human musculoskeletal forces.

These are necessary conditions to be met for actively supporting elbow rotations while not inducing unwanted motions or affecting natural movements, as how it usually happens when in the presence of a rigid exoskeleton. In this context, results from human tracking tests confirmed that during powered tasks, accuracy did not deteriorate with respect to unpowered tasks across all subjects and trials (Fig. 7.5). When compared to a previously presented gravity compensation controller (Xiloyannis et al., 2019), our proposed solution displayed improved tracking accuracy: mean r^2 with gravity compensator assistance was 0.80 ± 0.06, while with our HMI was 0.90 ± 0.04. We found a significant difference in the root mean square tracking error variations ($p = 0.034$). However the difference between the powered and unpowered condition was always less than 2°. Importantly, the gravity compensator controller (Chiaradia et al., 2018) also needed PID parameters tuning for each subject, which made it hard to provide an adaptive assistance depending on the external dynamic conditions. The PID module specifies the exosuit behavior at the human-machine physical interface and the parameters need to be set to provide stability within the myoprocessor range of outputs and to prevent saturation of the actuators. As the myoprocessor output torque had similar magnitudes for all subjects, we tuned the PID module on the basis of one single subject only. This procedure also reduced the controller set-up time and allowed focusing on the myoprocessor contribution to the system overall performance. However, adapting the PID gain to individual subjects may further increase the control performance. Future studies will address a systematic analysis of how generic vs subject-specific PID gains affect control performance.

Our results suggest that the exosuit response to EMGs may be faster than HMIs based on human-exosuit interaction forces (Fig. 7.5). EMG-controlled exosuits can react to EMGs theoretically before physical joint force and motion is generated. In the case of interaction force, detectable joint force and motion must occur before exosuit assistance can be computed and delivered to the human, something that would limit final applicability, e.g. according to this scheme, exosuits can only provide assistance after detectable movement is produced by the user. Importantly, our approach did not require any modification in hardware with respect to interaction-force based controllers we previously developed and tested on the same device (Xiloyannis et al., 2019). We used the same configuration showed in (Xiloyannis et al., 2019) and we integrated our HMI in the control loop. Furthermore, results showed that the exosuit intervention reduced effort in major elbow flexors across increasing velocity and load conditions: this was reflected by a decrease of both EMG and mechanical force

magnitude in the transition from unpowered to powered conditions, i.e. both muscle EMGs and forces across the 1 kg and 2 kg conditions varied within similar absolute ranges (Fig. 7.7). Results also showed that the exosuit support preserved muscle force generating capacity across multiple velocities and loads (Fig. 7.7b). This condition was observed in particular on the biceps, the main elbow flexor muscle.

The exosuit assisted only in flexion and allowed unassisted extension along gravity by releasing its artificial tendon. Therefore, the muscles that predominantly contributed to control the exoskeleton during flexion were the biceps and brachialis muscles. However, it was necessary to include also triceps in the myoprocessor module for two reasons. The first one concerned the elbow net torque estimation for which triceps contribuite to: in the hypothetical and extreme scenario where subjects were able to exclusively contract the flexor muscles (leaving the triceps completely off), there would still be passive force produced by the triceps due to muscle stretch. These forces could be in the order of several tens of newton and therefore not negligible. The correct estimation of these passive resistive forces would provide the best possible estimation of net elbow torque. If we neglected these passive torques we could have had potentially over or under estimation of the net elbow torque, thereby providing sub-optimal assistance to the human. The second reason regarded the exosuit control: the mechanical system was not backdriveable, so the triceps was used to release the artificial tendon during elbow extension and its initial burst triggered the releasing of the motor and made the device transparent during elbow extension too. In this context, the reduction in the triceps muscle activity (Fig. 7.7) was an unexpected result. It could be caused by the participants having to follow a predefined trajectory, displayed on a screen. This might have caused the descending motion to not be a purely concentric one, that implies modulation of agonist and antagonist muscle to preserve accuracy. Fig. 7.6 between the exosuit and the human arm.

In this context, our also showed that the biceps activity in the powered condition varied minimally across loads: this all provided evidence that the proposed myoprocessor could make both the worn device and the external load transparent to the human operator during dynamic tasks. Since small discrepancies between the onset of human limb movement and that of the parallel exosuit can significantly increase human muscle effort, our results demonstrated that our approach ensure a reliable synchronization approach could directly exploit the electromechanical delay (EMD) for prompt device control. Results showed that, across the recruited subjects, the EMD was sufficiently large (20 - 48 ms, Fig. 7.4) for decoding mechanical moments from EMGs before the voluntary movement took place. Moreover, the EMD was sufficiently consistent to be considered as a hard real-time deadline

for the exosuit control. Meeting this deadline within our proposed HMI assured the exosuit to be actuated synchronously with the user's muscle mechanical function. This is an additional advantage with respect to current HMIs that actuate wearable robots solely on the basis of the detection of externally measurable forces, which could not provide support until the operator has produced detectable dynamics at the interface with the machine (Asbeck et al., 2014).

Our study presented limitations. We explored a limited range of movements: this was due to limitations in the exosuit actuation stage. Experiments involved only healthy subjects. Future work will involve neurologically impaired subjects. The device actuated a single degree of freedom, so during the calibration it was important to avoid movement that involved other joints. For this reason, in this study we constrained the wrist to best test our approach. The exosuit was only designed for the elbow flexion-extension. We did not model any degree of freedoms at the wrist and therefore, we avoided motions at these DOFs. Future works will focus on testing control of multiple soft mechatronic DOFs, e.g. simultaneous control of elbow and hand joints in exosuits. Experiments required subject-specific calibration. However, it is worth stressing that this calibration is not needed to be performed every time one uses the device. In this context, there are two type of parameters in the myoprocessor module: anatomical parameters and filtering parameters. Once identified, anatomical parameters should not vary anymore for a grown adult because they are linked to the anatomy of the subject. In a previous study (Sartori et al., 2018), using the same myoprocessor, model calibration was always performed a number of days prior to real-time prosthesis control experiments. This provided evidence of the EMG-model framework ability of retaining subject-specific parameter consistency across time scales. On the other hand, filtering parameters (MVC and EMG-to-activation coefficients) may be less stationary as they depend on EMG-skin impedance, fatigue and other factors, but this quantification requires a stand alone study, planned in future.

In this study we did not compare our HMI with different approaches such as simpler direct-EMG controllers. In this context, the added complexity of our model is repaid by a twofold benefit: (1) the ability to capture and adapt to unpredictable and varying external dynamics, tested in the different loads conditions (Fig. 7.6, 7.7); (2) a higher robustness to movement artefacts and noise in the EMG signals. A proportional controller, based only on processed EMG signals, could not capture all the aspects related to the dynamics of the arm, since it ignores muscles geometry and EMG-to-activation conversion. The second advantage directly translates to a higher usability in real-world scenarios: in (Sartori et al., 2018), we showed that the myoprocessor, relying on muscular geometry as well as activation levels, is robust to mechanically induced movement artefacts in the EMG signals,

such as arm positions or cable movements. In future studies, we will directly compare the myoprocessor to other myoelectric control techniques (e.g. proportional EMG control), by enlisting a larger number of subjects and conditions (after hardware improvements) to test the generalizability. We will also test the exosuit control on subjects with neuromuscular conditions to assess to what extent the model-based HMI can adapt to abnormal anatomies and affected muscular activation patterns (Durandau et al., 2019). Finally, the study only explored highly controlled elbow rotations and did not include functional real-life tasks. However, our approach demonstrated adaptation to external load that could be applied in unstructured environments. The robustness of the controller, combined with a symbiotic HMI, can provide cooperation between the user and the exosuit. The next step will adapt the system in order to port this device in the real world.

In conclusion, we demonstrated the possibility of controlling exosuits via a real-time myoprocessor enabling adaptive support during a diverse range of mechanical loads and kinematics during elbow motion. The integration of model-based HMIs with soft mechatronics has the potential to open new frontiers in highly ergonomic wearable assistive robots, which will behave symbiotically with humans.

Chapter 8

Myoprocessor-driven force fields to induce virtual changes in human biomechanics: a feasibility study

8.1 Introduction

Estimating the contributions of individual muscles to limb movements is crucial to our understanding of the organization of the motor system.

The temporal evolution of muscle activity during a movement may be the end result of a on-line optimization process, involving the trade-off of accuracy and effort (Todorov and Jordan, 2002). It has been suggested, however, that the motor system may have a modular organization (Bizzi et al., 2008; Cheung et al., 2005; d'Avella et al., 2003; Tresch et al., 2006, 1999), so that muscle activity is generated by combining a smaller number of motor modules, or muscle 'synergies'. An alternative but similar hypothesis is that muscle activation follows stereotypical patterns, but they reflect previous individual experience rather than structural constraints. Both hypotheses predict limitations in the ability of muscle activation to adapt to novel situations.

In pathological conditions, characterizing the roles of the individual muscles may provide a basis for devising personalized forms of treatment. In particular, understanding these control mechanisms is a prerequisite for devising ways to selectively modify the activity of individual muscles or muscle groups for neuro-rehabilitation purposes.

Electromyographic signals (EMG) in conjunction with detailed musculoskeletal models allow to simulate the force generated by a specific muscle or group of muscles (Thelen,

2003). Musculoskeletal models are widely used in biomechanics, for instance to predict the load to a particular joint (Manal et al., 2002) or to predict joint torques during movements (Cavallaro et al., 2006). Model simulations may be performed in real-time, driven by the recorded muscle activity and movement kinematics. These computational modules have been referred as 'myoprocessors' (Durandau et al., 2018). Myoprocessors have been used as biofeedback during gait studies (Pizzolato et al., 2017) or to control external devices, such as an exoskeleton (Buongiorno et al., 2016), soft wearable exosuit (Lotti et al., 2020) or a prosthetic hand (Sartori et al., 2019).

Recently, myoprocessors have been used to computationally alter muscles directions of action ('virtual biomechanics') in order to study the motor system's modular structure and its adaptive capabilities (Berger et al., 2013; de Rugy et al., 2012). In these studies, the endpoint force – in isometric conditions and with a fixed arm configuration – was estimated from the recorded activity of multiple upper limb muscles. The endpoint force was then used to operate a virtual point mass, displayed as a cursor on a computer screen.

In (de Rugy et al., 2012) individual muscles were virtually 'removed' so that the same muscle activation produced a different endpoint force. The study examined whether muscle activity adapts in order to recover the previous endpoint force, thus compensating for muscle removal. The main finding was that EMG activity indeed changes with training – the action of the removed muscle is taken over by muscles with similar directions of action. However, the activity of this muscle does not go to zero but rather increases dramatically, even though it has now become task-irrelevant. A similar approach ('virtual surgery') (Berger et al., 2013) specifically focuses on the degree of modularity of the motor system, i.e. its organization in terms of muscle synergies. Two types of perturbations – compatible and incompatible – were applied to the myocontroller. In compatible surgery, the original endpoint force could be generated by simply recombining existing synergies. In incompatible surgery, the target endpoint force could only be achieved by rearranging synergies. The modularity hypothesis predicts that adaptation to compatible surgery is faster than that to incompatible surgery. The findings seem to confirm this prediction.

One major limitation of these approaches is that they only focus on isometric force generation with a fixed body configuration, with no actual body movements. Neural control of limb movements requires precise coordination of multiple degrees of freedom and compensation of dynamic interaction torques (centripetal/Coriolis). Also, during movements the limb resistance to perturbation (stiffness) is regulated through muscle cocontraction (Franklin et al., 2008; Tee et al., 2010). The contribution of individual muscles to both movement and cocontraction is determined by their geometric arrangement and by the dynamics of

contraction. In conclusion, generalization of the above results to control of limb movements must be taken cautiously. Here we extend the above results to a more general situation, involving multi-joint arm movements. Our aim is to use the myoprocessor module to generate force field on a planar robot manipualndum in order to emulate the mechanical action of one muscle or muscle groups. This technique allows to effectively modify the geometric arrangement (and therefore the directions of action) of existing muscles and/or their dynamic properties.

8.2 Materials and Methods

8.2.1 Myoprocessor-controlled force fields

The myoprocessor-controlled force field concept is summarized in Figure 8.1. A detailed model of arm geometry, muscle geometry and muscle contraction dynamics, in conjunction with measures of arm kinematics and muscle activity is used to predict the joint torque generated by an individual muscle, in real-time. If the movements are limited to shoulder and elbow rotations and the arm moves in a plane, the muscle torques can be translated into an equivalent endpoint force. A planar manipulandum is programmed to generate an endpoint force corresponding to the simulated 'virtual' muscle or muscle group, which is then applied to the subject's hand. The force generated by the manipulandum ('robot force' in Figure 8.1) is added to the actual muscle force - the endpoint equivalent of the torque generated by the actual muscle. The sum of these forces represents the overall contribution of that muscle ('virtual muscle force').

8.2.2 Experimental Apparatus

The experimental apparatus involves a planar robot manipulandum with two degrees of freedom (Casadio et al., 2006), a Force/Torque Sensor (Gamma, 130-10, ATI Industrial Automation, USA), mounted on the robot handle, and a multi-channel wireless EMG system (EMG Wave plus, Cometa srl, Italy). One infrared camera (Slim 13, Optitrack, NaturalPoint Inc, USA) placed above the subject's workspace recorded the movements of three markers, placed on the subject's shoulder acromion, the elbow joint, and on the robot handle. All markers approximately move on the same horizontal plane. We recorded the activity of nine muscles: anterior deltoid (aDEL), posterior deltoid (pDEL), long and short head of biceps (lBIC, sBIC), long and lateral heads of triceps (loTRI, laTRI), brachioradialis (BRD), pectoralis major (mPEC) and upper trapezius (TRA). We used one additional electrode,

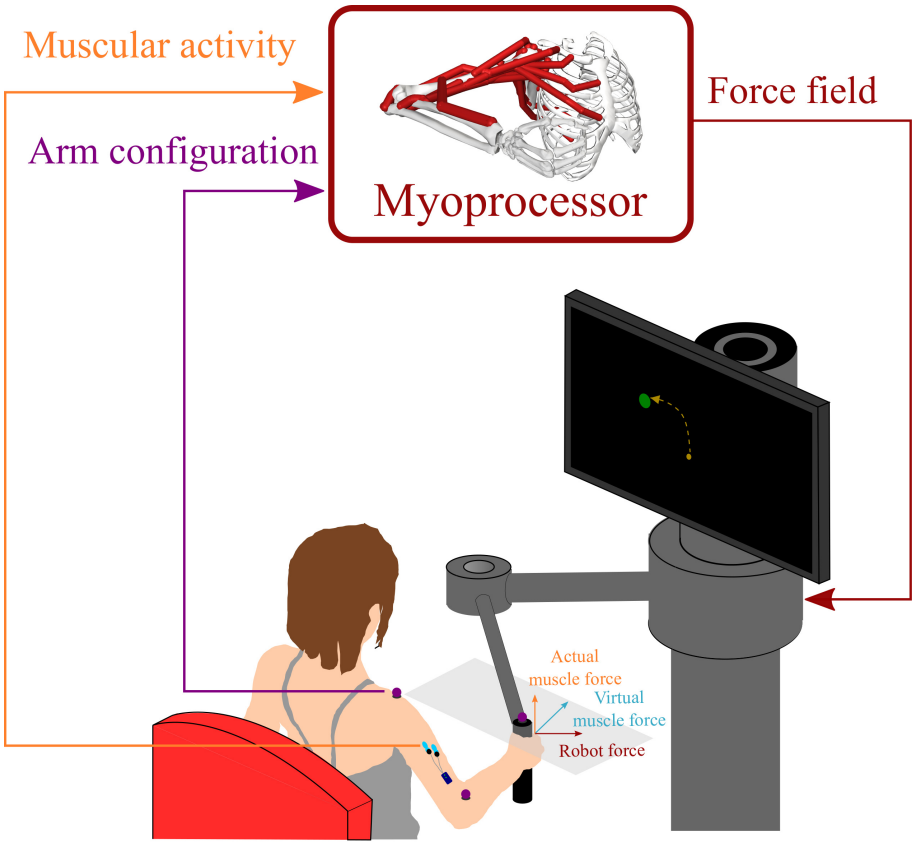

Figure 8.1 *The myoprocessor-controlled force field concept.* The robot generates a force which reflects the behavior of a simulated muscle. Muscle simulation relies on a detailed model of arm kinematics, muscle geometry and of muscle contraction dynamics. This allows to computationally modify the directions of action of individual muscles, which are now determined by the summation of the contributions of the original muscle and by that of their simulated counterpart

placed on the sternum, to record the electrocardiography signal. Electrode placement was based on the SENIAM recommendations (Hermens et al., 2000).

The subjects sat in front of a 40” computer screen placed vertically at eye level at a distance of about 1 m, and grasped the handle of the manipulandum with their right hand. Torso and wrist were restrained and the seat position was adjusted so that, with the cursor pointing at the center of the workspace, the shoulder and the elbow joints were flexed about 45° and 90°. The forearm was suspended to the ceiling to partly compensate for the effect of gravity. This arrangement only allowed planar shoulder and elbow rotations in the horizontal plane.

The experimental set-up involved two computers (PC1 and PC2). Two separate applications ran on PC1, respectively managing EMG recording, early processing and extraction of the EMG envelopes, and extracting the marker positions from the camera data. The latter was only used during calibration (see below). Another application, running on PC2, was responsible for managing the experimental protocol, force recordings and robot control. The two application running on PC1 communicated in real-time with PC2 through two separate user datagram protocol (UDP) data streams. The software implementation was based on Simulink and the Desktop Real-Time toolset (Mathworks, Natick USA).

8.2.3 Myoprocessor model

The myoprocessor model is composed of four modules, as shown in Figure 8.2. The structure and the aim of each block are the same described in Chapter 5.

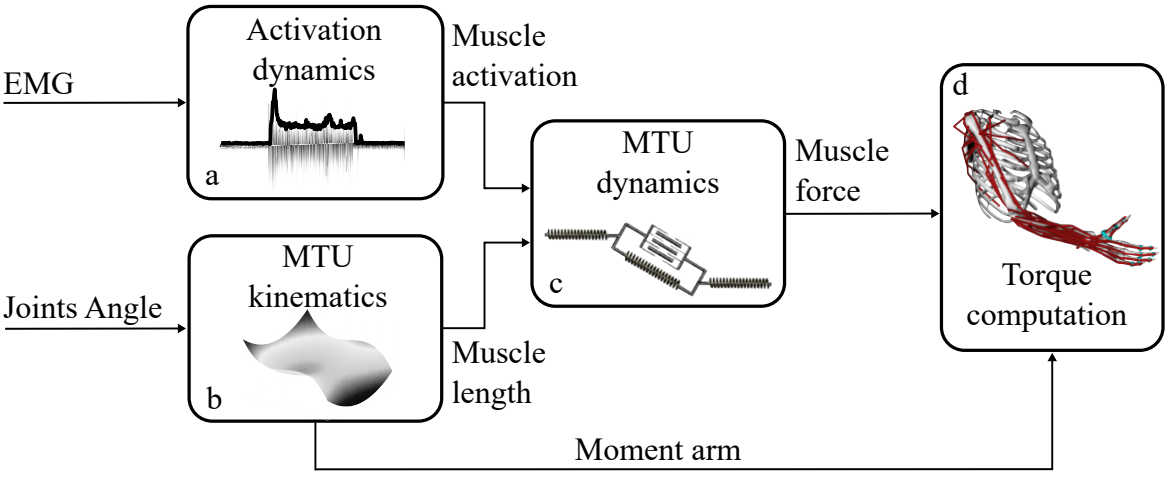

Figure 8.2 *The myoprocessor module scheme.*

8.2.4 Calibration of the myo-processor module

We improved the task described in (Lotti and Sanguineti, 2018) for the myoprocessor module calibration. The pipeline consisted of three procedures:(i) a maximum volontary contraction task (MVC), a resting state acquisition and a model calibration task. During the MVC, subjects performed a series of task in order to achieve the maximum contraction for each muscle included in the model. This procedure was useful to normalize the EMG activity. The other two procedures were performed in conjuction with the planar robot manipulandum (Casadio et al., 2006). During the resting state acquisition subject had to grasp the robot for 30 sec without performing movement: in this phase we acquired the data for the ECG blinking and for the muscle activity baseline acquisition. As the recorded mPEC muscle activity turned out to be contaminated by the cardiac activity, we used the recorded ECG signal to remove this artifact by using a cross-correlation method (Hof, 2009). The cancellation filter was then used on-line in order to filter out the ECG artifact from the mPEC activity. The model calibration task included reaching movements through a sequence of five targets, $P_1, \ldots, P_5$ evenly distributed within the whole arm workspace, see Figure 8.3 (right). The whole sequence (movement and force generation) was repeated for a total of 3 times. The total duration of this task was about 40 min.

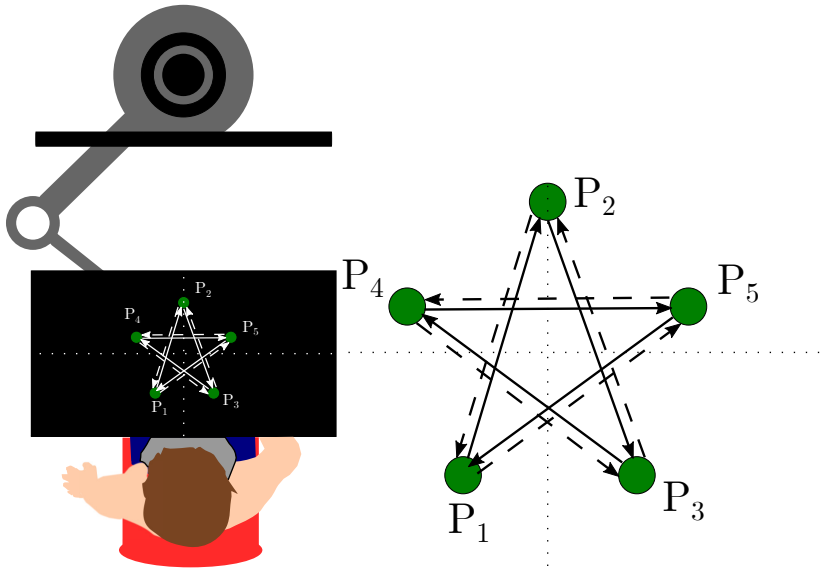

Figure 8.3 *Calibration procedure*. Workspace representation in scale (left), reaching movements through a sequence of five targets (right).

We estimated during the model calibration task upper arm and forearm length and shoulder position (L_1, L_2, x_s) by using camera data. The IR camera acquired (sampling rate: 100 Hz) and detected the position of the three markers. The camera was previously calibrated

by comparing the trajectories of the 'robot' marker with the end-effector trajectories estimated through the robot encoders. We used the Direct Linear Transform to translate these measures into Cartesian coordinates in the robot coordinate frame. Although the set-up allows for the real-time estimation of the joint angles $q_1(t)$ and $q_2(t)$, from the recorded marker positions, the camera measurements were only used off-line to estimate the skeletal geometry (L_1 and L_2). Using these parameters, through inverse kinematics we then derived on-line the joint angles from the endpoint trajectory. This is less accurate than estimating the joint angles directly from the camera measurements, but does not require to process the latter in real-time and is an acceptable approximation for planar arm movement with fixed shoulder. We also used camera data as input for the open-source software OpenSim in order to linearly scale a generic musculoskeletal model (Holzbaur et al., 2005) to match each individual's arm anthropometry. From the scaled model we extracted the musculotendon lengths and moment arms through the multidimensional spline techniques (see Chapter 2). We calibrated the myoprocessor module by using the kinematic data, EMG, and Force signals recorded during the reaching movements in the model calibration task. By using the simulated annealing algorithm (Das and Chakrabarti, 2005), we minimized the function

$$\sum_{i=1}^{2}\sum_{t=1}^{N}(\tau_i^H(t)+\tau_{dyn}(t)-\tau_i^M(t))^2 \tag{8.1}$$

where τ^H is the torque obtained by measured the force at the end effector $\tau^H = J(q)^T \cdot F^H(t)$, τ_{dyn} is the upper-limb inverse dynamics and τ^M the torque estimated by the myoprocessor model. The upper-limb inverse dynamics τ_{dyn} is estimated by using a normative model (Winter, 2009)

$$\tau_{dyn} = M(q(t))\ddot{q} + C(q(t),\dot{q}) \tag{8.2}$$

where

$$M(q(t)) \triangleq \begin{bmatrix} I_2 + M_1 Lg_2^2 + I_1 + M_1 Lg_1^2 + M_2(L_1^2 + 2L_1 Lg_2 \cos(q_2(t))) & I_2 + M_1 Lg_2^2 + M_2(L_1 Lg_2 \cos(q_2(t))) \\ I_2 + M_1 Lg_2^2 + M_2(L_1 Lg_2 \cos(q_2(t))) & I_2 + M_1 Lg_2^2 \end{bmatrix}$$

$$C(q(t),\dot{q}) \triangleq \begin{bmatrix} -M_2 L_1 Lg_2 sin(q_2(t))\dot{q_2}^2 - 2M_2 L_1 Lg_2 sin(q_2(t))\dot{q_1}\dot{q_2} \\ M_2 L_1 Lg_2 sin(q_2(t))\dot{q_1}^2 \end{bmatrix}$$

I_1, I_2: moment of inertia of the arm and forearm;

M_1, M_2: mass of the arm and forearm (Hogan et al., 1990);

$$\begin{bmatrix} Lg_1 \\ Lg_2 \end{bmatrix} \quad \triangleq \begin{bmatrix} 0.436L_1 \\ 0.682L_2 \end{bmatrix} \quad ;$$

We considered in the function both shoulder and elbow torque (τ_1, τ_2). The parameters involved in the optimization function were the optimal fiber length, the tendon slack length, the maximum isometric force, the filtering coefficients and the non-linear coefficient in the activation dynamics block (Lloyd and Besier, 2003).

8.2.5 Adaptation experiment

The adaptation experiment consisted of a series of center-out reaching movements in six different directions (0°, 60°, 120°, 180°, 240°, 300°) with a 10 cm amplitude. The subjects were instructed to place the hand at start position (white circle with $\varnothing$1 cm located at the center of the workspace). When a new target appeared (white circle with $\varnothing$1 cm), they had to move toward it as fast and as accurate as possible. Participants received a speed visual feedback. The target turned green if participants reached it within a certain time range (1$\pm$ 0.1 sec), otherwise the target turned red.

The experimental protocol was organized into epochs (one epoch: six repetitions for each direction, total $6 \times 6 = 36$ movements. The experiment involved a total of 13 epochs. In the first two epochs (baseline phase, 72 movements) the robot generated no forces. During the subsequent seven epochs (adaptation phase, 252 movements) the robot generated a force field that mimic the contribution of a muscle at the end-effector. During the adaptation phase the force-field was pesudo-ranmly removed in $1/6$ of the total number of trials. During the last four epochs (washout phase, 144 movements) the robot forces were removed.

The endpoint force that emulates the contribution of the selected muscle is given by:

$$F^H = J(q)^{-T} \cdot jj_m(q)^T \cdot F_{\mathrm{VM}} \tag{8.3}$$

where $J(q)$ is the Jacobian of the arm, jj_m and F_{VM} are respectively the vector of the moment arm and the estimated force of the selected muscle. These force fields were directly controlled by the EMG signal and by kinematic data. We extracted the envelope of EMG in real-time using using a 50 Hz notch filter, high-pass filtering (35 Hz), full-wave rectification and low-pass filtering (4 Hz, second-order Butterworth filter), and then normalized with respect to individual MVC level recorded during the calibration procedure. Through inverse kinematics approach we estimated in real-time shoulder and elbow joint value knowing end-effector coordinates and kinematic parameters.

The duration of this phase of the experiment was about 100 min.

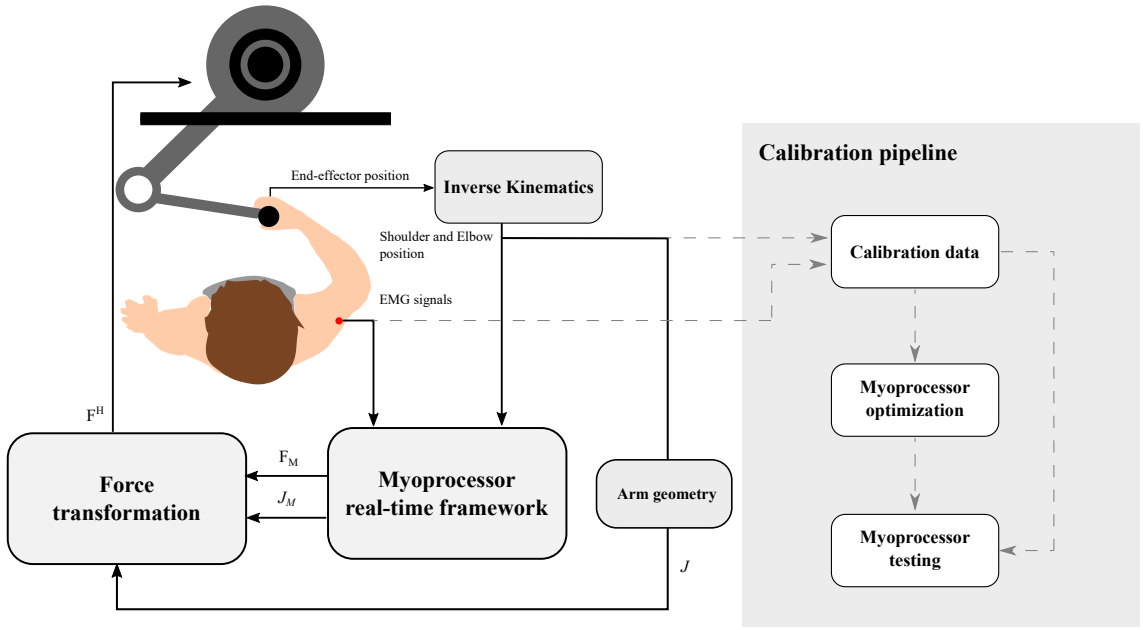

Figure 8.4 *Control scheme and Calibration pipeline.*

We calibrated the myoprocessor module on a total of five subjects (2 M + 3 F, age 25 ± 2) who presented no evidence or known history of skeletal or neurological diseases, and exhibited normal joint range of motion and muscle strength. However, in this preliminary study we performed the adaptation experiment on only one subject. We tested the effect of the virtual lateral head of the triceps

$$F^H = J(q)^{-T} \cdot jj_{\text{laTRI}}(q)^T \cdot F_{\text{laTRI}} \tag{8.4}$$

The following results are based on this pilot subject.

8.2.6 Data Analysis

For each movement we recorded the raw EMG signals from the nine muscles (sampling rate: 1000 Hz). The EMG signals envelope were extracted as described above.

The resulting EMG envelopes were sent to PC1 via a UDP connection. The following signals: (i) envelope of EMG activity, $U(t)$; (ii) endpoint trajectory, $x(t)$; (iii) force $F_h(t)$ against the robot handle were sampled at 100 Hz and saved for further analysis. We evaluated several indexes to quantify the myoprocessor calibration performance and the adaptation to the virtual muscle.

Calibration

Torque reconstruction we computed the coefficient of determination r^2 and the root means square error RMSE to quantify the ability of the myoprocessor to estimate the shoulder and the elbow joint torque by comparison with the inverse dynamics 8.2 and the torque measured from the sensor.

Adaptation

Kinematics smoothness smooth movements are a characteristic feature of healthy, efficient and well-trained motor behaviour (Sejnowski, 1998) and an external assistive device should ideally maintain such smoothness. To quantify smoothness, we used the SPectral ARC length (SPARC) index proposed in (Balasubramanian et al., 2015).

EMG reduction we evaluated the Root Mean Square (RMS) of EMG signals during the adaptation task and we looked at the reduction of this level on the late epochs of the adaptation respect to the baseline.

8.3 Results

8.3.1 Calibration

Arm kinematics reconstruction

Figure 8.5 compares the IR camera trajectory after the mapping to the end-effector.

Musculotendon geometry estimation

Figures 8.6, 8.7, 8.8 show respectively the musculotendon lengths, shoulder moment arms and elbow moment arms extracted from the spline. The orange marks are the nodes: in mono-articular muscles the set of nodes is a vector, in bi-articular muscles is a matrix.

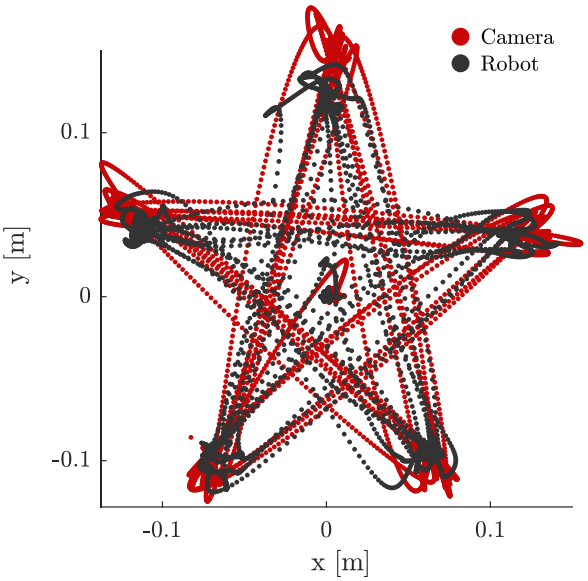

Figure 8.5 *Camera Calibration*. Dark grey dots represent the robot end-effector trajectory during the calibration task. Red dots are the calibrated trajectory after the DLT transformation.

Torque reconstruction

The performance of the myoprocessor module calibration is summarised in Figures 8.9 and 8.10 for one typical subject. Figure 8.9 displays movement speed (top) and the shoulder and elbow torques. Colored lines represent the measured torque, the black line is the torque reconstructed by the myoprocessor. Since the calibration task comprised forward and backward movements between target pairs, the different colors represent these movements (e.g. red color represents $P_1 - -P_2$ movements)

8.3.2 Adaptation

8.3.3 Kinematic changes

Figure 8.11 displays the kinematics trajectories during the adaptation task. We evaluated the kinematics smoothness trend (Figure 8.12) by using the SPARC index (Balasubramanian et al., 2015). Directions 60°, 120° and 240° preserve the smoothness during the trial. The direction of movement of 0° is the one with the largest smoothness deterioration.

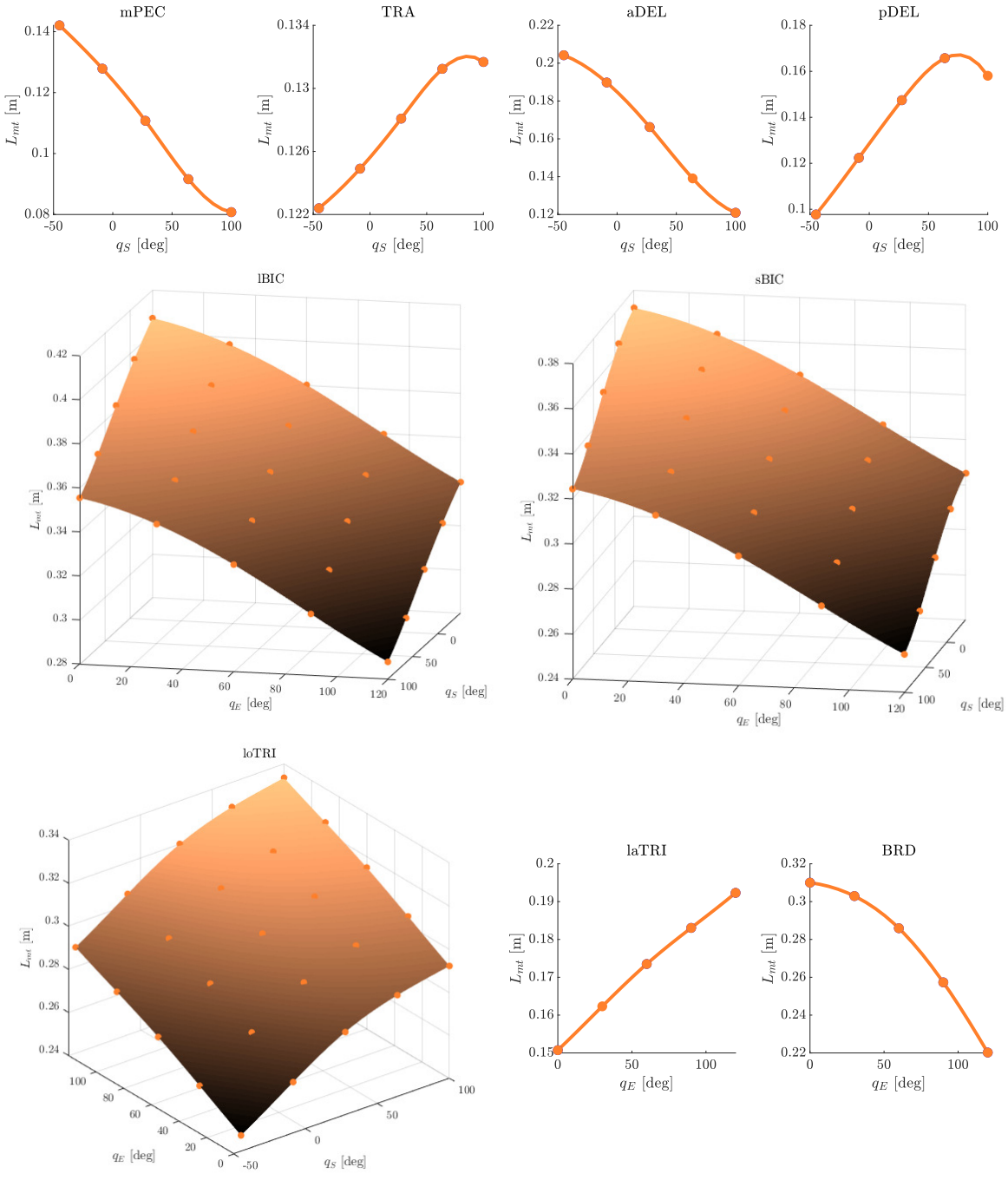

Figure 8.6 *Musculotendon lengths estimation.* Mono-articular muscles are represented by using an orange line; bi-articular muscles are described through the surface plot.

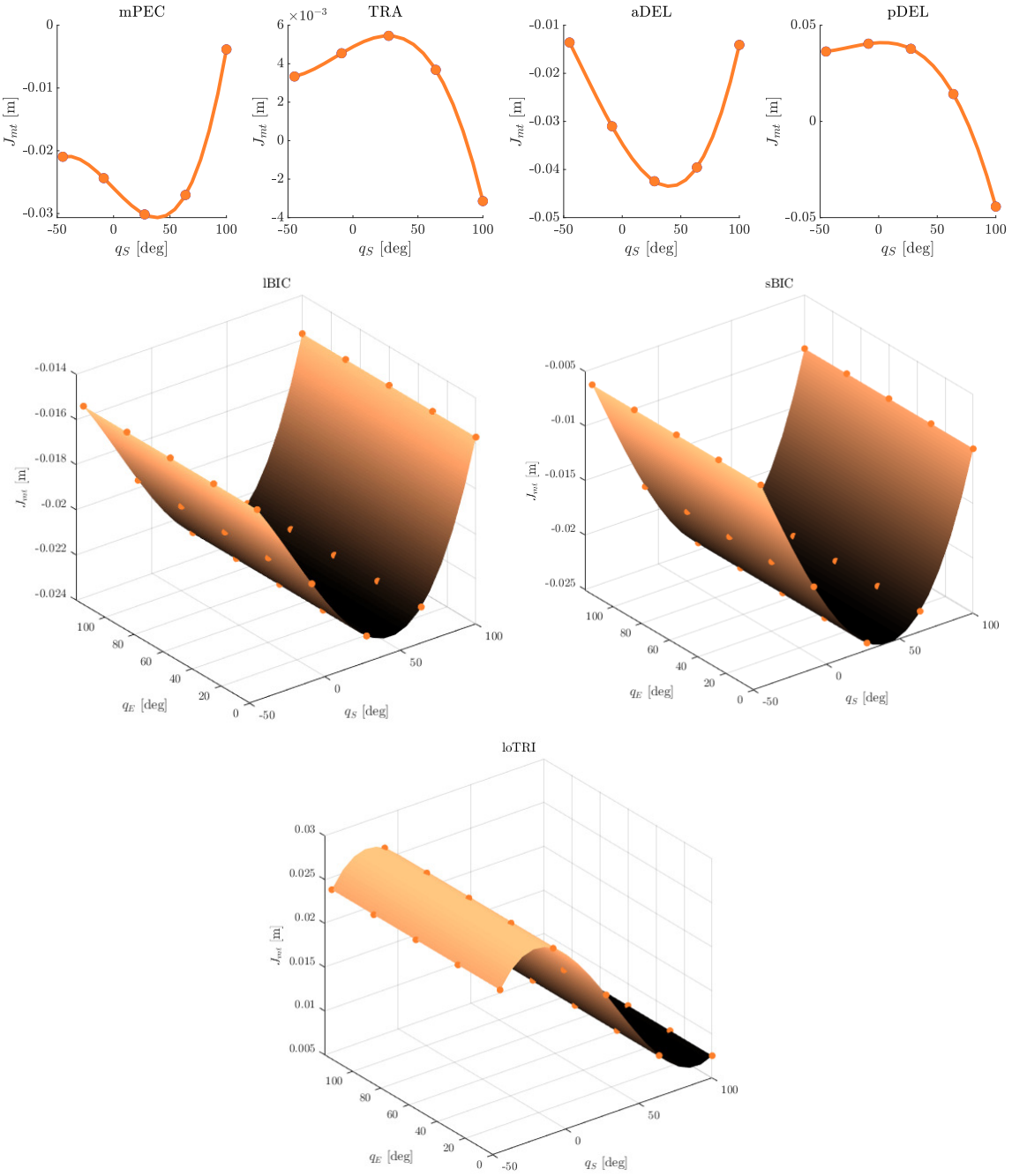

Figure 8.7 *Musculotendon shoulder moment arms estimation*. Mono-articular muscles are represented by using an orange line; bi-articular muscles are described through the surface plot.

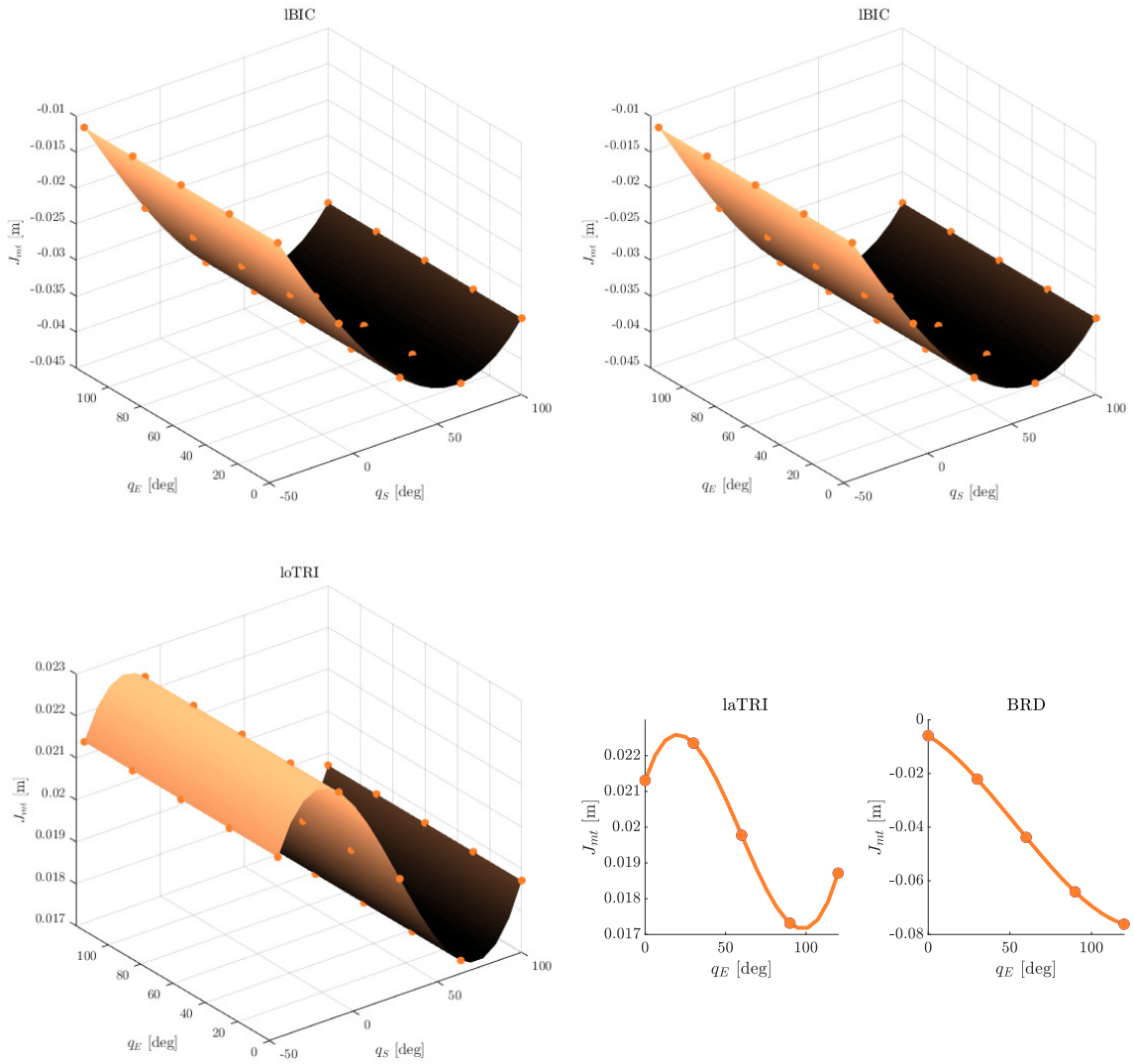

Figure 8.8 *Musculotendon elbow moment arms estimation*. Mono-articular muscles are represented by using an orange line; bi-articular muscles are described through the surface plot.

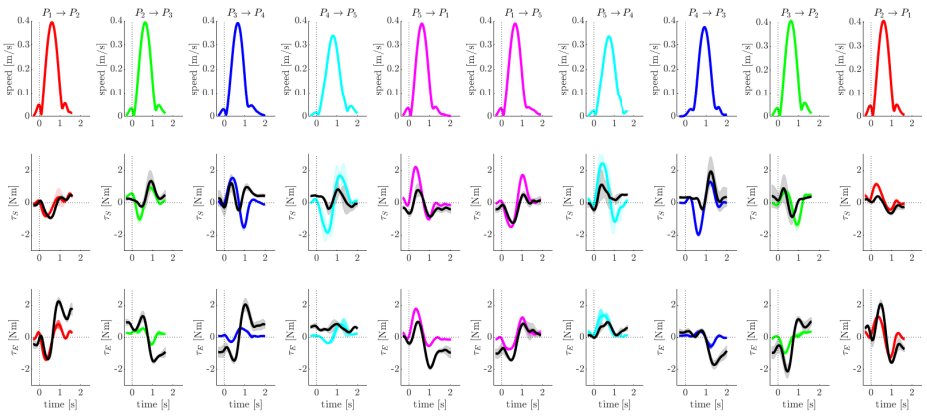

Figure 8.9 *Estimated vs measured torque* across the calibration task movements. Colored lines are the reference torques for each movement ($\tau^H + \tau_{dyn}$). The black line represents the reconstructed torque τ^M

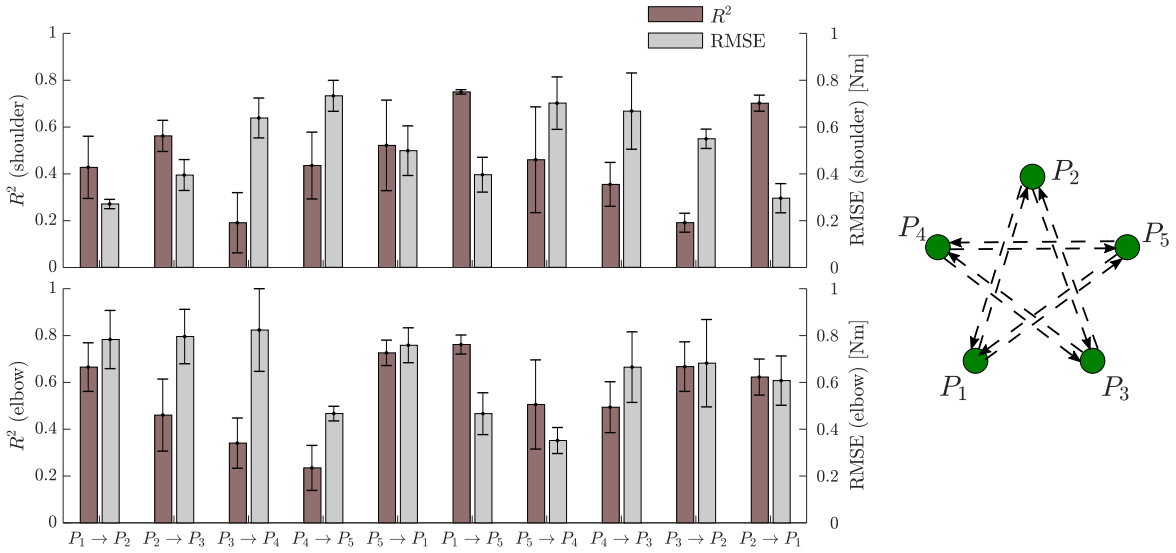

Figure 8.10 *Coefficient of determination R^2 and root mean square error RMSE* computed for the shoulder and the elbow on each movement (Mean $\pm$ SD).

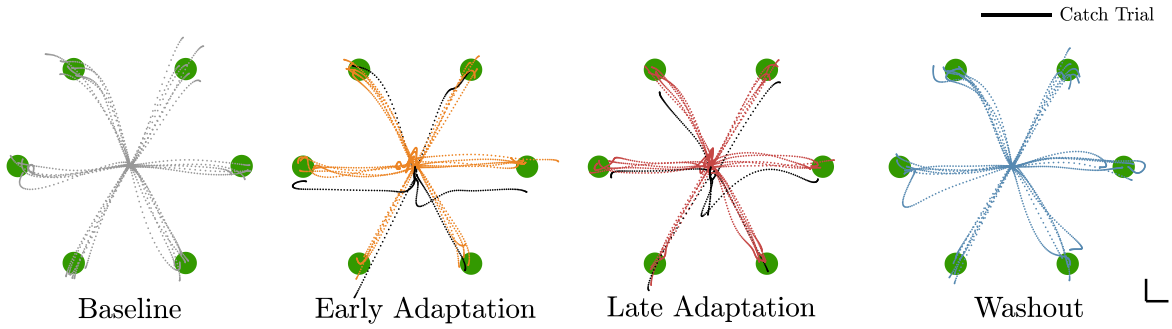

Figure 8.11 *Changing on kinematics trajectories* during the adaptation task (scale bar: 2 cm). Black lines represent the trial in which the force fields were removed.

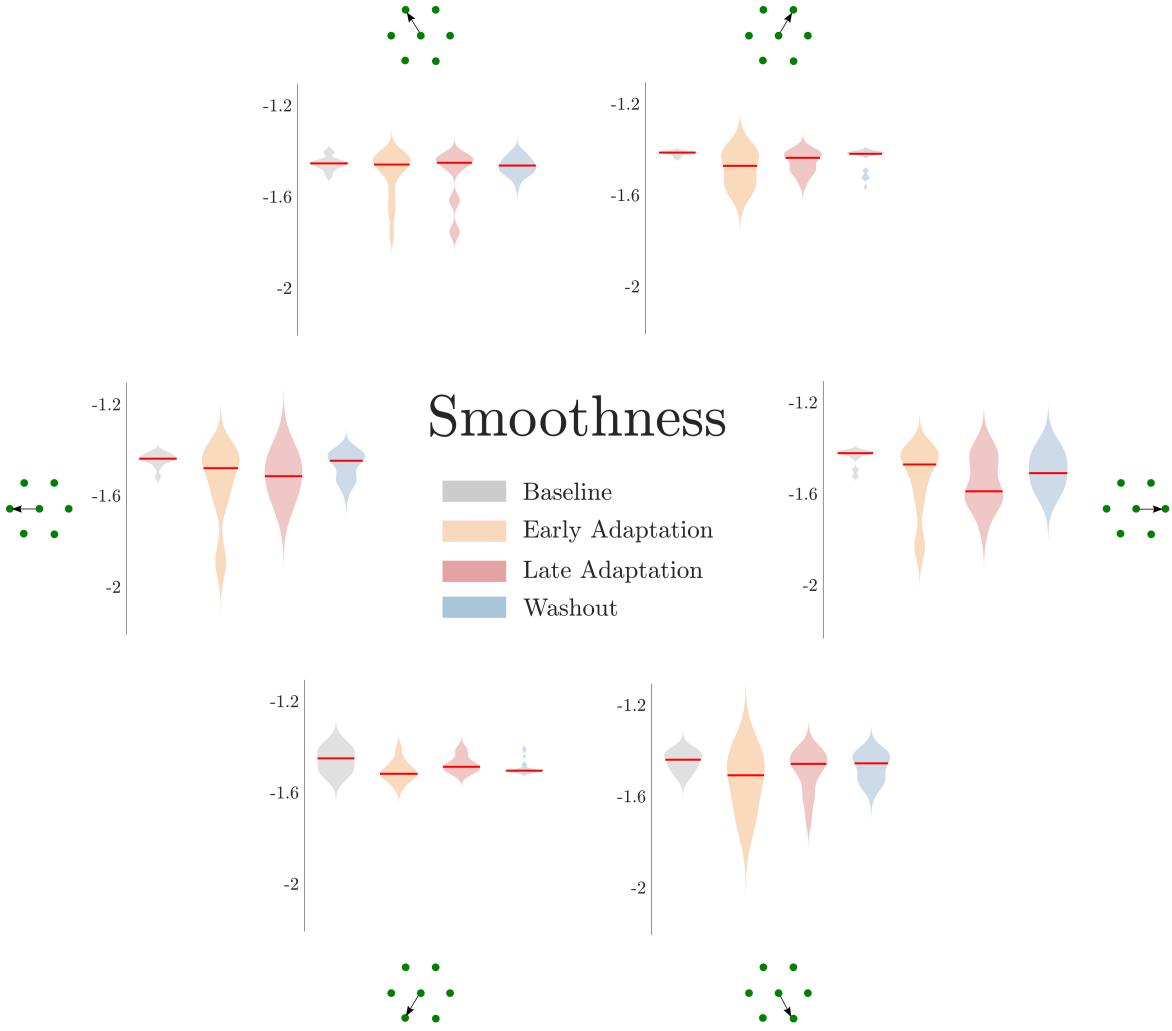

Figure 8.12 *Changing on kinematics smoothness* across the six movements, measured by using the SPARC index (Balasubramanian et al., 2015). Read line represents the median value computed overall the repetitions.

8.3.4 Myoprocessor selectively reduces the muscular activity

Figure 8.13 shows the reduction of the muscular activity during the last 2 epochs of the adaptation respect to the baseline. The virtual muscle contribution reduced the activity of the lateral head of the triceps in all movements.

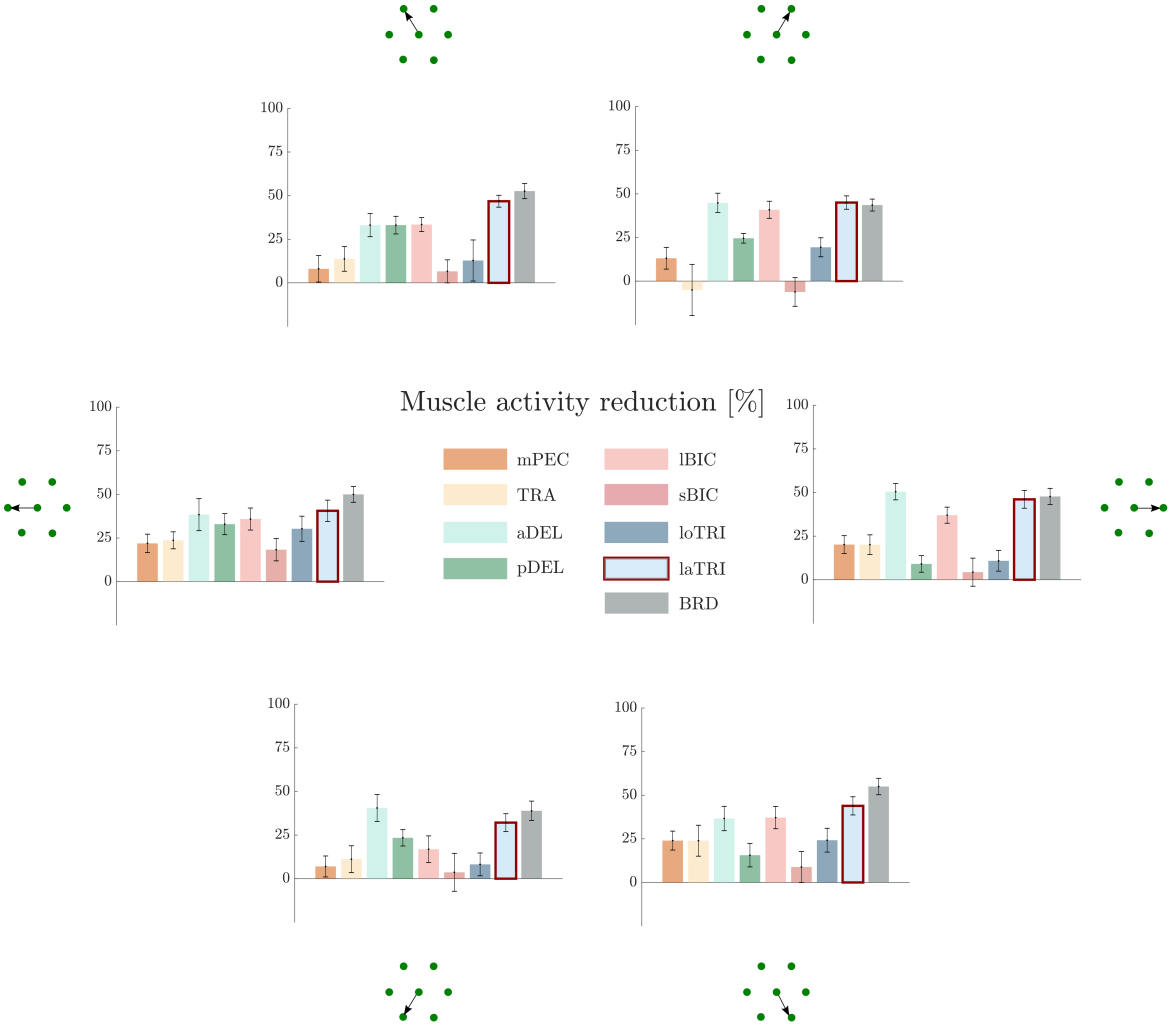

Figure 8.13 *Muscular activity reduction* between the baseline and the early adaptation (Mean ± SE).

8.4 Discussion

These preliminary results showed that a myoprocessor driven force field may be a feasible approach to probe into the organization of neuromuscular control. Our real-time framework can provides reasonably accurate estimates and reconstruct the shoulder and elbow torques in almost any direction. The worst cases are related to P_4: the reason could be that the target is close to the fully extension of the joint and the inverse kinematics estimation deteriorate the performance.

However, to the best of our knowledge, this is the first time that a myoprocessor control approach is implemented on a planar robot manipulandum and more in general in movements involving more than one joint. The adaptation induced kinematic and neuromuscular changes on the pilot subject: the kinematics smoothness (Fig. 8.12) was completely preserved along the direction of action (pulling vector) of the lateral head of the triceps (60°-240°). The virtual muscle favoured these movements and made it more difficult to execute others: the worst cases were 0° and 300°, the directions close to the perpendicular direction of the laTRI pulling vector.

The virtual muscle contribution selectively reduced muscle activity: with respect to the baseline epochs, the lateral head of the triceps activity was reduced across all directions, but this did not happen for all muscles. The long head of the biceps and the brachioradialis presented a similar trend: this could suggest a change on antagonist muscular activity. Regarding the other muscles, the reduction range is wider and depends by the direction of the movement. A possible hypothesis could be a compensatory re-organization of musculoaskeletal system.

Future steps will involve a large number of subjects in order to analyse the effects of adaptation at population level. Here we showed the effect of a replication of a real muscle: future study will investigate how to potentiate or weaken the selected muscle and the effect of this changes on the musculoskeletal system modularity. We will also investigate the effects that the virtual muscle induces on the cocontraction.

In conclusion, the preliminary results suggest that 'dynamic' virtual biomechanics may modulate the neuromuscular system by integrating its contribution on the activation pattern of the upper-limb muscles.

Selectively modifying the activity of individual muscles or muscle groups can be useful for neurorehabilitation purposes, by augmenting the force of the muscles in which the activity is deteriorate.

In pathological conditions, identifying the roles of each individual muscles may provide a basis for designing personalized treatments aimed at motor recovery.

Chapter 9

Conclusion and outlook

9.1 General conclusion

This thesis presented the development and the testing of a real-time framework myoprocessor module for the upper-limb. The final aim was an inclusion in the control loop of assistive devices for rehabilitation and assitance in activity of daily livings for subjects with neuro-muscular disorders. In the Introduction to the work, I presented the main objectives and feasibility of the study. These objectives were addressed in the third part of the thesis, the applications of this control approach. The following sections list again the aims of each Chapter, with concluding remarks on whether these they were achieved.

9.2 Major contributions

9.2.1 Myoprocessor module development

Aim: to develop a myoprocessor module in order to estimate the muscle contribution at the joints level in real-time

Chapters 3, 4 and 5 described the steps followed to develop a real-time myoprocessor module by increasing the biomechanical complexity. As a first step, I developed a myoprocessor module in which the estimated muscle forces were proportional to the electromyographic signals, by focusing on the musculoskeletal geometry estimation. This was done in several isometric conditions. Preliminary results showed a reliable estimation for all muscles.

The major limitation of the first myoprocessor version was the unreliable reconstruction of the force during movements. A second version of the module included a Hill-based

musculotendon model (Thelen, 2003) that could better reconstruct the net torque on the explored workspace. However, the reconstruction was acceptable only in few movements.

The last version proposed greatly improved the reconstruction by changing the musculoskeletal geometry estimation from simple polynomials (Pigeon et al., 1996) to multidimensional cubic splines (Sartori et al., 2012).

9.2.2 Real-time control implementation

Aim: to include the myoprocessor module in the control loop of a robot device

Chapter 6 described how to implement the myoprocessor in the control loop of a robotic device. The approach changes based on the type of controller: I showed how to achieve this in both impedance and admittance controllers.

9.2.3 Myoprocessor control for the exosuit

Aim: testing the performance of the myoprocessor module on a soft wearable arm exosuit

Chapter 7 decribed the first application of a myoprocessor real-time framework control. The study was a multi-centre collaboration in which I implemented the myoprocessor developed by the University of Twente (Durandau et al., 2018) on the soft wearable arm exosuit developed by the Nanyang Technological University of Singapore (Xiloyannis et al., 2019).

In this work we evaluate the effort of this assistance control on healthy people by looking at the kinematics performance and the muscular activity reduction.

The myoprocessor module performed in a symbiotic way with the user musculoskeletal system by enabling adaptivity support during a diverse range of mechanical loads and kinematics during elbow motion.

9.2.4 Myoprocessor-driven force field on a rehabilitation device

Aim: to study the adaptation effects of a force field driven by the myoprocessor module

Chapter 8 showed how the final version of the myoprocessor module (Chapter 5) can generate force field on a planar robot manipulandum in order to modulate the musculoskeletal system. We tested the approach only on one subject and we presented, for the first time, the feasibility of the control.

However, preliminary results suggest that 'dynamic' virtual biomechanics may be a feasible approach to probe into the organization of neuromuscular control. Selectively modifying the activity of individual muscles or muscle groups can be useful for neurorehabilitation purposes. In pathological conditions, identifying the roles of each individual muscles may provide a basis for designing personalized treatments.

9.3 Open questions and future

One main weakness of this work is that the proposed controller were only evaluated on a cohort of young, healthy participants. Although the obtained results are positive, we can only speculate on the outcome that such a technology could have on a population of subjects with neuromuscular impairments. It would be interesting to examine the effects on patients with different pathologies and at a different stage of recovery.

The work outlined in this thesis set a basis for addressing this question but did not venture in that direction.

Furthermore, we only explored the surface of the myoprocessor-driven force field adaptations. However, the aims achieved in this studies open up new frontiers in the human-machine symbiosis.

References

Anam, K. and Al-Jumaily, A. A. (2012). Active exoskeleton control systems: State of the art. *Procedia Engineering*, 41:988 – 994. International Symposium on Robotics and Intelligent Sensors 2012 (IRIS 2012).

Asbeck, A. T., Schmidt, K., and Walsh, C. J. (2014). Soft exosuit for hip assistance. *Robotics and Autonomous Systems*, 73:102–110.

Asghari Oskoei, M. and Hu, H. (2007). Myoelectric control systems-A survey. *Biomed. Signal Process. Control*, 2(4):275–294.

Balasubramanian, S., Melendez-Calderon, A., Roby-Brami, A., and Burdet, E. (2015). On the analysis of movement smoothness. *Journal of neuroengineering and rehabilitation*, 12(1):112.

Bender, E. (2011). Human exoskeletons - for war and healing. *TED*.

Berger, D. J., Gentner, R., Edmunds, T., Pai, D. K., and D'Avella, A. (2013). Differences in adaptation rates after virtual surgeries provide direct evidence for modularity. *J Neurosci*, 33(30):12384–12394.

Bizzi, E., Cheung, V., d'Avella, A., Saltiel, P., and Tresch, M. (2008). Combining modules for movement. *Brain research reviews*, 57(1):125–133.

Buckley, M. A., Yardley, A., Johnson, G. R., and Cams, D. A. (1996). Dynamics of the upper limb during performance of the tasks of everyday living: a review of the current knowledge base. *J. Eng. Med.*, 210(4):241–247.

Buongiorno, D., Barone, F., Solazzi, M., Bevilacqua, V., and Frisoli, A. (2016). A Linear Optimization Procedure for an {EMG}-driven NeuroMusculoSkeletal Model Parameters Adjusting: Validation Through a Myoelectric Exoskeleton Control. In Bello F. Kajimoto H., V. Y., editor, *Haptics: Perception, Devices, Control, and Applications - 10th International Conference, EuroHaptics 2016*, volume 9775 of *Lecture Notes in Computer Science*, pages 218–227. Springer, London, UK.

Bütefisch, C., Hummelsheim, H., Denzler, P., and Mauritz, K.-H. (1995). Repetitive training of isolated movements improves the outcome of motor rehabilitation of the centrally paretic hand. *Journal of the neurological sciences*, 130(1):59–68.

Calanca, A., Muradore, R., and Fiorini, P. (2015). A review of algorithms for compliant control of stiff and fixed-compliance robots. *IEEE/ASME Transactions on Mechatronics*, 21(2):613–624.

Casadio, M., Sanguineti, V., Morasso, P. G., and Arrichiello, V. (2006). Braccio di Ferro: a new haptic workstation for neuromotor rehabilitation. *Technol Health Care*, 14(3):123–142.

Cavallaro, E. E., Rosen, J., Perry, J. C., and Burns, S. (2006). Real-time myoprocessors for a neural controlled powered exoskeleton arm. *IEEE Trans Biomed Eng*, 53(11):2387–2396.

Cheung, V. C. K., D'Avella, A., Tresch, M. C., and Bizzi, E. (2005). Central and sensory contributions to the activation and organization of muscle synergies during natural motor behaviors. *J Neurosci*, 25(27):6419–6434.

Chiaradia, D., Xiloyannis, M., Antuvan, C. W., Frisoli, A., and Masia, L. (2018). Design and Embedded Control of a Soft Elbow Exosuit. *2018 IEEE International Conference on Soft Robotics (RoboSoft)*, pages 565–571.

Crosby, D. S., Breaker, L. C., and Gemmill, W. H. (1993). A proposed definition for vector correlation in geophysics: theory and application. *Journal of Atmospheric & Oceanic Technology*, 10(3):355–367.

Das, A. and Chakrabarti, B. K. (2005). *Quantum annealing and related optimization methods*, volume 679. Springer Science & Business Media.

d'Avella, A., Saltiel, P., and Bizzi, E. (2003). Combinations of muscle synergies in the construction of a natural motor behavior. *Nature neuroscience*, 6(3):300–308.

de Rugy, A., Loeb, G. E., and Carroll, T. J. (2012). Virtual biomechanics: a new method for online reconstruction of force from {EMG} recordings. *J Neurophysiol*, 108(12):3333–3341.

Delp, S. L., Anderson, F. C., Arnold, A. S., Loan, P., Habib, A., John, C. T., Guendelman, E., and Thelen, D. G. (2007). Opensim: open-source software to create and analyze dynamic simulations of movement. *IEEE transactions on biomedical engineering*, 54(11):1940–1950.

Delp, S. L., Loan, J. P., Hoy, M. G., Zajac, F. E., Topp, E. L., and Rosen, J. M. (1990). An interactive graphics-based model of the lower extremity to study orthopaedic surgical procedures. *IEEE Transactions on Biomedical engineering*, 37(8):757–767.

Ding, Y., Galiana, I., Asbeck, A. T., De Rossi, S. M. M., Bae, J., Santos, T. R. T., De Araujo, V. L., Lee, S., Holt, K. G., and Walsh, C. J. (2017). Biomechanical and physiological evaluation of multi-joint assistance with soft exosuits. *IEEE Trans. Neural Syst. Rehabil. Eng.*, 25(2):119–130.

Durandau, G., Farina, D., Asín-Prieto, G., Dimbwadyo-Terrer, I., Lerma-Lara, S., Pons, J. L., Moreno, J. C., and Sartori, M. (2019). Voluntary control of wearable robotic exoskeletons by patients with paresis via neuromechanical modeling. *Journal of neuroengineering and rehabilitation*, 16(1):91.

Durandau, G., Farina, D., and Sartori, M. (2018). Robust Real-Time Musculoskeletal Modeling Driven by Electromyograms. *IEEE Trans Biomed Eng*, 65(3):556–564.

Englehart, K. and Hudgins, B. (2003). A robust, real-time control scheme for multifunction myoelectric control. *IEEE Transactions on Biomedical Engineering*, 50(7):848–854.

Fehlberg, E. (1968). *Classical fifth-, sixth-, seventh-, and eighth-order Runge-Kutta formulas with stepsize control*. Number R-287 in Technical report / National Aeronautics and Space Administration. NASA, Washington, DC.

Ferreira, A., Celeste, W. C., Cheein, F. A., Bastos-Filho, T. F., Sarcinelli-Filho, M., and Carelli, R. (2008). Human-machine interfaces based on emg and eeg applied to robotic systems. *Journal of NeuroEngineering and Rehabilitation*, 5(1):10.

Flanagan, J. R. and Rao, A. K. (1995). Trajectory adaptation to a nonlinear visuomotor transformation: evidence of motion planning in visually perceived space. *Journal of neurophysiology*, 74(5):2174–2178.

Flash, T. and Hogan, N. (1985). The coordination of arm movements: an experimentally confirmed mathematical model. *J. Neurosci.*, 5(7):1688–1703.

Franklin, D. W., Burdet, E., Tee, K. P., Osu, R., Chew, C.-M., Milner, T. E., and Kawato, M. (2008). Cns learns stable, accurate, and efficient movements using a simple algorithm. *J Neurosci*, 28(44):11165–73.

Frisoli, A., Rocchi, F., Marcheschi, S., Dettori, A., Salsedo, F., and Bergamasco, M. (2005). A new force-feedback arm exoskeleton for haptic interaction in virtual environments. In *First Joint Eurohaptics Conference and Symposium on Haptic Interfaces for Virtual Environment and Teleoperator Systems. World Haptics Conference*, pages 195–201.

Gao, F., Damsgaard, M., Rasmussen, J., and Christensen, S. T. (2002). Computational method for muscle-path representation in musculoskeletal models. *Biological cybernetics*, 87(3):199–210.

Garner, B. A. and Pandy, M. G. (2000). The obstacle-set method for representing muscle paths in musculoskeletal models. *Computer methods in biomechanics and biomedical engineering*, 3(1):1–30.

Garner, B. A. and Pandy, M. G. (2003). Estimation of Musculotendon Properties in the Human Upper Limb. *Annals of Biomedical Engineering*, 31(2):207–220.

Grieve, J. R. and Dickerson, C. R. (2008). Overhead work: Identification of evidence-based exposure guidelines. *Occupational Ergonomics*, 8(1):53–66.

Habermann, C. and Kindermann, F. (2007). Multidimensional spline interpolation: Theory and applications. *Computational Economics*, 30(2):153–169.

Henneman, E., Somjen, G., and Carpenter, D. O. (1965). Functional significance of cell size in spinal motoneurons. *Journal of neurophysiology*, 28(3):560–580.

Hermens, H. J., Freriks, B., Disselhorst-Klug, C., and Rau, G. (2000). Development of recommendations for SEMG sensors and sensor placement procedures. *J. Electromyogr. Kinesiol.*, 10(5):361–374.

Hill, A. V. (1938). The heat of shortening and the dynamic constants of muscle. *Proceedings of the Royal Society of London B: Biological Sciences*, 126(843):136–195.

Hof, A. L. (2009). A simple method to remove {ECG} artifacts from trunk muscle {EMG} signals. *J Electromyogr Kinesiol*, 19(6):e554–5.

Hogan, N. (1985). Impedance Control: An Approach to Manipulation. *Am. Control Conf. 1984 IS - SN - VO -*, (March):304–313.

Hogan, N., Winters, J., and Woo, S. (1990). Multiple Muscle Systems: Biomechanics and Movement Organization.

Holzbaur, K. R., Murray, W. M., and Delp, S. L. (2005). A model of the upper extremity for simulating musculoskeletal surgery and analyzing neuromuscular control. *Annals of biomedical engineering*, 33(6):829–840.

Hudgins, B., Parker, P., and Scott, R. N. (1993). A new strategy for multifunction myoelectric control. *IEEE Transactions on Biomedical Engineering*, 40(1):82–94.

Iden, E. (2017). Xxi world congress on safety and health at work 2017–through the eyes of a delegate. *Occupational Health Southern Africa*, 23(6):6–6.

Jiang, N., Vest-Nielsen, J. L. G., Muceli, S., and Farina, D. (2012). EMG-based simultaneous and proportional estimation of wrist/hand kinematics in uni-lateral trans-radial amputees. *Journal of neuroengineering and rehabilitation*, 9(1):42.

Klamroth-Marganska, V., Blanco, J., Campen, K., Curt, A., Dietz, V., Ettlin, T., Felder, M., Fellinghauer, B., Guidali, M., Kollmar, A., et al. (2014). Three-dimensional, task-specific robot therapy of the arm after stroke: a multicentre, parallel-group randomised trial. *The Lancet Neurology*, 13(2):159–166.

Kuiken, T. A., Li, G., Lock, B. A., Lipschutz, R. D., Miller, L. A., Stubblefield, K. A., and Englehart, K. B. (2009). Targeted muscle reinnervation for real-time myoelectric control of multifunction artificial arms. *Jama*, 301(6):619–628.

Kwakkel, G., Kollen, B., and Lindeman, E. (2004). Understanding the pattern of functional recovery after stroke: facts and theories. *Restor. Neurol. Neurosci.*, 22(3-5):281–299.

Lloyd, D. G. and Besier, T. F. (2003). An EMG-driven musculoskeletal model to estimate muscle forces and knee joint moments in vivo. *Journal of biomechanics*, 36(6):765–776.

Lo, H. S. and Xie, S. Q. (2012). Exoskeleton robots for upper-limb rehabilitation: State of the art and future prospects. *Med. Eng. Phys.*, 34(3):261–268.

Lotti, N. and Sanguineti, V. (2017). Toward EMG-controlled force field generation for training and rehabilitation: From movement data to muscle geometry. In *IEEE International Conference on Rehabilitation Robotics*.

Lotti, N. and Sanguineti, V. (2018). EMG-Driven Force Fields: Toward a Myoprocessor for 'Virtual Biomechanics'. In *International Conference on NeuroRehabilitation*, pages 1161–1165. Springer.

Lotti, N., Xiloyannis, M., Durandau, G., Galofaro, E., Sanguineti, V., Sartori, M., et al. (2020). Adaptive model-based myoelectric control for a soft wearable arm exosuit: A new generation of wearable robot control. *IEEE Robotics & Automation Magazine*.

Manal, K., Gonzalez, R. V., Lloyd, D. G., and Buchanan, T. S. (2002). A real-time {EMG}-driven virtual arm. *Computers in Biology and Medicine*, 32(1):25–36.

Masia, L. and Vitiello, N. (2020). The long and winding road to symbiotic wearable robotics [young professionals]. *IEEE Robotics & Automation Magazine*, 27(1):9–9.

Mason, M. T. (1981). Compliance and force control for computer controlled manipulators. *IEEE Transactions on Systems, Man, and Cybernetics*, 11(6):418–432.

Nielsen, J. L. G., Holmgaard, S., Jiang, N., Englehart, K. B., Farina, D., and Parker, P. A. (2011). Simultaneous and Proportional Force Estimation for Multifunction Myoelectric Prostheses Using Mirrored Bilateral Training. *{IEEE} Transactions on Biomedical Engineering*, 58(3):681–688.

Norman, R. W. and Komi, P. V. (1979). Electromechanical delay in skeletal muscle under normal movement conditions. *Acta Physiologica Scandinavica*, 106(3):241–248.

Park, D. and Cho, K.-J. (2017). Development and evaluation of a soft wearable weight support device for reducing muscle fatigue on shoulder. *PloS one*, 12(3):e0173730.

Pigeon, P., Yahia, L., and Feldman, A. G. (1996). Moment arms and lengths of human upper limb muscles as functions of joint angles. *J Biomech*, 29(10):1365–1370.

Pizzolato, C., Reggiani, M., Saxby, D. J., Ceseracciu, E., Modenese, L., and Lloyd, D. G. (2017). Biofeedback for gait retraining based on real-time estimation of tibiofemoral joint contact forces. *IEEE Transactions on Neural Systems and Rehabilitation Engineering*, 25(9):1612–1621.

Raibert, M. H., Craig, J. J., et al. (1981). Hybrid position/force control of manipulators. *Journal of Dynamic Systems, Measurement, and Control*, 103(2):126–133.

Rosen, J., Brand, M., Fuchs, M. B., and Arcan, M. (2001). A myosignal-based powered exoskeleton system. *IEEE Trans. Syst. Man, Cybern. Part ASystems Humans.*, 31(3):210–222.

Rosen, J., Fuchs, M. B., and Arcan, M. (1999). Performances of Hill-type and neural network muscle modelstoward a myosignal-based exoskeleton. *Computers and Biomedical Research*, 32(5):415–439.

Sartori, M., Durandau, G., Došen, S., and Farina, D. (2018). Robust simultaneous myoelectric control of multiple degrees of freedom in wrist-hand prostheses by real-time neuromusculoskeletal modeling. *Journal of Neural Engineering*, 15(6):066026.

Sartori, M., Llyod, D. G., and Farina, D. (2016). Neural data-driven musculoskeletal modeling for personalized neurorehabilitation technologies. *IEEE Transactions on Biomedical Engineering*, 63(5):879–893.

Sartori, M., Reggiani, M., van den Bogert, A. J., and Lloyd, D. G. (2012). Estimation of musculotendon kinematics in large musculoskeletal models using multidimensional B-splines. *Journal of biomechanics*, 45(3):595–601.

Sartori, M., van de Riet, J., and Farina, D. (2019). Estimation of phantom arm mechanics about four degrees of freedom after targeted muscle reinnervation. *IEEE Transactions on Medical Robotics and Bionics*.

Schiele, A., Letier, P., Van Der Linde, R., and Van Der Helm, F. (2006). Bowden cable actuator for force-feedback exoskeletons. *IEEE Int. Conf. Intell. Robot. Syst.*, pages 3599–3604.

Schutte, L. M., Rodgers, M. M., Zajac, F. E., and Glaser, R. M. (1993). Improving the efficacy of electrical stimulation-induced leg cycle ergometry: an analysis based on a dynamic musculoskeletal model. *IEEE Transactions on Rehabilitation Engineering*, 1(2):109–125.

Sejnowski, T. J. (1998). Making smooth moves. *Nature*, 394(6695):725–726.

Tee, K. P., Franklin, D. W., Kawato, M., Milner, T. E., and Burdet, E. (2010). Concurrent adaptation of force and impedance in the redundant muscle system. *Biol Cybern*, 102(1):31–44.

Thelen, D. G. (2003). Adjustment of muscle mechanics model parameters to simulate dynamic contractions in older adults. *Journal of Biomechanical Engineering*, 125(1):70–77.

Thelen, D. G., Anderson, F. C., and Delp, S. L. (2003). Generating dynamic simulations of movement using computed muscle control. *J Biomech*, 36(3):321–328.

Todorov, E. and Jordan, M. I. (2002). Optimal feedback control as a theory of motor coordination. *Nature {N}euroscience*, 5(11):1226–1235.

Tresch, M. C., Cheung, V. C. K., and D'Avella, A. (2006). Matrix factorization algorithms for the identification of muscle synergies: evaluation on simulated and experimental data sets. *J Neurophysiol*, 95(4):2199–2212.

Tresch, M. C., Saltiel, P., and Bizzi, E. (1999). The construction of movement by the spinal cord. *Nature neuroscience*, 2(2):162–167.

Van Peppen, R. P., Kwakkel, G., Wood-Dauphinee, S., Hendriks, H. J., Van der Wees, P. J., and Dekker, J. (2004). The impact of physical therapy on functional outcomes after stroke: what's the evidence? *Clinical rehabilitation*, 18(8):833–862.

Winby, C. R., Lloyd, D. G., Besier, T. F., and Kirk, T. B. (2009). Muscle and external load contribution to knee joint contact loads during normal gait. *Journal of biomechanics*, 42(14):2294–2300.

Winter, D. A. (2009). *Biomechanics and motor control of human movement*. Wiley, Hoboken, N.J., 4th ed edition.

Wolpert, D. (2011). The real reason for brains. *TED*.

Xiloyannis, M., Chiaradia, D., Frisoli, A., and Masia, L. (2019). Physiological and kinematic effects of a soft exosuit on arm movements. *Journal of NeuroEngineering and Rehabilitation*, 16(1):29.

Yu, W., Rosen, J., and Li, X. (2011). Pid admittance control for an upper limb exoskeleton. In *Proceedings of the 2011 American control conference*, pages 1124–1129. IEEE.

Zajac, F. E. (1989). Muscle and tendon Properties models scaling and application to biomechanics and motor. *Critical reviews in biomedical engineering*, 17(4):359–411.

Appendix A

List of Publications

Journal Paper

- Lotti, N., Xiloyannis, M., Durandau, G., Galofaro, E., Sanguineti, V., Masia, L., and Sartori,M. Adaptive model-based myoelectric control for a soft wearable arm exosuit: A new generation of wearable robot control. *IEEE Robotics & Automation Magazine, 2020*.

Conference Proceeding

- Tiseni L., Xiloyannis M., Chiaradia D., Lotti N., Solazzi M., van der Kooij H., Frisoli A., Masia L. On the edge between soft and rigid: an assistive shoulder exoskeleton with hyper-redundant kinematics. Oral Presentation, *International conference on Rehabilitation Robotics* (ICORR), 23-28 June 2019, Toronto (CA).

- Lotti N., Piscopiello D., Sanguineti V. A user model for adaptation of task parameters in robot-assisted exercise. Oral Presentation, *International Conference on Neurorehabilitation*, 16-20 October 2018, Pisa (IT).

- Lotti N. and Sanguineti V. EMG-driven force fields: toward a myoprocessor for virtual biomechanics. Workshop, Oral Presentation, *International Conference on Neurorehabilitation*, 16-20 October 2018, Pisa (IT).

- Lotti N. and Sanguineti V. Estimation of muscle torques from EMG and kinematics during planar arm movements. Poster Presentation, *IEEE International Conference on Biomedical Robotics and Biomechatronics*, 29-29 August 2018, Enschede (NL).

- Lotti N. and Sanguineti V. EMG-controlled force field generation: myocontroller module for Real-Time force estimation. Abstract & Poster Presentation, Sixth National Congress of Bioengineering, 25-27 June 2018, Milan (IT).

- Lotti N. and Sanguineti V. Toward emg-controlled force field generation for training and rehabilitation: From movement data to muscle geometry. Poster Presentation, *International conference on Rehabilitation Robotics* (ICORR), 17-20 July 2017, London (UK)

Conference Abstracts

- Lotti N. and Sanguineti V. EMG-controlled force field generation: myocontroller module for Real-Time force estimation. Abstract & Poster Presentation, *Sixth National Congress of Bioengineering*, 25-27 June 2018, Milan (IT).

- Lotti N. and Sanguineti V. EMG-controlled force field generation: incorporating muscle geometry and muscle activation dynamics. Abstract & Poster Presentation, *Annual Meeting of the Society for Neuroscience* (SfN 2017), 11-15 November 2017, Washington (DC).

- Lotti N. and Sanguineti V. Muscle model geometry estimation through EMG and kinematic signals. Abstract & Poster Presentation, *School & Symposium on advanced Neurorehabilitation* (SSNR2017), 17-22 September 2017, Baiona (ES).